

UNIVERSITY OF CALIFORNIA

Los Angeles

**Studies of Linear and Nonlinear Photoemission
Processes in Metals and Semiconductors**

A dissertation submitted in partial satisfaction of the
requirements for the degree
Doctor of Philosophy in Physics

by

Robert Patrick Brogle

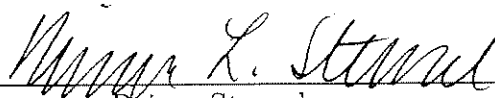
1996

© Copyright by
Robert Patrick Brogle
1996

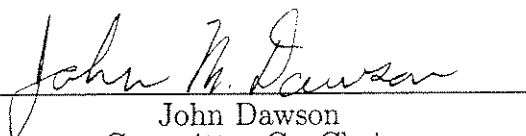
The dissertation of Robert Patrick Brogle is approved.



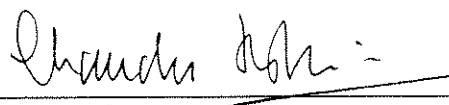
Claudio Pellegrini



Reiner Stenzel



John Dawson
Committee Co-Chair



Chan Joshi
Committee Co-Chair

University of California, Los Angeles

1996

DEDICATION

To my parents, James and Barbara Brogle.

To my brothers and sisters: Rick, Rebecca, Randy, Ron, and Rachel.

Contents

DEDICATION	iii
List of Figures	vii
ACKNOWLEDGMENTS	xi
VITA AND PUBLICATIONS	xiii
ABSTRACT	xv
1 Introduction	1
2 Theory and Previous Work	5
2.1 Absorption Probability for an Electron in a Metal	5
2.2 Fowler-DuBridge Theory	7
2.3 Photocurrent	11
2.4 Photoemission Examples	14
2.4.1 Thermionic Emission: $n = 0, T \gg 0$	14
2.4.2 Linear Photoemission: $n = 1$	15
2.4.3 Thermally Assisted Photoemission: $n = 1, T \gg 0$	16
2.4.4 Nonlinear Photoemission: $n \geq 2$	17

2.4.5	Thermally Assisted Multiphoton Emission: $n \geq 2, T \gg 0$	18
2.4.6	Multicolor Emission	18
2.5	Previous Work	20
3	Multiphoton and Multicolor Emission	24
3.1	Laser System	24
3.2	Multiphoton Photoemission Setup	26
3.3	Single-Color Photoemission	29
3.3.1	Emitted Charge vs. Incident Laser Energy	30
3.3.2	Photoemission from Copper	31
3.4	Multicolor Photoemission	37
4	RF Gun Photocathode Tests	51
4.1	Quantum Efficiency and the Effects of Laser Damage	53
4.1.1	Copper Measurements	55
4.1.2	Magnesium Measurements	57
4.2	Effects of the RF Gun Environment	58
5	Photoemission from Semiconductors	64
5.1	Band Structure of Semiconductors	65
5.2	N-type Doping	67
5.3	P-type Doping	68
5.4	Silicon	70
5.5	Diamond	72
5.5.1	Pure Diamond Film	72
5.5.2	Doped Diamond Film	74

5.5.3	Single-Crystal Bulk Diamond	76
5.6	Fullerene Films	78
5.7	Summary of Electron Yields	80
5.8	Damage Threshold Measurements	84
6	Thin Film Photoemission Experiment	92
6.1	Photoelectron Dynamics	92
6.1.1	One-photon Emission	95
6.1.2	Two-photon Emission	99
6.1.3	Three-photon Emission	101
6.2	Front and Back Illumination Experiment	105
6.3	Emission Promptness	113
7	Conclusions	115
	Bibliography	118

List of Figures

2.1	Sommerfeld model of electrons in a metal.	7
2.2	Graph of the exact and approximate integrands of $N_{av}^{e^-}$	10
2.3	The Fowler function.	12
2.4	Thermionic emission.	15
2.5	The linear photoelectric effect.	16
2.6	Thermally assisted photoemission.	16
2.7	Two-photon photoelectric effect.	17
2.8	Thermally assisted 2-photon photoemission.	18
2.9	2-color, 2-photon photoelectric effect.	19
3.1	Four stage dye laser system.	25
3.2	Multiphoton photoemission experiment.	27
3.3	Single-color transitions in copper.	32
3.4	Charge vs. energy curves for copper.	33
3.5	Two-color transitions in copper.	37
3.6	Emitted charge vs. delay time between the 650 nm and 325 nm pulses.	40
3.7	Enhanced charge vs. 650 nm energy.	41
3.8	Values of $b_{1+1}E_{325}$ vs. E_{325}	43
3.9	Enhanced charge vs. 325 nm energy.	44

3.10	Values of $b_{1+1}E_{650}$ vs. E_{650}	45
3.11	Two-color photoemission from copper for long delay times.	46
3.12	Two-color photoemission by coupling to a long-lived energy state of the cathode.	48
4.1	Setup for the DC test gun experiment.	53
4.2	Electron yield of copper before and after laser damage.	56
4.3	Electron yield of magnesium before and after laser damage.	59
4.4	Quantum efficiency map of the Spawr polished copper photocathode after 4 months in the UCLA RF gun.	61
4.5	Quantum efficiency map of a hand polished copper photocathode before and after one week of use in the UCLA RF gun.	62
5.1	Band structure for an undoped (intrinsic) semiconductor.	65
5.2	A heavily doped n-type semiconductor.	68
5.3	A heavily doped p-type semiconductor.	69
5.4	Emitted charge vs. incident energy for n- and p-type silicon.	71
5.5	Emitted charge vs. incident energy for cauliflower and well-oriented pure diamond films.	73
5.6	Emitted charge vs. incident energy for sodium-doped and boron- doped diamond films.	75
5.7	Emitted charge vs. incident energy for (110) and (111) single- crystal bulk diamond.	77
5.8	Emitted charge vs. incident energy for pure and yttrium-doped fullerene films.	79
5.9	The b_1 coefficients for various materials at 217 nm incident wave- length.	81

5.10	The b_2 coefficients for various materials at 325 nm incident wavelength.	82
5.11	The b_3 coefficients for various materials at 650 nm incident wavelength.	83
5.12	Emitted ion charge vs. incident 650 nm laser energy for copper, boron-doped diamond film, and (110) bulk diamond.	86
5.13	Emitted ion charge vs. incident 325 nm laser energy for copper, boron-doped diamond film, and (110) bulk diamond.	88
5.14	Emitted ion charge vs. incident 217 nm laser energy for copper, boron-doped diamond film, and (110) bulk diamond.	89
6.1	Empirical curve for electron range vs. excitation energy.	94
6.2	Front and back side photoemission from a film of thickness d . . .	96
6.3	The theoretical behavior of the electron yield vs. film thickness for front and back illumination of copper by 217 nm light.	98
6.4	Two-photon front emission from a metal film of thickness d	100
6.5	Theoretical behavior of the 2-photon electron yield vs. film thickness for front and back illumination of copper by 325 nm light. . .	102
6.6	Three-photon front emission from a metal film of thickness d	104
6.7	Theoretical behavior of the 3-photon electron yield vs. film thickness for front and back illumination of copper by 650 nm light. . .	105
6.8	Setup for the multiphoton thin film illumination experiment. . . .	107
6.9	Optical transmission vs. copper film thickness.	108
6.10	The measured 1-photon yield vs. copper film thickness for front and back illumination by 217 nm laser pulses.	109

6.11	The measured 2-photon yield vs. copper film thickness for front and back illumination by 325 nm laser pulses.	111
6.12	The measured 3-photon yield vs. copper film thickness for front and back illumination by 650 nm laser pulses.	112

ACKNOWLEDGEMENTS

There are many people to whom I am greatly indebted for their assistance and moral support during my years in graduate school:

To Prof. Chan Joshi, my thesis advisor, for taking me on as his student, for guiding me and showing faith in me along the way, and for providing a research environment which produces not only excellent scientific work but also, perhaps more importantly, friendships. I feel extremely fortunate to have been a part of Chan's group.

To Prof. John Dawson, my co-advisor, for his support in both my classroom and laboratory work, and in particular for his guidance early in my studies when I was searching for an area of research.

To Dr. Patrick Muggli, with whom I worked daily on the photoemission experiment, for his guidance, his patience, and his understanding. He taught me much about what it means to be good scientist, and without him none of the experiments would have been possible.

To Dr. Richard Savage, for showing me the ropes during my first year in the laser lab, and for designing the target chamber used in all of the photoemission experiments.

To Dr. Shyankay Jou and Prof. Rointan Bunshah, for providing the silicon, diamond, and fullerene samples used in the experiment.

To Penny Lucky, the physics department graduate advisor, for being incredibly helpful no matter how busy she was at the time.

To Maria Guerrero for all her help with the administrative and paper work.

To all the guys in the lab: Amit Lal, Pepe Davis, Dave Blackwell, Dan Gordon, Ken Marsh, Chris Clayton, and Ritesh Narang. Their assistance was invaluable, but their friendships are what made graduate school such a tremendous experience. I doubt I'll ever find such a great group of people to work with again.

And finally, I would like to give very special thanks to Wila Chunbomrung, for being my best friend.

VITA

- June 26, 1967 Born, Gainesville, Florida
- 1989 B.S., Physics, Stanford University
- 1989–90 Teaching Assistant, Department of Physics, University
of California, Los Angeles
- 1990 M.S., Physics, University of California, Los Angeles
- 1989–96 Graduate Student Researcher, Departments of Physics
and Electrical Engineering, University of California, Los
Angeles

PUBLICATIONS AND PRESENTATIONS

R. Brogle, R. Savage, and C. Joshi, “Frequency Upshifting of Radiation via Laser-Produced Ionization Fronts”, paper presented at the 22nd Annual Anomalous Absorption Conference, Lake Placid, NY, July 12–17, 1992.

R. L. Savage, Jr., R. P. Brogle, W. B. Mori, and C. Joshi, “Photon Acceleration via Laser-Produced Ionization Fronts”, Proceedings of the 8th International Conference on Ultrafast Phenomena, Antibes-Juan-les-pins, France, June 8–12, 1992.

✓ R. L. Savage, Jr., R. P. Brogle, W. B. Mori, and C. Joshi, "Frequency Upshifting and Pulse Compression via Underdense Relativistic Ionization Fronts", IEEE Transactions on Plasma Science, **21** (1) 5–19 (1993).

P. Muggli, R. Brogle, C. Zhang, and C. Joshi, "Studies of Fundamental Processes Leading to Electron Emission from Surfaces by Sub-picosecond Laser Pulses", paper presented at the 35th Annual Meeting of the Division of Plasma Physics of the American Physical Society, St. Louis, MO, Nov. 1–5, 1993.

✓ P. Muggli, R. Brogle, and C. Joshi, "Two-color Photoemission Produced by Femtosecond Laser Pulses on Copper", Journal of the Optical Society of America B (Optical Physics), **12** (4) 553–8 (1995).

R. Brogle, P. Muggli, P. Davis, G. Hairapetian, and C. Joshi, "Studies of Linear and Nonlinear Photoelectric Emission for Advanced Accelerator Applications", Proceedings of the 1995 Particle Accelerator Conference, Dallas, TX, May 1995.

✓ P. Muggli, R. Brogle, S. Jou, H. J. Doerr, R. F. Bunshah, and C. Joshi, "Photoemission from Diamond and Fullerene Films", IEEE Transactions on Plasma Science, **24** (2) April, 1996.

ABSTRACT OF THE DISSERTATION

**Studies of Linear and Nonlinear Photoemission
Processes in Metals and Semiconductors**

by

Robert Patrick Brogle

Doctor of Philosophy in Physics

University of California, Los Angeles, 1996

Professor Chan Joshi, Co-Chair

Professor John Dawson, Co-Chair

Various issues in linear and nonlinear photoemission were studied using different harmonic wavelengths of a short pulse laser system. 1-, 2-, and 3-photon emission from copper was observed using subpicosecond pulses of 217, 325, and 650 nm wavelengths, respectively. The electron yield for each n -photon process was measured and found to be proportional to I^n as predicted by the generalized Fowler-DuBridge theory with no heating effects. The quantum efficiency of copper at 217 nm was $\eta_{217} = 1.2 \times 10^{-3}$. The first multicolor photoemission process was discovered and characterized using overlapping 325 and 650 nm laser pulses. Emission properties of copper and magnesium RF photoinjector gun cathodes were studied using 50 ps, 266 nm pulses. At this wavelength the quantum efficiency of copper was $\eta_{266} = 1.0 \times 10^{-5}$. The quantum efficiency of magnesium was initially low but increased dramatically upon laser ablation of its surface to

a higher value than copper, then quickly began to deteriorate as contamination set in. The effect of the RF gun environment on copper photocathodes was investigated by creating quantum efficiency maps of the cathode surfaces. It was found that short term exposure in the gun produced a smoothing of the surface emission, while long term exposure led to contamination and laser damage which caused large variations in emission across the surface. This led to an investigation of alternate cathode materials: silicon, diamond, and fullerene. Boron-doped diamond showed the most promise as a photocathode material, having a quantum efficiency and damage fluence product $\eta\mathcal{E}_{dam}$ comparable to that of copper. Finally, electron dynamics of multiphoton emission were studied using thin copper films. The majority of electrons were produced by bulk (volume) photoemission, and the maximum electron escape depth was measured to be 250 Å at 217 nm and 350 Å at 325 nm in the absence of space charge. From these escape depths the maximum delay time between the incident laser pulse and the emitted electrons was calculated to be 12 fs for 217 nm and 21 fs for 325 nm light. These time delays will be negligible for laser pulses > 100 fs in duration.

Chapter 1

Introduction

The success of Maxwell's equations for electromagnetism had convinced late 19th century scientists of the wave nature of light. However, when Hertz [1], Thomson [2], Lenard [3], and others performed photoemission experiments by illuminating metals with ultraviolet light and measuring the current of electrons that were emitted, their results began to show inconsistencies with this wave model.

For example, the wave theory of light predicts that the energy absorbed by an electron in an illuminated metal should be proportional to the intensity of the incident light. Thus measuring the maximum kinetic energy of the emitted electrons as a function of light intensity should demonstrate this relationship. The results of these photoemission experiments, however, showed that the electron kinetic energy was not dependent on the light intensity, but rather was proportional to the incident light *frequency*.

Einstein offered an explanation in 1905 [4] using the concept of quantization developed by Max Planck five years earlier [5]. Einstein assumed that light was composed of discrete particles called photons, each having an energy proportional to the frequency of the light:

$$E = h\nu \tag{1.1}$$

where ν is frequency and h is Planck's constant. The process of photoemission occurs when individual electrons in the metal absorb individual photons and gain this amount of energy. The maximum kinetic energy of the electrons ejected from the metal would then be given by the equation

$$E_{max} = h\nu - e\Phi \quad (1.2)$$

where e is the magnitude of the electron charge and Φ is the work function of the metal. Because E_{max} must have a positive value, there is a threshold condition on the photon energy. If the photon energy $h\nu$ is less than $e\Phi$ (the energy required to overcome the work function) no emission will be observed because the photoexcited electrons will have insufficient energy to escape the material.

These predictions were confirmed by subsequent photoemission experiments, and thus Einstein's theory became the standard model. Since then theoretical modifications have been made to account for such processes as temperature effects and multiphoton emission, and with the advent of lasers many experiments have been designed to test these theories and to develop a wide range of photoemission applications. In this paper we will investigate theoretical and experimental issues of linear and nonlinear photoemission, and applications of the emission process to studies of metal and semiconductor photocathodes.

Chapter 2 describes the modern theory of photoemission. This was first developed for single-photon (linear) emission from metals in 1931—not so modern—but more recently has been generalized to include multiphoton (nonlinear) photoemission. Multiphoton emission can be observed only with high intensity laser systems and thus is a relatively new development. This chapter also surveys some of the main findings in the photoemission field.

Utilizing amplified femtosecond dye laser pulses we performed photoemission

experiments on copper using three different laser harmonics to produce 1-, 2-, and 3-photon emission. This led to the first observation of a multicolor emission process from electrons occupying the Fermi states of the metal. Electron yield measurements were performed for all these processes—the details and results will be described in Chapter 3.

Chapter 4 presents experimental results investigating single-photon emission properties of copper and magnesium with respect to their use as photocathode materials in electron accelerators. For these experiments we used frequency quadrupled Nd:YAG laser pulses which are standard for many such accelerators. We also studied the short and long term effects of an accelerator environment on the emission performance of copper using actual cathodes from the UCLA RF photoinjector gun.

The results of these copper and magnesium photocathode experiments led us to search for alternative photocathode materials for accelerator applications. In Chapter 5 we present results of photoemission studies on various types of semi-conducting materials including silicon, diamond, and fullerene. One or more of these chemically inert materials may provide a suitable replacement for a copper photocathode if the product of its quantum efficiency and laser damage fluence $\eta\mathcal{E}_{dam}$ is comparable to that of copper.

Chapter 6 describes some of the electron dynamics of single and multiphoton photoemission. Using thin copper films, we investigated electron emission from both the front and the back side with respect to the incident laser pulse. From this we could determine the depth from which the electrons are emitted in the metal and estimate the “promptness” of the photoemission process. These results indicate the feasibility of using a back illuminated photocathode in a linac

or other accelerator where laser access from the front side is limited. We also calculated the minimum temporal width for a photoemitted electron bunch created by an ultrashort laser pulse.

Finally, the findings of our various experiments are summarized in Chapter 7.

Chapter 2

Theory and Previous Work

To begin our photoemission study, we will develop a theory predicting the total number of electrons emitted from a metal illuminated by a given laser pulse. This number of electrons will depend on two factors: (1) the probability of each electron absorbing the n photons necessary for emission and (2) the number of electrons in the metal available for such an emission process. The first part is described by simple probability theory in Sec. 2.1 while the second part is calculated using the Fowler-DuBridge theory detailed in Sec. 2.2.

2.1 Absorption Probability for an Electron in a Metal

The probability of an electron in a metal absorbing a photon during a short time interval dt is proportional to the number of photons incident on the electron during that time:

$$p_1(t)dt \propto N_\gamma(t)dt \quad (2.1)$$

where N_γ is the number of incident photons per area per unit time. Because N_γ is related to the intensity I of the incident light by

$$N_\gamma(t) = \frac{I(t)}{h\nu} \quad (2.2)$$

we can write the single-photon absorption probability as

$$p_1(t)dt \propto I(t)dt \quad (2.3)$$

The probability of an electron absorbing two photons in a time dt is equal to the product of two single-photon absorption probability densities multiplied by the time interval dt :

$$p_2(t)dt = [p_1(t) \cdot p_1(t)]dt = p_1^2(t)dt \propto N_\gamma^2(t)dt \propto I^2(t)dt \quad (2.4)$$

For an electron absorbing n photons in a time dt we have

$$p_n(t)dt = p_1^n(t)dt \propto N_\gamma^n(t)dt \propto I^n(t)dt \quad (2.5)$$

Let us now assume that the electron is illuminated by a laser pulse with a gaussian intensity profile

$$I(t) = I_0 e^{-t^2/\tau^2} \quad (2.6)$$

The probability of the electron absorbing one photon from the laser pulse is then proportional to the total energy per area \mathcal{E} of the pulse at the location of the electron:

$$P_1 = \int_{-\infty}^{+\infty} p_1(t)dt \propto \int_{-\infty}^{+\infty} I(t)dt = I_0 \int_{-\infty}^{+\infty} e^{-t^2/\tau^2} dt = \sqrt{\pi} I_0 \tau = \mathcal{E} \quad (2.7)$$

The two-photon absorption probability for an electron is then

$$P_2 = \int_{-\infty}^{+\infty} p_2(t)dt \propto \int_{-\infty}^{+\infty} I^2(t)dt = I_0^2 \int_{-\infty}^{+\infty} e^{-2t^2/\tau^2} dt = \sqrt{\frac{\pi}{2}} I_0^2 \tau \propto \frac{\mathcal{E}^2}{\tau} \quad (2.8)$$

and the n -photon absorption probability is

$$P_n = \int_{-\infty}^{+\infty} p_n(t)dt \propto \int_{-\infty}^{+\infty} I^n(t)dt = \sqrt{\frac{\pi}{n}} I_0^n \tau \propto \frac{\mathcal{E}^n}{\tau^{n-1}} \quad (2.9)$$

Note that single-photon absorption depends only on the energy of the laser pulse while multiphoton absorption depends on both the incident energy and pulsewidth.

2.2 Fowler-DuBridge Theory

The number of electrons in a metal available for photoemission at a given frequency of light was calculated by Robert Fowler [6] and experimentally verified by Lee DuBridge [7] in their studies of the photoelectric effect in 1931. The Fowler-DuBridge theory is based on the Sommerfeld model of electrons in a metal (Fig. 2.1). The electrons are free but contained inside the metal by a potential step of energy W_0 at the surface. The distribution of energy levels of this free electron gas obeys Fermi-Dirac statistics.

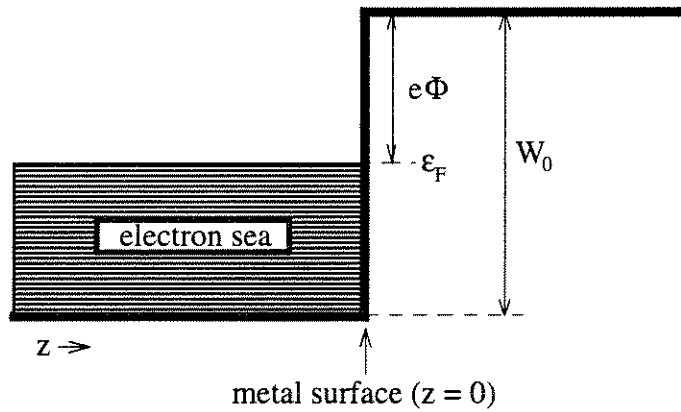


Figure 2.1: Sommerfeld model of electrons in a metal for electron temperature $T \approx 0$ K. W_0 is the surface step height (as measured from the bottom of the conduction band), ϵ_F is the Fermi energy, e is the magnitude of the electron charge, and Φ is the metal work function.

For such a distribution the number of electrons per unit volume having an x -component of velocity between v_x and $v_x + dv_x$, a y -component between v_y and $v_y + dv_y$, and a z -component between v_z and $v_z + dv_z$ is [8]

$$n(v_x, v_y, v_z)dv_x dv_y dv_z = 2 \left(\frac{m}{h} \right)^3 \frac{dv_x dv_y dv_z}{e^{[\frac{1}{2}m(v_x^2 + v_y^2 + v_z^2) - \epsilon_F]/kT} + 1} \quad (2.10)$$

where m is the electron mass, k is the Boltzmann constant, T is the electron

temperature, and the Fermi energy ϵ_F is the energy of the highest occupied state at $T = 0$ K.

Let us define \hat{z} as the direction perpendicular to the metal surface. The number of electrons per unit volume with a z -component of velocity between v_z and $v_z + dv_z$ is found by integrating Eq. 2.10 over v_x and v_y :

$$n(v_z)dv_z = \frac{4\pi kT}{m} \left(\frac{m}{h}\right)^3 \ln [1 + e^{(\epsilon_F - \frac{1}{2}mv_z^2)/kT}] dv_z \quad (2.11)$$

This brings us to the main hypothesis of the Fowler-DuBridge theory: the number of electrons in the metal available for photoemission is equal to the number of electrons having kinetic energy in the \hat{z} direction large enough to overcome the potential step at the surface after absorbing a photon:

$$\frac{1}{2}mv_z^2 + h\nu \geq W_0 \quad (2.12)$$

This hypothesis ignores collisions and assumes that the direction of motion of the electron is unchanged after the absorption of a photon. If we compare the momentum of an ultraviolet photon p_γ to the momentum of a Fermi level electron in copper p_{e^-} we see that

$$\begin{aligned} p_\gamma &\approx 5 \text{ eV}/c \\ p_{e^-} &\approx 2700 \text{ eV}/c \end{aligned}$$

The photon momentum is negligible compared to the electron momentum and therefore the photon cannot change the electron's direction of motion. The velocities of the photoexcited electrons in the metal will then be isotropic because the initial Fermi velocities are isotropic. The only electrons which have a chance to be emitted, however, are those which satisfy Eq. 2.12. We can determine the

number of such available electrons $N_{av}^{e^-}$ by integrating over the z -velocities of the Fermi distribution:

$$N_{av}^{e^-} = \int_{\frac{1}{2}mv_z^2=W_0-h\nu}^{\infty} n(v_z)dv_z \quad (2.13)$$

$$= \frac{4\pi kT}{m} \left(\frac{m}{h}\right)^3 \int_{\frac{1}{2}mv_z^2=W_0-h\nu}^{\infty} \ln[1 + e^{(\epsilon_F - \frac{1}{2}mv_z^2)/kT}]dv_z \quad (2.14)$$

Making the substitution $u = [\frac{1}{2}mv_z^2 - (W_0 - h\nu)]/kT$ and using the fact that $W_0 - \epsilon_F = e\Phi$ gives

$$N_{av}^{e^-} = \frac{2\pi kT}{m} \left(\frac{2kT}{m}\right)^{1/2} \left(\frac{m}{h}\right)^3 \int_0^{\infty} \frac{\ln[1 + e^{-u+(h\nu-e\Phi)/kT}]}{[u + (W_0 - h\nu)/kT]^{1/2}} du \quad (2.15)$$

For the typical case of a visible photon incident on a metal at room temperature we will have $(W_0 - h\nu)/kT \gg u$ for all values of u while the integrand of Eq. 2.15 is finite (the numerator tends to zero as u becomes large). Thus we can neglect the u in the denominator and write Eq. 2.15 as

$$N_{av}^{e^-} = \frac{2\pi kT}{m} \left(\frac{2kT}{m}\right)^{1/2} \left(\frac{m}{h}\right)^3 \int_0^{\infty} \frac{\ln[1 + e^{-u+(h\nu-e\Phi)/kT}]}{[(W_0 - h\nu)/kT]^{1/2}} du \quad (2.16)$$

$$= \frac{2\sqrt{2}\pi m^{3/2}}{h^3} \frac{k^2 T^2}{(W_0 - h\nu)^{1/2}} \int_0^{\infty} \ln[1 + e^{-u+(h\nu-e\Phi)/kT}] du \quad (2.17)$$

To check the validity of this approximation, Fig. 2.2 shows a graph of the integrands of Eq. 2.15 and Eq. 2.16 for two different photon energies incident on copper. At $h\nu = 5.0$ eV the exact and approximate curves are virtually identical; however, as we increase the photon energy to 8.0 eV the approximation introduces an error of $\sim 10\%$ in the integral. For higher energies the error continues to get worse, thus for copper we take 8 eV to be the upper limit of the regime in which the Fowler approximation is valid.

The integral of Eq. 2.17 can be solved by integrating by parts, expanding the natural logarithm, and then integrating term by term. Defining $\mu \equiv (h\nu - e\Phi)/kT$

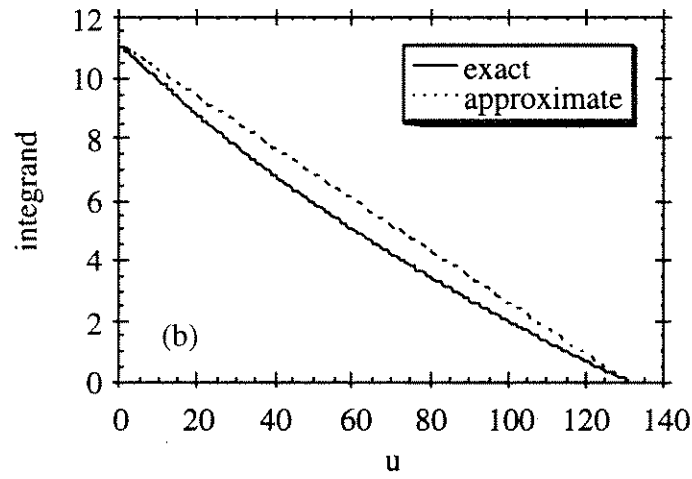
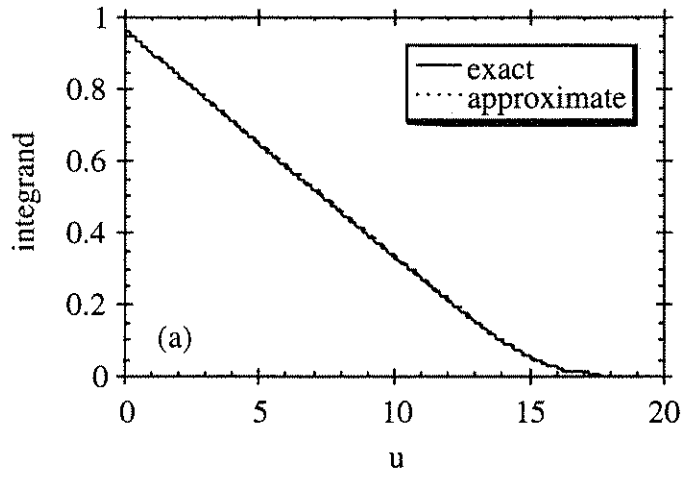


Figure 2.2: Graph of the exact and approximate integrands of N_{av}^{e-} for photon energies of (a) $h\nu = 5.0$ eV and (b) $h\nu = 8.0$ eV. Sommerfeld quantities are those of room temperature copper: $W_0 = 11.6$ eV, $e\Phi = 4.6$ eV, $T = 300$ K.

we obtain

$$N_{av}^{e^-} = \frac{2\sqrt{2}\pi m^{3/2}}{h^3} \frac{k^2 T^2}{(W_0 - h\nu)^{1/2}} \left[e^\mu - \frac{e^{2\mu}}{2^2} + \frac{e^{3\mu}}{3^2} - \dots \right] \quad (2.18)$$

for $\mu \leq 0$, and

$$N_{av}^{e^-} = \frac{2\sqrt{2}\pi m^{3/2}}{h^3} \frac{k^2 T^2}{(W_0 - h\nu)^{1/2}} \left(\frac{\pi^2}{6} + \frac{\mu^2}{2} - \left[e^{-\mu} - \frac{e^{-2\mu}}{2^2} + \frac{e^{-3\mu}}{3^2} - \dots \right] \right) \quad (2.19)$$

for $\mu \geq 0$. The infinite series in Eqs. 2.18 and 2.19 is known as the Fowler function. It is continuous and is defined for any quantity μ as

$$F(\mu) = \begin{cases} e^\mu - \frac{e^{2\mu}}{2^2} + \frac{e^{3\mu}}{3^2} - \dots & \text{for } \mu \leq 0 \\ \frac{\pi^2}{6} + \frac{\mu^2}{2} - \left(e^{-\mu} - \frac{e^{-2\mu}}{2^2} + \frac{e^{-3\mu}}{3^2} - \dots \right) & \text{for } \mu \geq 0 \end{cases} \quad (2.20)$$

The behavior of the Fowler function is shown in Fig. 2.3.

The number of available electrons can therefore be written as

$$N_{av}^{e^-} = \frac{2\sqrt{2}\pi m^{3/2}}{h^3} \frac{k^2 T^2}{(W_0 - h\nu)^{1/2}} F\left(\frac{h\nu - e\Phi}{kT}\right) \quad (2.21)$$

To generalize to the case of multiphoton emission, we simply note that the absorbed energy will be $nh\nu$ instead of $h\nu$. Thus the number of available electrons for an n -photon emission process will be

$$N_{av}^{e^-} = \frac{2\sqrt{2}\pi m^{3/2}}{h^3} \frac{k^2 T^2}{(W_0 - nh\nu)^{1/2}} F\left(\frac{nh\nu - e\Phi}{kT}\right) \quad (2.22)$$

2.3 Photocurrent

The number of electrons emitted per area per unit time $N_{em}^{e^-}$ in an n -photon process will be proportional to the probability per time of such a process occurring

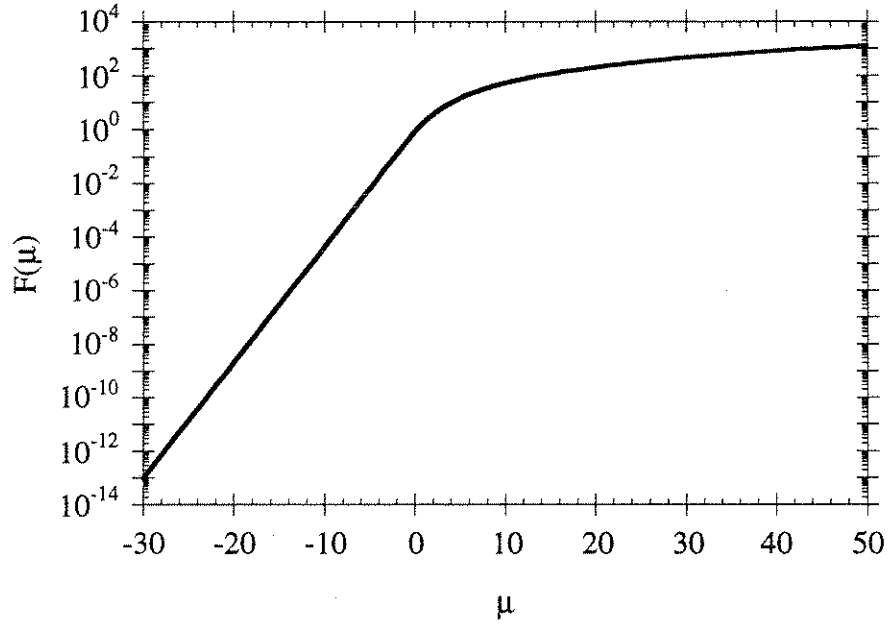


Figure 2.3: The Fowler function.

for each electron multiplied by the total number of electrons available for this process. From Sections 2.1 and 2.2 we have

$$N_{em}^{e^-} \propto p_n N_{av}^{e^-} \quad (2.23)$$

$$\propto N_{\gamma}^n N_{av}^{e^-} \quad (2.24)$$

This can be written in terms of an emitted current density J_n as

$$J_n = e N_{em}^{e^-} \propto e N_{\gamma}^n N_{av}^{e^-} \quad (2.25)$$

If the light which reaches the electrons in the metal has intensity I_{e^-} we can use Eq. 2.2 to write

$$J_n \propto e \left(\frac{I_{e^-}}{h\nu} \right)^n N_{av}^{e^-} \quad (2.26)$$

Because of the reflection at the surface of the metal, the intensity of light which reaches the electrons will be related to the incident intensity by

$$I_{e^-} = (1 - R)I \quad (2.27)$$

where R is the reflection coefficient of the metal surface. Eq. 2.26 then becomes

$$J_n \propto e \left[\frac{(1 - R)I}{h\nu} \right]^n N_{av}^{e^-} \quad (2.28)$$

Using the expression for $N_{av}^{e^-}$ given in Eq. 2.22 we obtain

$$J_n \propto \frac{2\sqrt{2}\pi m^{3/2}}{h^3} \frac{e(1 - R)^n I^n k^2 T^2}{(h\nu)^n (W_0 - nh\nu)^{1/2}} F\left(\frac{nh\nu - e\Phi}{kT}\right) \quad (2.29)$$

This can be simplified a bit by substituting the Richardson coefficient $A \equiv 4\pi m e k^2 / h^3 \approx 120 \text{ A}/(\text{cm}^2 \text{K}^2)$:

$$J_n \propto \frac{m^{1/2} A (1 - R)^n I^n T^2}{\sqrt{2} (h\nu)^n (W_0 - nh\nu)^{1/2}} F\left(\frac{nh\nu - e\Phi}{kT}\right) \quad (2.30)$$

We now note that for copper, a change in $nh\nu$ from the photoemission threshold of 4.6 eV up to 8 eV (the upper limit for a valid Fowler approximation) results in less than a 30% change in $(W_0 - nh\nu)^{1/2}$. This term in general is weakly dependent on frequency and as a first approximation can be absorbed into the constant of proportionality. Thus we can write the n th order current density in its conventional form [9]:

$$J_n = a_n A \left(\frac{e}{h\nu}\right)^n (1 - R)^n I^n T^2 F\left(\frac{nh\nu - e\Phi}{kT}\right) \quad (2.31)$$

where a_n is a material dependent coefficient having units of $(\text{cm}^2 \text{s}/\text{C})^n$. This coefficient contains all of the physical processes not taken into account by the rest of Eq. 2.31: the electron cross-section, scattering events inside the metal, probability of electron reflection at the surface barrier, etc. These processes

are very difficult to quantify theoretically and thus a_n must be experimentally determined for each material. The a_n 's may also depend on the metal surface preparation.

In principle the total photocurrent will be the sum of the currents for all possible processes:

$$J_{tot} = \sum_{n=0}^{\infty} J_n \quad (2.32)$$

although for room temperature metals the only measurable contribution will come from the J_n term having the lowest n which satisfies the condition

$$nh\nu \geq e\Phi \quad (2.33)$$

2.4 Photoemission Examples

In order to obtain a better picture of the Fowler-DuBridge theory, we will now look at some examples of various orders of photoemission processes.

2.4.1 Thermionic Emission: $n = 0$, $T \gg 0$

When electrons in a metal are heated, some will move to occupy excited energy states above the Fermi level. If the electron temperature is large enough, electrons in the high energy states may have sufficient thermal energy to overcome the work function and escape the metal without requiring additional energy from an incident photon (Fig. 2.4). This is the zeroth order photoemission process—thermionic emission. For $n = 0$, Eq. 2.31 reduces to the following (assuming $e\Phi \gg kT$):

$$J_0 = a_0 AT^2 e^{-e\Phi/kT} \quad (2.34)$$

Thus for the case of no incident photons the Fowler-Dubridge theory produces the familiar Richardson-Dushman equation for thermionic emission [10], [11], [12].

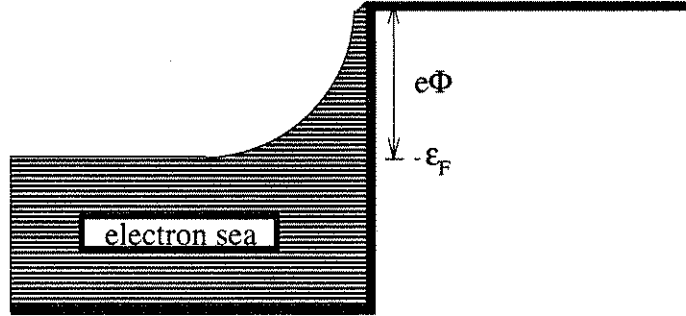


Figure 2.4: Thermionic emission. The temperature is high enough that electrons in the tail of the thermal distribution have sufficient energy to overcome the potential barrier at the surface.

2.4.2 Linear Photoemission: $n = 1$

For low temperatures (e.g., room temperature) the highest occupied energy state will be very close to the Fermi level, and thus the condition

$$h\nu \geq e\Phi \quad (2.35)$$

must be met in order to observe photoemission (Fig 2.5). For $n = 1$, Eq. 2.31 becomes

$$J_1 = a_1 A \left(\frac{e}{h\nu} \right) (1 - R) I T^2 F \left(\frac{h\nu - e\Phi}{kT} \right) \quad (2.36)$$

If the electron temperature does not change during the photoemission process then we can absorb all the other terms into one constant coefficient c_1 and write

$$J_1 = c_1 I \quad (2.37)$$

Thus for $n = 1$ the photocurrent is linearly dependent on the incident light intensity.

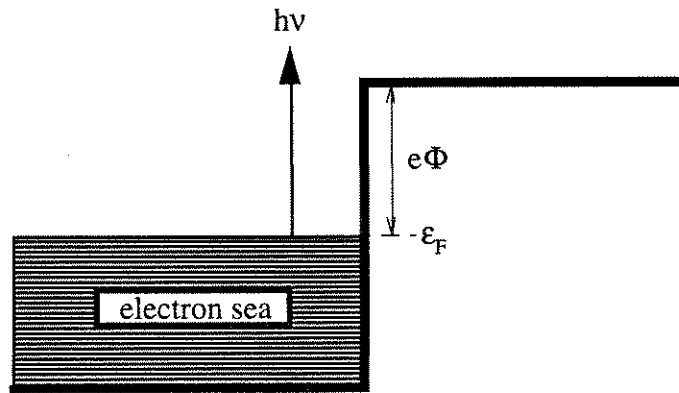


Figure 2.5: The linear photoelectric effect.

2.4.3 Thermally Assisted Photoemission: $n = 1, T \gg 0$

If the electron temperature is very high but below the level required to produce significant thermionic emission, then the dominant emission process may be a thermally assisted photoelectric effect (Fig. 2.6). Because the high temperature electrons occupy states above the Fermi level, it is possible to produce photoemission with photons having energies below threshold ($h\nu < e\Phi$).

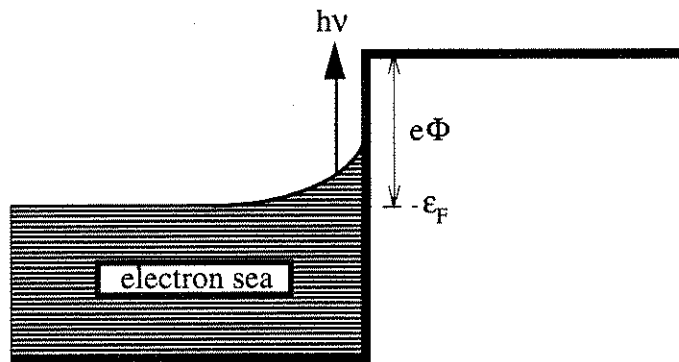


Figure 2.6: Thermally assisted photoemission.

2.4.4 Nonlinear Photoemission: $n \geq 2$

For very large incident light intensities in which the photon energies are below the work function, electron emission may occur by means of the multiphoton photoelectric effect. For 2-photon photoemission, Eq. 2.31 becomes

$$J_2 = a_2 A \left(\frac{e}{h\nu} \right)^2 (1 - R)^2 I^2 T^2 F \left(\frac{2h\nu - e\Phi}{kT} \right) \quad (2.38)$$

If the electron temperature does not change during the emission process we can simplify this expression as before:

$$J_2 = c_2 I^2 \quad (2.39)$$

Generalizing to the case of a temperature constant n -photon effect, we obtain

$$J_n = c_n I^n \quad (2.40)$$

From Eq. 2.40 we see that for multiphoton processes ($n > 1$) the photocurrent is a nonlinear function of the incident intensity.

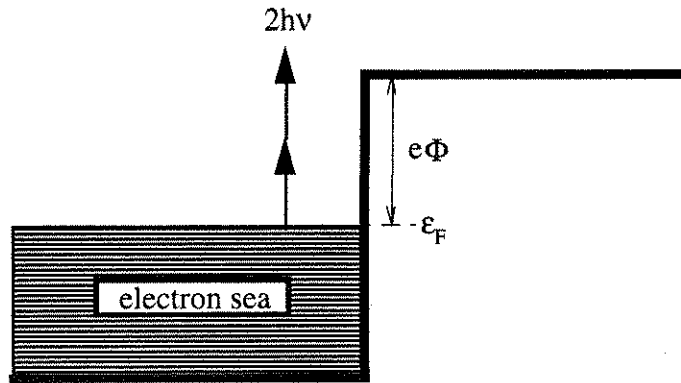


Figure 2.7: Two-photon photoelectric effect.

2.4.5 Thermally Assisted Multiphoton Emission: $n \geq 2$,

$$T \gg 0$$

Thermally assisted multiphoton emission is a combination of the last two cases (Fig. 2.8). This process may be dominant for high electron temperatures and high incident light intensities with low photon energies. In such a case an electron requires a large thermal energy plus the energy of multiple photons in order to overcome the work function and escape the metal.

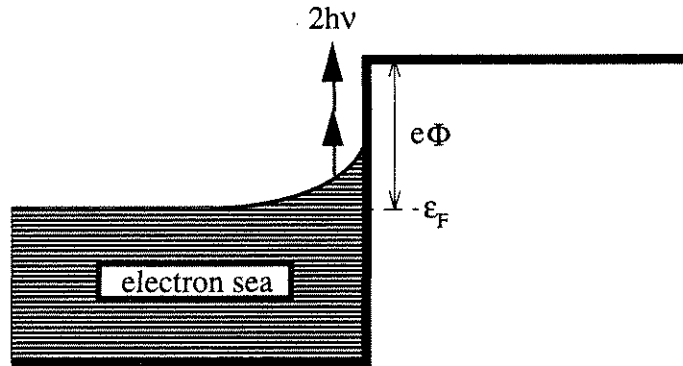


Figure 2.8: Thermally assisted 2-photon photoemission.

2.4.6 Multicolor Emission

So far we have considered emission processes due to illumination by photons of a single frequency. However, if a metal is illuminated by photons of different frequencies then we may observe a multicolor emission process provided the condition

$$\sum_i n_i h\nu_i \geq e\Phi \quad (2.41)$$

is satisfied (we will assume room temperature electrons so that thermal effects are negligible). The sum is over all incident frequencies and n_i is the number of

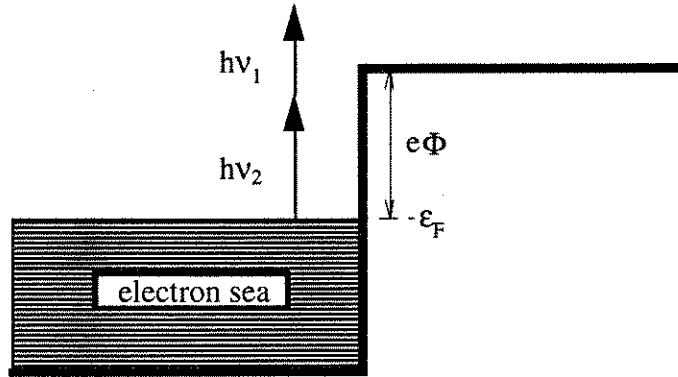


Figure 2.9: 2-color, 2-photon photoelectric effect.

photons of the i th frequency involved in the process.

For example, Fig. 2.9 shows an emission process due to the absorption of two photons of different frequencies, ν_1 and ν_2 . The condition for this emission process is (from Eq. 2.41)

$$h\nu_1 + h\nu_2 \geq e\Phi \quad (2.42)$$

We can write an expression for the resulting photocurrent by modifying Eq. 2.31 to account for the two frequencies:

$$J_{\nu_1+\nu_2} = a_{\nu_1+\nu_2} A \left(\frac{e}{h\nu_1} \right) \left(\frac{e}{h\nu_2} \right) (1 - R_{\nu_1})(1 - R_{\nu_2}) \times I_{\nu_1} I_{\nu_2} T^2 F \left(\frac{h(\nu_1 + \nu_2) - e\Phi}{kT} \right) \quad (2.43)$$

As in Sec. 2.4 we can reduce this expression for the case of constant temperature:

$$J_{\nu_1+\nu_2} = c_{\nu_1+\nu_2} I_{\nu_1} I_{\nu_2} \quad (2.44)$$

Finally, we can derive a general expression for the photocurrent resulting from a process involving m different frequencies of light, each frequency ν_i contributing n_{ν_i} photons:

$$\begin{aligned}
J_{n_{\nu_1}+\dots+n_{\nu_m}} &= a_{n_{\nu_1}+\dots+n_{\nu_m}} A \left(\frac{e}{h\nu_1} \right)^{n_{\nu_1}} \dots \left(\frac{e}{h\nu_m} \right)^{n_{\nu_m}} \times \\
&\quad (1 - R_{\nu_1})^{n_{\nu_1}} \dots (1 - R_{\nu_m})^{n_{\nu_m}} I_{\nu_1}^{n_{\nu_1}} \dots I_{\nu_m}^{n_{\nu_m}} \times \\
&\quad T^2 F \left(\frac{h(n_{\nu_1}\nu_1 + \dots + n_{\nu_m}\nu_m) - e\Phi}{kT} \right) \quad (2.45)
\end{aligned}$$

This can be simplified as before to give the general expression for a multicolor, multiphoton emission current for constant temperature:

$$J_{n_{\nu_1}+\dots+n_{\nu_m}} = c_{n_{\nu_1}+\dots+n_{\nu_m}} I_{\nu_1}^{n_{\nu_1}} \dots I_{\nu_m}^{n_{\nu_m}} \quad (2.46)$$

Thus the Fowler-DuBridge theory of photoemission can be generalized to include not only multiphoton emission processes but also processes involving different numbers of photons from different frequencies of incident light.

2.5 Previous Work

The Fowler-DuBridge theory provided a simple yet highly accurate description of photoemission which remains the standard model today [13]. However, one issue which is not addressed by this theory is the question of momentum conservation in the photoemission process. The Sommerfeld model assumes a free electron gas, yet a free electron cannot absorb a photon because such a process violates conservation of momentum. Tamm and Schubin noted in 1931 [14] that there are two possible sources of the extra momentum required for photoemission: the potential step at the metal surface and the periodic potential of the ion lattice sites in the metal bulk (this periodic potential is not included in the Sommerfeld theory). Photoemission resulting from momentum contributed by the surface potential is described as a *surface photoelectric effect*, while photoemission due to momentum provided by the lattice sites is a *volume photoelectric effect*.

The surface effect requires a component of the electric field of the incident light to be perpendicular to the surface in order to conserve momentum. Thus for a perfectly smooth surface only p -polarized light can cause surface photoemission. However, for real materials having a given amount of surface roughness both s - and p - polarized light may produce the surface photoelectric effect. The electrons emitted by this effect must originate very close to the surface (within a few angstroms) in order to exchange momentum with the potential step upon photon absorption.

The volume photoelectric effect has fewer requirements. Because the potential of each lattice site is spherical, there is no polarization preference for the incident light. Also, the electrons can originate from anywhere within the material provided that the incident light reaches the electrons and that the electrons can travel to the surface without losing their excitation energy through collisions (see Chapter 6).

Considerations by Mitchell in 1934 [15], Schiff and Thomas in 1935 [16], and Makinson in 1937 [17] predicted that the scattering potential of the lattice sites would be much smaller than the surface step potential in free electron metals. Therefore, surface photoemission would dominate over volume photoemission. Early experiments [18] seemed to confirm this, and thus photoemission was initially considered to be a surface effect.

However, developments in the band theory of solids and improved experimental techniques produced results incompatible with a surface photoelectric effect. In 1964 Gobel, Allen, and Kane [19] determined that the momentum and energy distributions of photoelectrons from single-crystal materials reflected the *bulk* band structure and not the structure of the surface levels. Other experiments

confirmed this, and photoemission came to be known as a volume effect. The volume effect was described in terms of a simple three step model [20]: (1) an electron absorbs a photon, gaining an energy $h\nu$, (2) the electron travels to the surface, and (3) the electron crosses the surface barrier and is emitted into the vacuum. The number of electrons emitted from the surface itself is considered to be negligible. Despite its simplicity, this model has been extremely successful in describing many photoemission experiments up to the present day.

Experiments with ultra-clean metal surfaces in the early 1970's, however, showed in some cases a measurable emission contribution from surface states [21], [22] which was not seen in earlier studies. More complex theories involving a superposition of the volume and surface electron wavefunctions were developed to include both the surface and volume emission processes [23]. Today photoemission is considered to be the sum of both a surface and volume photoelectric effect, although for metal samples without special surface preparation the volume emission will typically be dominant.

With the invention of the laser in 1960 [24], scientists found themselves with a high intensity, monochromatic light source which was readily applied to photoemission experiments. Using a Nd:glass laser Sonnenberg, Heffner, and Spicer produced the first 2-photon emission process from a Cs_3Sb cathode in 1964 [25]. As improved laser technologies led to increased intensities, 3-photon and higher order emission processes were observed [26].

The development of very short pulse lasers allowed scientists to perform time-resolved measurements on fast occurring processes in metals. In 1983 Eesley used pulses of 8 ps duration from a dye laser to demonstrate nonequilibrium heating of electrons in copper [27] and later used 65 fs dye laser pulses in measuring the

electron-lattice thermal relaxation time to be 2–3 ps in gold [28]. These studies suggested that thermionic emission and thermally enhanced photoemission may be significant in emission experiments utilizing high intensity short pulse lasers.

More recently, ultrashort pulse laser systems have been used to investigate image potential states in metals [29], surface-plasmon enhanced multiphoton emission [30], emission and electron spectroscopy from exotic materials such as diamond and fullerene [31], [32], and electron-spin polarization in photoemission processes [33]. In the studies described in this paper we utilized a synchronously pumped, mode-locked femtosecond dye laser system to continue such photoemission research. The following chapters will describe several experiments including the investigation of multicolor emission, the characterization of RF gun photocathodes, the measurement of photoemission from silicon, diamond, and fullerene, and the study of photoelectron dynamics in metals using thin copper films.

Chapter 3

Multiphoton and Multicolor Emission

In this chapter we discuss the experimental work that led to the first observation of multicolor photoemission from the Fermi electrons in a metal. This was achieved using a femtosecond dye laser system which is described in the following section.

3.1 Laser System

The light pulses used to produce photoemission in the following experiment are produced by a four stage dye laser system (Fig. 3.1). The first stage oscillator is a Coherent Antares Nd:YAG laser. This laser is actively mode-locked to produce a train of 1064 nm infrared pulses each having a temporal duration $\tau_{1/2}$ of 100 ps measured full width at half maximum (FWHM). The repetition rate is 76 MHz and the CW power of this beam is 25 W. The infrared pulses are sent through a Type II KTP crystal inside the laser head which converts about 10% of the infrared into 532 nm green pulses. These pulses are 70 ps long with a CW power of 2.5 W. The infrared and green are then separated by three dichroic mirrors and propagated out of the laser head.

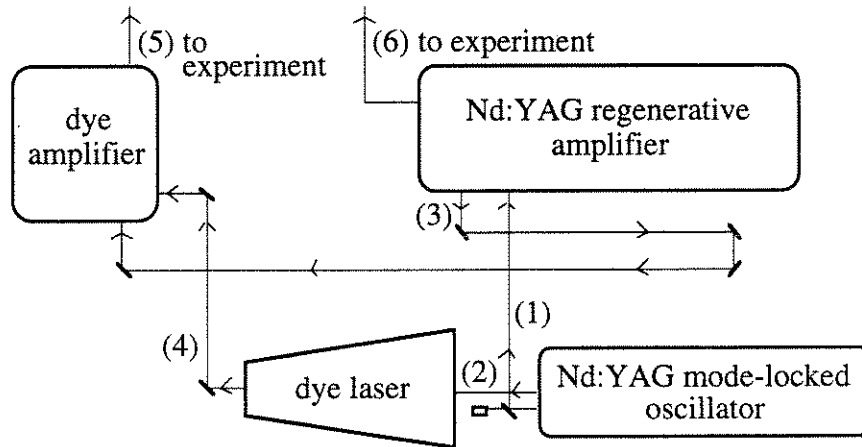


Figure 3.1: Four stage dye laser system. The beam characteristics are as follows: (1) $\lambda = 1064$ nm, $\tau_{1/2} = 100$ ps, $E = 10$ nJ, rep rate = 76 MHz; (2) $\lambda = 532$ nm, $\tau_{1/2} = 70$ ps, $E = 30$ nJ, rep rate = 76 MHz; (3) $\lambda = 532$ nm, $\tau_{1/2} = 70$ ps, $E = 50$ mJ, rep rate = 5 Hz; (4) $\lambda = 650$ nm, $\tau_{1/2} = 250$ fs, $E = 2$ nJ, rep rate = 76 MHz; (5) $\lambda = 650$ nm, $\tau_{1/2} = 500$ fs, $E = 2$ mJ, rep rate = 5 Hz; (6) $\lambda = 266$ nm, $\tau_{1/2} = 50$ ps, $E = 40$ mJ, rep rate = 5 Hz.

The green beam from the Antares is used to pump a Coherent Satori dye laser. This laser produces 650 nm, 250 fs red pulses at the mode-locking repetition rate of 76 MHz. The CW power of this beam is 150 mW, corresponding to an energy of 2 nJ per pulse. These pulses are then amplified in the following manner:

A fraction (~ 1 W) of the infrared beam from the Antares laser is used to seed a Continuum Nd:YAG regenerative amplifier. A single pulse is selected from this mode-locked pulse train by dual pockel cells and is amplified to an energy of 200 mJ. The pulse is then frequency doubled using a Type I KDP crystal to produce a 100 mJ, 70 ps pulse at 532 nm. The repetition rate of the regenerative amplifier is 5 Hz. This amplified green pulse is sent through a 50% beamsplitter and then propagated out of the laser head, through a delay line and into a Quantel PTA-60 three-stage dye amplifier. The delay line synchronizes the green pulses with the output of the Satori dye laser so that the energy of the green pulse pumps

each of the three dye cells to produce a population inversion and therefore gain just as a mode-locked Satori pulse propagates through the cells and extracts this gain. After the three dye cells the Satori pulse has been amplified by a factor of $\sim 10^6$. There is a factor of two temporal broadening of the pulses in the dye amplifier, and so the final output is 650 nm, 500 fs, 2 mJ pulses with a spot size of 7 mm in diameter at a rep rate of 5 Hz. This was the initial beam used in most of the photoemission experiments.

The regenerative amplifier also has a frequency quadrupling crystal (Type I KDP) which can double the frequency of the green to produce 266 nm, 50 ps, 40 mJ pulses at the 5 Hz rep rate. Quadrupled Nd:YAG pulses are commonly used to illuminate photocathodes for creating pulsed electron beams in various types of accelerators, thus we performed additional photoemission experiments using this output of the amplifier.

3.2 Multiphoton Photoemission Setup

The setup for the multiphoton emission experiment [34] is shown in Fig. 3.2. The output from the dye amplifier is sent first through a partially silvered variable attenuator wheel which controls the laser energy incident on the experiment. The beam then travels through a telescope which reduces the spot size to 3.5 mm. After the telescope the beam is incident on a 50% beamsplitter. The transmitted half of the beam travels along a variable delay line, through a 650/325 nm dichroic mirror, and enters the vacuum chamber through a laser port. The beam then propagates through the hollow anode and onto the sample at normal incidence. The vacuum chamber is maintained at a pressure of $\sim 10^{-6}$ torr by a turbomolecular pump.

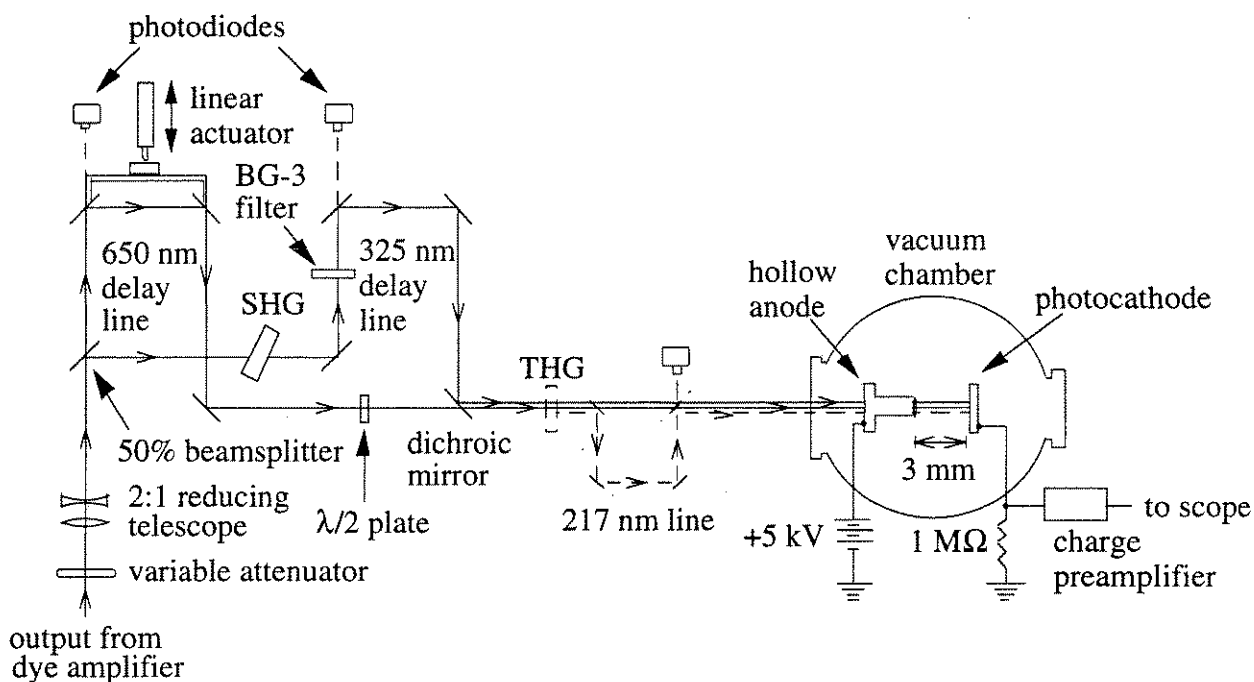


Figure 3.2: Multiphoton photoemission experiment.

The other half of the beam reflects from the beamsplitter and passes through a Type I KDP second harmonic generator (SHG) crystal which converts $\sim 10\%$ of the energy into 325 nm ultraviolet light. This process narrows the pulsewidth to 350 fs, and reduces the spot size to 2.5 mm. The beam then travels through a BG-3 filter which eliminates the residual 650 nm light; the remaining 325 nm light propagates along a fixed delay line (of approximately equal length to the variable red delay line) then reflects off the dichroic mirror through the vacuum chamber and onto the sample.

By placing a beam block in either delay line we can run a single-color 650 or 325 nm photoemission experiment. With no beam blocks in place we can overlap both wavelengths on the same point on the sample and use the linear actuator on the variable delay line to change the timing of one wavelength pulse with respect

to the other. This allows us to run a two-color photoemission experiment. We also have a Type I BBO third harmonic generator (THG) crystal which we can place after the dichroic mirror. This will generate 217 nm light when a 650 and a 325 nm pulse of the same polarization are sent simultaneously through it. Because the Type I SHG rotates the polarization of the 325 nm beam by 90° , it is necessary to place a half-wave plate in the 650 nm beam so that both wavelengths will have the same polarization in the THG crystal. The third harmonic generation will further narrow the pulsewidth to 290 fs and reduce the spot size to 2.0 mm. A series of four 217 nm mirrors then filters out the residual 650 and 325 nm light and sends the remaining 217 nm beam into the chamber and onto the sample for a single-color 217 nm photoemission experiment. Calibrated photodiodes are placed behind turning mirrors for each wavelength so that the laser pulse energy can be measured on each shot from the leakage through the mirrors.

For the pulsewidths and spotsizes given above, the peak laser intensity can be calculated from the measured pulse energy. For the three short-pulse wavelengths, the peak intensities corresponding to an energy of $1 \mu\text{J}$ are

$$650 \text{ nm: } 1 \mu\text{J} = 2.0 \times 10^7 \text{ W/cm}^2$$

$$325 \text{ nm: } 1 \mu\text{J} = 5.5 \times 10^7 \text{ W/cm}^2$$

$$217 \text{ nm: } 1 \mu\text{J} = 1.0 \times 10^8 \text{ W/cm}^2$$

The hollow anode is machined from copper and biased typically at +5 kV to collect all of the photoelectrons emitted from the sample. The distance between the anode and photocathode is ≤ 3 mm which gives an electric field for the hollow anode geometry of ≥ 1 MV/m on the sample surface. This field produces a $< 1\%$ reduction of the work function of copper through the Schottky effect (see Sec. 3.3.2). When photoelectrons leave the sample they are replenished from

ground through a $1\text{ M}\Omega$ load resistor. This amount of replenishing charge is equal to the charge that was emitted from the sample and is measured across the load resistor by a 1 pF capacitor inside an EG&G Ortec model 142 charge preamplifier. The preamplifier produces a signal proportional to this charge ($V = Q/C$) which sent to a digital oscilloscope and in turn to a computer data acquisition system. The polarity of this signal is negative for electrons emitted from the photocathode (or ions collected by the cathode) and positive for ions emitted from the photocathode (or electrons collected by the cathode).

The risetime of the preamplifier is 5 ns which is much longer than the picosecond and subpicosecond time scales over which the electron emission occurs in all of our experiments. Therefore, any transient displacement currents between the anode and cathode or between the cathode and the chamber walls will not be measured because the time integral of these currents is zero. Only the real charge which flows through the $1\text{ M}\Omega$ resistor will produce a signal from the preamplifier. This will be the total charge emitted by the photocathode during the laser shot.

Stray capacitance in the experiment (between the cathode and the chamber walls, for example) can effect the charge measurement by effectively adding to the 1 pF capacitance C of the preamplifier. However, measurements taken with another preamplifier having a 50 pF internal capacitor produced the same value for the measured charge. Thus the stray capacitance must be significantly smaller than 1 pF , and we have neglected it in our measurements.

3.3 Single-Color Photoemission

We will first discuss single-frequency photoemission data which was initially used to calibrate our experiment with previous studies of laser-produced single and

multiphoton photoelectric effect from bulk materials.

3.3.1 Emitted Charge vs. Incident Laser Energy

If the laser pulse does not significantly heat the electrons in the sample, then from Sec. 2.4.4 the n -photon current density is given by

$$J_n = c_n I^n \quad (3.1)$$

For this experiment our diagnostics measure the *total* emitted charge as a function of *total* energy per laser pulse. Thus we need to express Eq. 3.1 in terms of these measured quantities. If we assume a laser pulse which has a gaussian transverse profile as well as a gaussian temporal profile, the total energy can be found by integrating the intensity over the time and area of the pulse:

$$E = \int \int I(r, t) dt d\sigma \quad (3.2)$$

$$= \int_0^{2\pi} \int_0^\infty \int_{-\infty}^{+\infty} I_0 e^{-t^2/\tau^2} e^{-r^2/r_0^2} dt r dr d\theta \quad (3.3)$$

$$= \sqrt{\pi} I_0 \tau \pi r_0^2 \quad (3.4)$$

The total charge emitted during the n -photon process is then found by integrating the current density over time and area:

$$Q_n = \int \int J_n(r, t) dt d\sigma \quad (3.5)$$

$$= \int \int c_n I^n(r, t) dt d\sigma \quad (3.6)$$

$$= c_n I_0^n \int_0^{2\pi} \int_0^\infty \int_{-\infty}^{+\infty} e^{-nt^2/\tau^2} e^{-nr^2/r_0^2} dt r dr d\theta \quad (3.7)$$

$$= c_n \sqrt{\frac{\pi}{n}} I_0^n \tau \frac{\pi r_0^2}{n} \quad (3.8)$$

$$= \frac{c_n E^n}{\pi^{\frac{n-1}{2}} n^{3/2} \tau^{n-1} (\pi r_0^2)^{n-1}} \quad (3.9)$$

For a fixed laser pulsewidth and spot size, we can rewrite Eq. 3.9 in terms of a single coefficient b_n

$$Q_n = b_n E^n \quad (3.10)$$

Taking the logarithm of this equation gives

$$\log Q_n = \log b_n + n \log E \quad (3.11)$$

Thus if we plot the emitted charge versus the laser energy from our experiment on a log-log scale, we should obtain a straight line with slope n being an integer equal to the number of photons involved in the emission process.

3.3.2 Photoemission from Copper

The photon energies ($h\nu$), FWHM pulsewidths ($\tau_{1/2}$), and spot size diameters ($w_0 = 2r_0$) for the three laser wavelengths are summed up as follows:

λ	$h\nu$	$\tau_{1/2}$	w_0
650 nm	1.9 eV	500 fs	3.5 mm
325 nm	3.8 eV	350 fs	2.5 mm
217 nm	5.7 eV	290 fs	2.0 mm

Because the work function of copper is 4.6 eV, an electron near the Fermi level will require one 217 nm photon, two 325 nm photons, or three 650 nm photons in order to have sufficient energy to escape the metal (Fig. 3.3).

The copper photocathode was a one-inch diameter flat copper mirror from Spawr Industries polished to $\lambda/20$ at 10.6 μm . The photoemission results from the three wavelengths incident on this sample are shown in Fig. 3.4. Below 1 pC the emission curves are straight lines on a log-log scale as predicted by Eq. 3.11.

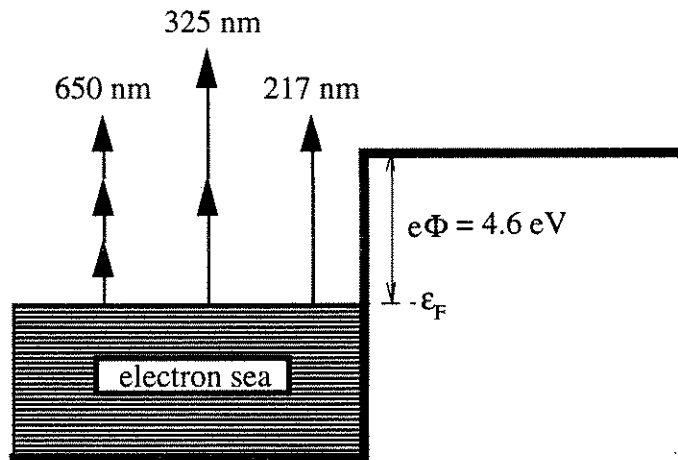


Figure 3.3: Photoelectric transitions in copper from the three wavelengths available in the multiphoton emission experiment. The photon energies are as follows: $h\nu_{650} = 1.9$ eV, $h\nu_{325} = 3.8$ eV, $h\nu_{217} = 5.7$ eV.

The 217 nm curve has slope = 1, the 325 nm curve has slope = 2, and the 650 nm curve has slope = 3 indicating a 1-, 2-, and 3-photon effect respectively. Because the data points form lines of the correct integer slopes, we can conclude that below 1 pC there is no measurable electron heating by the laser and thus the photoemission is due entirely to the n -photon photoelectric effect.

Space Charge Effects

Above 1 pC the lines bend due to space charge effects. As the first electrons leave the metal they create an electric field which tends to push the next bunch of electrons back into the metal. When this electric field becomes comparable to the applied field of the anode, the emitted charge will be suppressed.

The magnitude of this space charge field can be estimated by considering the escaping electrons to form sheets of charge having the same gaussian spatial and temporal profile as the laser pulse. The electric field of such a charge distribution

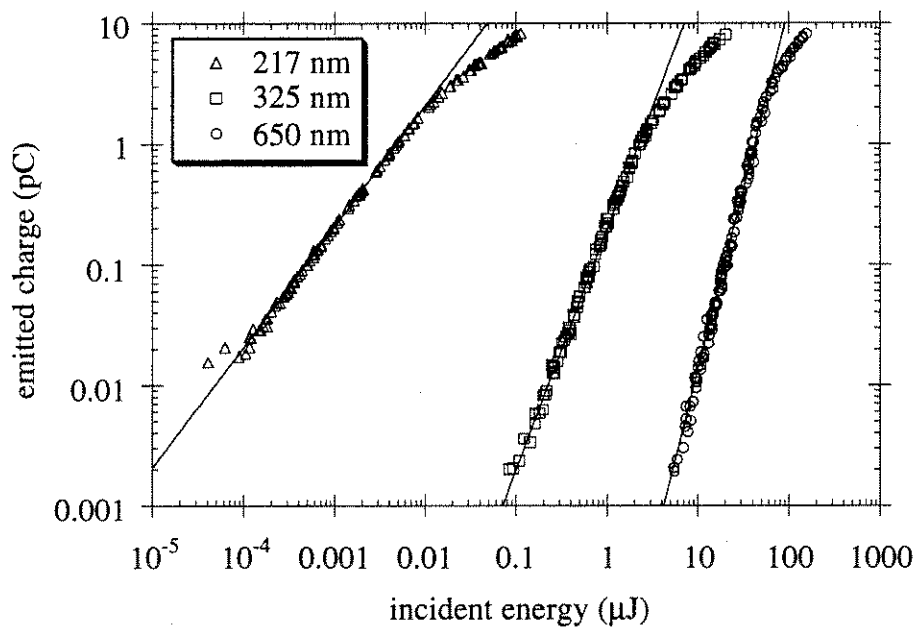


Figure 3.4: Charge vs. energy curves for the three laser wavelengths incident on copper. The solid lines represent slopes 1, 2, and 3 for the 217 nm, 325 nm, and 650 nm curves respectively. Above 1 pC the curves bend due to space charge saturation.

will be

$$\mathbf{E}(r, t) = \frac{\sigma(r, t)}{2\epsilon_0} \hat{z} = -\frac{Qe^{-t^2/\tau^2} e^{-r^2/\tau_0^2}}{2\epsilon_0\sqrt{\pi\tau\pi r_0^2}} \hat{z} \quad (3.12)$$

where σ is the charge per area of the sheet, ϵ_0 is the permittivity of free space ($8.85 \times 10^{-12} \text{ C}^2/[\text{J}\cdot\text{m}]$) and Q is the total charge emitted during the laser pulse. The magnitude of the maximum field at the center of the illuminated spot during the latest part of the laser pulse will be

$$|\mathbf{E}| = \frac{Q}{2\epsilon_0\pi r_0^2} \quad (3.13)$$

For our laser spotsizes and a total emitted charge of 1 pC the maximum space charge field is on the order of

$$|\mathbf{E}| \approx 0.01 \text{ MV/m}$$

The space charge field is small compared to the 1 MV/m applied field and from this calculation we would not expect to see bending of the charge curves at 1 pC. Therefore, the emission from the copper surface may be nonuniform which could greatly enhance the space charge fields at localized “hot” emission spots.

Determination of a_n , b_n , and η

From the data we can determine the b_n coefficients of Eq. 3.10 for each color. They are as follows:

$$217 \text{ nm: } b_1 = 210 \text{ pC}/\mu\text{J}$$

$$325 \text{ nm: } b_2 = 0.20 \text{ pC}/\mu\text{J}^2$$

$$650 \text{ nm: } b_3 = 1.4 \times 10^{-5} \text{ pC}/\mu\text{J}^3$$

To calculate the a_n coefficients of Eq. 2.31 from our b_n measurements we use Eqs. 2.31, 3.1, 3.9, and 3.10:

$$a_n = \frac{\pi^{\frac{n-1}{2}} n^{3/2} (h\nu)^n \tau^{n-1} (\pi r_0^2)^{n-1}}{A e^n (1-R)^n T^2 F\left(\frac{nh\nu - e\Phi}{kT}\right)} b_n \quad (3.14)$$

For gaussian pulses, the e -folding time τ is related to the FWHM time $\tau_{1/2}$ by

$$\tau = \frac{\tau_{1/2}}{2\sqrt{\ln 2}} \quad (3.15)$$

and so we can use this plus the relation between spot radius and diameter ($r_0 = w_0/2$) to write Eq. 3.14 in terms of measured quantities $\tau_{1/2}$ and w_0 :

$$a_n = \frac{\pi^{\frac{3n-3}{2}} n^{3/2} (h\nu)^n \tau_{1/2}^{n-1} w_0^{2n-2}}{2^{3n-3} (\ln 2)^{\frac{n-1}{2}} A e^n (1-R)^n T^2 F\left(\frac{nh\nu - e\Phi}{kT}\right)} b_n \quad (3.16)$$

The reflection coefficients for copper at these wavelengths are [35]

$$\begin{aligned} R_{217} &= 0.390 \\ R_{325} &= 0.387 \\ R_{650} &= 0.943 \end{aligned}$$

and the Fowler function values for copper at room temperature are

$$\begin{aligned} F\left(\frac{h\nu_{217} - e\Phi_{Cu}}{kT_{room}}\right) &= F(43) = 910 \\ F\left(\frac{2h\nu_{325} - e\Phi_{Cu}}{kT_{room}}\right) &= F(116) = 6700 \\ F\left(\frac{3h\nu_{650} - e\Phi_{Cu}}{kT_{room}}\right) &= F(43) = 910 \end{aligned}$$

Plugging these values, our laser pulse parameters, and our measured values of b_n into Eq. 3.16 gives the a_n coefficients for copper

$$\begin{aligned} 217 \text{ nm: } a_1 &= 2.0 \times 10^{-13} \text{ cm}^2\text{s/C} \\ 325 \text{ nm: } a_2 &= 5.5 \times 10^{-24} \text{ cm}^4\text{s}^2/\text{C}^2 \\ 650 \text{ nm: } a_3 &= 6.9 \times 10^{-31} \text{ cm}^6\text{s}^3/\text{C}^3 \end{aligned}$$

For linear photoemission processes, a more useful quantity is the absolute quantum efficiency η of a material. This quantity is the number of emitted electrons per incident photon and can be calculated from our b_1 coefficient by

$$\eta = \frac{h\nu}{e} b_1 \times 10^{-6} \text{ electrons/photon} \quad (3.17)$$

For our measurement of 217 nm light on copper we obtain a quantum efficiency of

$$\eta_{217} = 1.2 \times 10^{-3} \text{ electrons/photon}$$

Charge Enhancement Due to the Applied Electric Field

So far we have not considered the possibility of charge enhancement due to the applied electric field on the photocathode. In general, an electric field \mathbf{E} at the surface of a metal will lower the metal work function to an effective value of

$$\Phi_{eff} = \Phi_0 - \left(\frac{e|\mathbf{E}|}{4\pi\epsilon_0} \right)^{1/2} \quad (3.18)$$

where Φ_0 is the work function at zero applied field. This is known as the Schottky effect [36].

For the 1 MV/m field produced by the +5 kV bias on the anode, the energy barrier of the copper cathode surface is lowered to

$$e\Phi_{eff} = 4.56 \text{ eV}$$

which is a change of $< 1\%$. This change in work function has the following effect on the Fowler function values for the three wavelengths:

$$\begin{aligned} F\left(\frac{h\nu_{217} - e\Phi_{eff}}{kT_{room}}\right) &= F(44) = 970 \\ F\left(\frac{2h\nu_{325} - e\Phi_{eff}}{kT_{room}}\right) &= F(118) = 6900 \\ F\left(\frac{3h\nu_{650} - e\Phi_{eff}}{kT_{room}}\right) &= F(44) = 970 \end{aligned}$$

The Fowler function values change by $< 7\%$, and therefore we can ignore the Schottky effect for photoemission from copper at these wavelengths.

3.4 Multicolor Photoemission

In addition to the single-color transitions discussed in Sec. 3.3, multicolor photoemission may also be possible (Fig. 3.5). For the wavelengths available in this experiment such photoelectric transitions could be due to the absorption of one 650 nm photon + one 325 nm photon, or two 650 nm photons + one 325 nm photon.

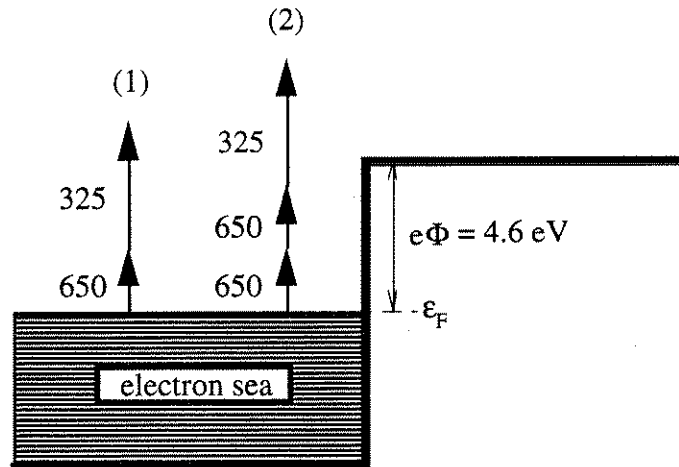


Figure 3.5: Two-color transitions in copper. For this experiment the possible transitions are (1) one 650 nm photon + one 325 nm photon or (2) two 650 nm photons + one 325 nm photon.

To investigate such transitions, we set up the two-color photoemission experiment described in Sec. 3.2. The 650 nm and 325 nm pulses were sent colinearly onto the same point on the sample (the 217 nm crystal and mirrors were removed for this experiment). A precise overlap of the two beams was attained by removing the BG-3 filter in the 325 nm delay line and propagating the unamplified red

Satori beams from both delay lines ~ 10 meters across the room onto a screen using a turning mirror placed just before the vacuum chamber. (Without amplification there is no second harmonic generation and thus there is only 650 nm light in both delay lines.) We then adjusted the alignment of the beams until the two red spots on the screen overlapped and the interference fringes between the two beams were eliminated. This left a single spot which would blink on and off as room vibrations would shift the phase between the two colinear beams. Once this overlap was complete we removed the turning mirror, replaced the BG-3 filter, and sent the amplified 650 nm and 325 nm beams onto the sample. By moving the linear actuator in the 650 nm delay line we could change the relative timing of the two pulses on the photocathode.

When the two pulses do not overlap in time, the total measured charge will simply be the sum of the emitted charge from each pulse:

$$Q_{tot} = Q_2 + Q_3 \quad (3.19)$$

$$= b_2 E_{325}^2 + b_3 E_{650}^3 \quad (3.20)$$

However, when the two pulses do overlap in time the multicolor transitions become possible and we may observe additional charge arising from the $1_{650} + 1_{325}$ transition or the $2_{650} + 1_{325}$ transition (or possibly both). The total charge in this case is

$$Q_{tot} = Q_2 + Q_3 + Q_{1+1} + Q_{2+1} \quad (3.21)$$

If both the spatial and temporal peaks of the two gaussian pulses are overlapped, Q_{1+1} will be given by

$$Q_{1+1} = c_{1+1} \int \int I_{650}(r, t) I_{325}(r, t) dt d\sigma \quad (3.22)$$

$$= c_{1+1} I_{0650} I_{0325} \int_0^{2\pi} \int_0^\infty \int_{-\infty}^{+\infty} e^{-t^2/\tau_{650}^2} e^{-t^2/\tau_{325}^2} e^{-r^2/r_{0650}^2} \times e^{-r^2/r_{0325}^2} dt r dr d\theta \quad (3.23)$$

$$= c_{1+1} \pi^{3/2} I_{0650} I_{0325} \left(\frac{\tau_{650} \tau_{325}}{\sqrt{\tau_{650}^2 + \tau_{325}^2}} \right) \left(\frac{r_{0650}^2 r_{0325}^2}{r_{0650}^2 + r_{0325}^2} \right) \quad (3.24)$$

$$= \frac{c_{1+1} E_{650} E_{325}}{\pi^{3/2} (r_{0650}^2 + r_{0325}^2) \sqrt{\tau_{650}^2 + \tau_{325}^2}} \quad (3.25)$$

$$= b_{1+1} E_{650} E_{325} \quad (3.26)$$

and similarly Q_{2+1} will be

$$Q_{2+1} = c_{2+1} \int \int I_{650}^2(r, t) I_{325}(r, t) dt d\sigma \quad (3.27)$$

$$= \frac{c_{2+1} E_{650}^2 E_{325}}{\pi^3 r_{0650}^2 (r_{0650}^2 + 2r_{0325}^2) \tau_{650} \sqrt{\tau_{650}^2 + 2\tau_{325}^2}} \quad (3.28)$$

$$= b_{2+1} E_{650}^2 E_{325} \quad (3.29)$$

The result of this two-color time delay experiment is shown in Fig. 3.6. Clearly there is an enhancement in emitted charge when the two pulses overlap in time on the cathode. Note the asymmetry of the baseline on either side of the peak—we will return to this issue later. Our next step is to determine whether the Q_{1+1} or Q_{2+1} process is responsible for this additional charge.

Because Q_{2+1} is a higher order process (requiring three photons) than the Q_{1+1} process (requiring only two photons) the probability of an electron absorbing the $2_{650} + 1_{325}$ photons is lower than that of absorbing $1_{650} + 1_{325}$ photons. However, the number of available electrons for photoemission (which is proportional to the Fowler function) is greater for Q_{2+1} than for Q_{1+1} :

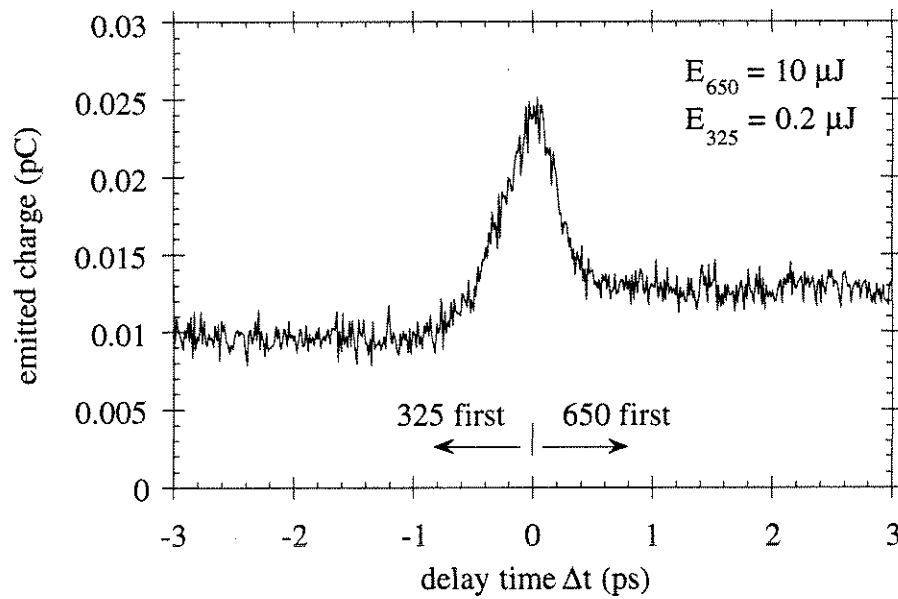


Figure 3.6: Emitted charge vs. delay time between the 650 nm and 325 nm pulses. For $\Delta t < 0$ the 325 nm pulse was incident on the cathode first, for $\Delta t > 0$ the 650 nm pulse was incident first, and for $\Delta t = 0$ the two pulses reached the cathode simultaneously. The energies of the two pulses were fixed at $E_{650} = 10 \mu\text{J}$ and $E_{325} = 0.2 \mu\text{J}$.

$$F\left(\frac{2h\nu_{650}+h\nu_{325}-e\Phi_{C_{1+1}}}{kT_{room}}\right) = F(120) = 6700$$

$$F\left(\frac{h\nu_{650}+h\nu_{325}-e\Phi_{C_{1+1}}}{kT_{room}}\right) = F(43) = 910$$

That is, the excitation energy in the Q_{2+1} process ($2h\nu_{650} + h\nu_{325} = 7.6$ eV) is greater than the excitation energy in the Q_{1+1} process ($h\nu_{650} + h\nu_{325} = 5.7$ eV) and therefore the former can dig deeper below the Fermi level to extract photoelectrons.

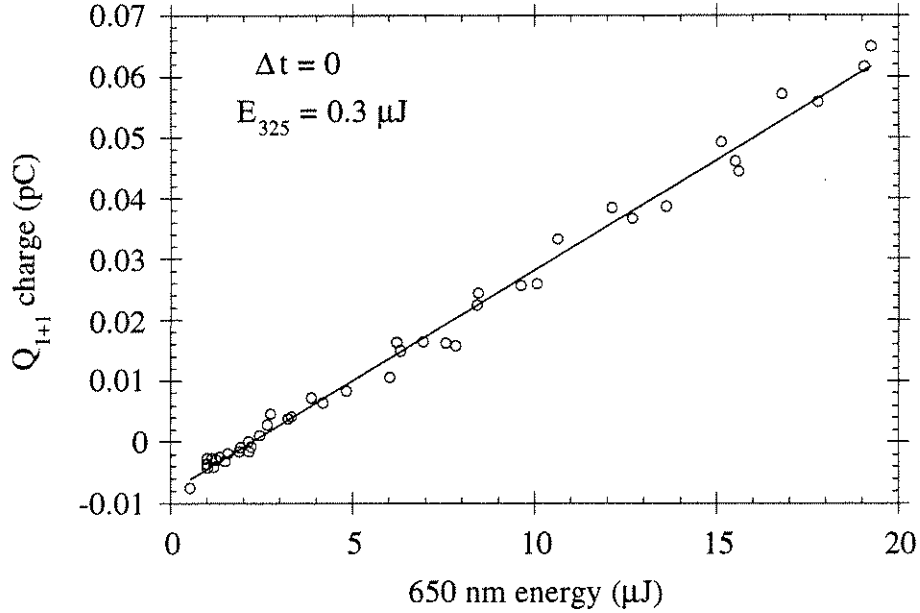


Figure 3.7: Enhanced charge vs. 650 nm energy for $\Delta t = 0$ and 325 nm energy fixed at $E_{325} = 0.3 \mu\text{J}$. The relationship is linear, indicating a Q_{1+1} process. The offset of the line is due to inaccuracies in the b_2 and b_3 coefficients used to calculate the enhanced charge.

To make a determination between these two processes we set the delay time $\Delta t = 0$, fixed the 325 nm pulse energy, and measured the enhanced charge vs. 650 nm pulse energy. The enhanced charge is found by subtracting the expected charge due to the 2- and 3-photon emission from the total charge measured at

the peak:

$$Q_{enh} = Q_{tot} - (b_2 E_{325}^2 + b_3 E_{650}^3) \quad (3.30)$$

If Q_{1+1} is dominant we should see a linear relationship between the enhanced charge and the 650 nm energy:

$$Q_{1+1} = (b_{1+1} E_{325}) E_{650} \quad (3.31)$$

If Q_{2+1} is the dominant process, however, the relationship between the enhanced charge and the 650 nm energy should be quadratic:

$$Q_{2+1} = (b_{1+1} E_{325}) E_{650}^2 \quad (3.32)$$

The results are shown in Fig. 3.7. Clearly, the relationship is linear and we can conclude that the Q_{1+1} process is responsible for the enhanced charge which produces the $\Delta t = 0$ peak in Fig. 3.6. Thus the total emitted charge is

$$Q_{tot} = Q_2 + Q_3 + Q_{1+1} \quad (3.33)$$

We can determine the coefficient b_{1+1} by measuring the value of the slope of the line in Fig. 3.7 (slope = $b_{1+1} E_{325}$) for several different values of E_{325} . The results are shown in Fig. 3.8. This method yields a value of $b_{1+1} = 0.011 \text{ pC}/\mu\text{J}^2$.

Of course, from Eq. 3.31 the Q_{1+1} process should also be linear in E_{325} . To verify this, we kept the 650 nm energy fixed and measured the enhanced charge at $\Delta t = 0$ vs. the 325 nm energy. Fig. 3.9 shows that this is indeed the case. As before, we can measure this slope (equal to $b_{1+1} E_{650}$) for different values of E_{650} . These results are shown in Fig. 3.10. From this graph we calculate the value of b_{1+1} to be $0.0095 \text{ pC}/\mu\text{J}^2$. This is within 15% of the value obtained with the previous method.

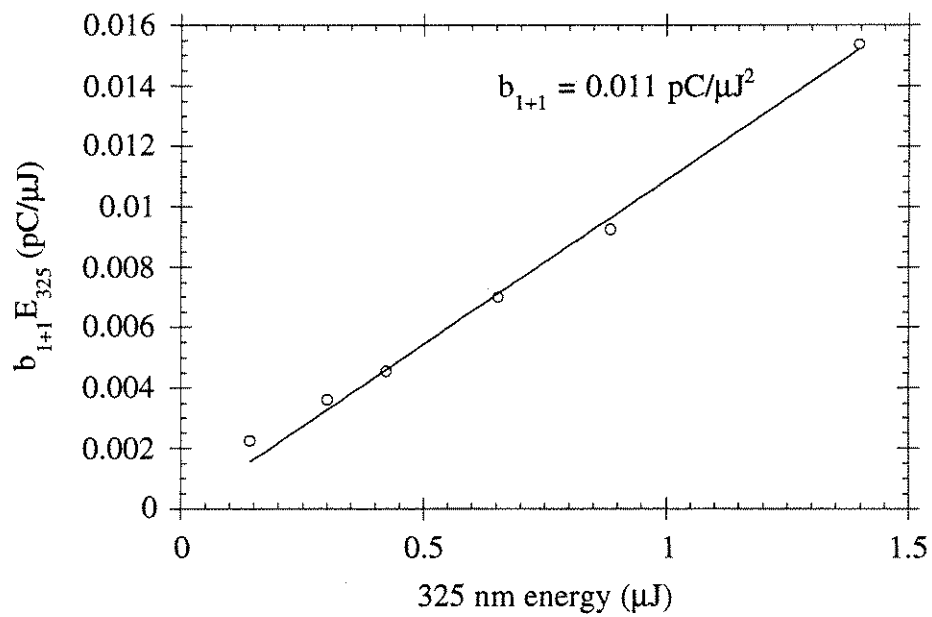


Figure 3.8: Values of $b_{1+1}E_{325}$ vs. E_{325} . The slope of this line gives the value of b_{1+1} to be $0.011 \text{ pC}/\mu\text{J}^2$.

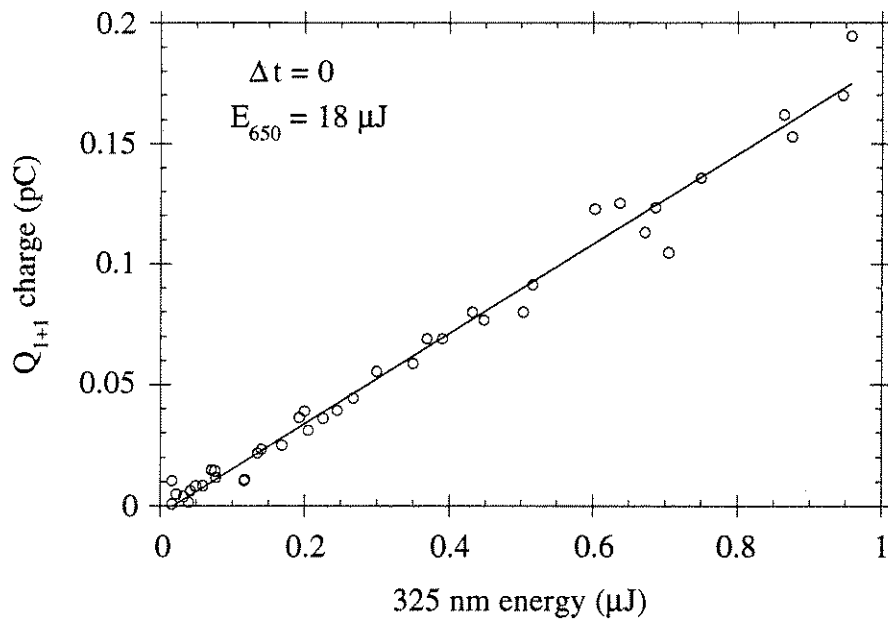


Figure 3.9: Enhanced charge vs. 325 nm energy for $\Delta t = 0$ and 650 nm energy fixed at $E_{650} = 18 \mu\text{J}$.

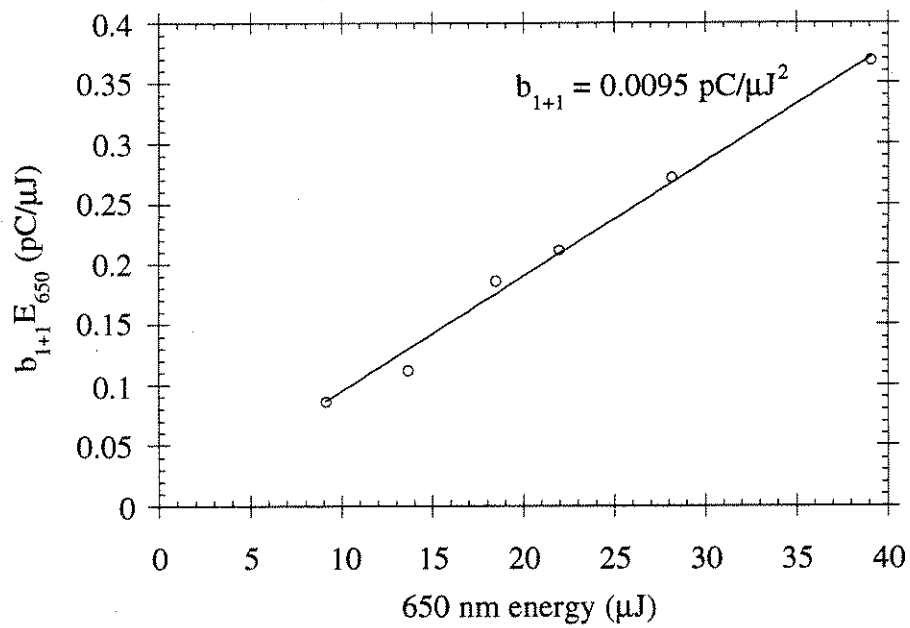


Figure 3.10: Values of $b_{1+1}E_{650}$ vs. E_{650} . The slope of this line gives the value of b_{1+1} to be $0.0095 \text{ pC}/\mu\text{J}^2$.

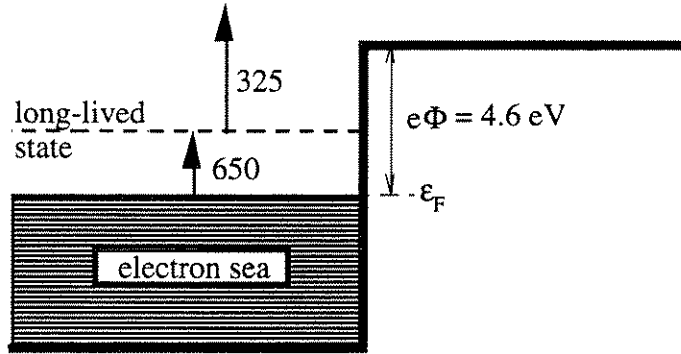


Figure 3.12: Two-color photoemission by coupling to a long-lived energy state of the cathode. The 650 nm photons populate the state and then the 325 nm photons free these electrons from the metal.

A more likely explanation is that the 650 nm photons are coupling electrons to a relatively long-lived energy state in the cathode. The 650 nm pulse populates this state and then the 325 nm pulse couples these electrons to the free states outside the metal (Fig. 3.12). Metallic energy states, however, typically have lifetimes less than a picosecond [38] as do image potential states [29]. Semiconductor states, on the other hand, can have lifetimes of hundreds of picoseconds. Because our copper cathodes have all been exposed to air, they will have a thin copper oxide layer on the surface. Therefore, it may be a copper oxide semiconductor state which is responsible for the enhancement of charge after the peak. In order for the 650 nm photons to populate the state and the 325 nm photons to liberate the electrons, such a state must lie between 0.8 and 1.9 eV above the copper Fermi level.

We must include the charge Q_u due to this long-lived state in our determination of b_{1+1} . The total charge emitted at $\Delta t = 0$ is then

$$Q_{tot} = Q_2 + Q_3 + Q_{1+1} + Q_u \quad (3.34)$$

From Figs. 3.6 and 3.11 the charge Q_u is responsible for $\sim 30\%$ of the charge

at the peak, thus our measured values of b_{1+1} must be reduced by this amount. Averaging the two values found earlier for b_{1+1} and reducing by the 30% gives

$$b_{1+1} = 7.0 \times 10^{-3} \text{ pC}/\mu\text{J}^2$$

We can derive an expression for a_{1+1} in terms of b_{1+1} using Eqs. 2.43, 2.44, 3.15, 3.25, and 3.26:

$$a_{1+1} = \frac{\pi^{3/2} h\nu_{650} h\nu_{325} (w_{0650}^2 + w_{0325}^2) \sqrt{\tau_{1/2650}^2 + \tau_{1/2325}^2}}{8\sqrt{\ln 2} A e^2 (1 - R_{650})(1 - R_{325}) T^2 F\left(\frac{h\nu_{650} + h\nu_{325} - e\Phi}{kT}\right)} b_{1+1} \quad (3.35)$$

Plugging in our experimental parameters yields

$$a_{1+1} = 1.4 \times 10^{-23} \text{ cm}^4\text{s}^2/\text{C}^2$$

Note that the value obtained earlier for a_2 is the same order of magnitude ($\sim 40\%$) of the value for a_{1+1} . Thus

$$a_{1+1} \approx a_2$$

as we may expect because both are 2-photon processes and the a_n coefficients are (approximately) independent of the photon wavelength.

A final observation about multicolor emission is that both the 650 and 325 nm pulses had to be kept at relatively low energies ($E_{650} < 20 \mu\text{J}$ and $E_{325} < 1 \mu\text{J}$) in order to observe the 2-color emission. At higher energies the 3-photon emission from the 650 nm pulses or the 2-photon emission from the 325 nm pulses dominate the total emitted charge and obscure the 2-color emission. Therefore this process cannot be used in applications which require the production of large amounts of charge.

However, multiphoton emission may prove useful as a method of overlapping two or more ultrashort (subpicosecond) laser pulses in space and time. Non-linear crystals are typically used to overlap laser pulses, but they are usually limited to harmonic wavelengths due to phase matching constraints. Multicolor photoemission has no such constraints. In principle by choosing a photocathode material with an appropriate work function several nonharmonic laser pulses could be synchronized by finding and then maximizing the multicolor emission peak (Fig. 3.6).

Chapter 4

RF Gun Photocathode Tests

Radio-frequency (RF) photoinjector guns have been developed as a means of generating short electron bunches for use in particle accelerators [39]. Conventional RF accelerators use a thermionic cathode placed in an RF accelerating structure which continuously emits electrons when heated. These electrons can become grouped at each peak of the RF cycle and accelerated as a train of microbunches by the fields of the RF wave. A photoinjector gun, however, uses a short laser pulse incident on a cathode to produce a single bunch of electrons through the process of photoemission. The laser pulse is synchronized with the RF cycle so that the electron bunch achieves maximum acceleration and minimum energy spread as it propagates down the structure. Because the photoelectrons are initially produced in one very short bunch, higher peak currents can be achieved with an RF photoinjector than with conventional RF accelerators.

Of course, the performance of a photoinjector gun is dependent on the performance of the photocathode. To obtain high peak currents, a photocathode material should be chosen which has a high quantum efficiency η at the laser wavelength. It must also be robust enough to withstand the high RF fields and

high incident laser intensities that are present in the RF gun environment. Finally, to achieve a high beam emittance from the gun the cathode should have a smooth, nonreactive surface for uniform emission over long periods of operation.

Two types of materials are generally used in these RF guns: metals and alkali photocathodes [40]. The alkali photocathodes include alkali halides such as CsI and Cs₂Te and alkali antimonides such as Cs₃Sb and K₃Sb. These photocathodes have high quantum efficiencies ($\eta = 10^{-2}$ – 10^{-1}) but are extremely sensitive to contamination and therefore require an operating vacuum of greater than 10^{-9} torr. Even in such a vacuum their quantum efficiencies generally decrease over periods of hours or days and thus they need to be reconditioned or replaced frequently. Metal photocathodes have lower quantum efficiencies ($\eta = 10^{-5}$ – 10^{-3}) but are less reactive and as a result have lower vacuum requirements and longer lifetimes.

Copper and magnesium are two common metal photocathode materials. Because the work function of pure copper is 4.6 eV, ultraviolet laser pulses are required for linear photoemission. In the RF photoinjector gun at UCLA these pulses are created by frequency quadrupling an amplified Nd:YAG laser pulse to obtain 266 nm radiation ($h\nu = 4.7$ eV). Pure magnesium, on the other hand, has a work function of 3.7 eV and therefore may exhibit a higher electron yield than copper at this wavelength. However, magnesium is more reactive than copper and subject to greater surface contamination. Such contamination can hinder photoemission by absorbing incident photons and by preventing photoexcited electrons from escaping the surface.

4.1 Quantum Efficiency and the Effects of Laser Damage

In order to study photoemission properties of these two metals before installing a copper or magnesium cathode into the UCLA RF photoinjector [41], we devised a DC field test gun using the basic setup from the short pulse multiphoton emission experiment (Fig. 4.1). In this case the incident laser pulses are from the frequency quadrupled output of the Nd:YAG regenerative amplifier (see Sec. 3.1). These pulses have a wavelength of 266 nm, a FWHM pulsewidth of 50 ps, and a spot size diameter of 3 mm after a 2:1 reducing telescope. A focusing lens could be placed before the chamber to reduce the spot size down to a minimum of $\sim 100 \mu\text{m}$. The photocathode samples were mounted on a positioning feedthrough so that the sample could be moved during the experiment to illuminate different points on the surface.

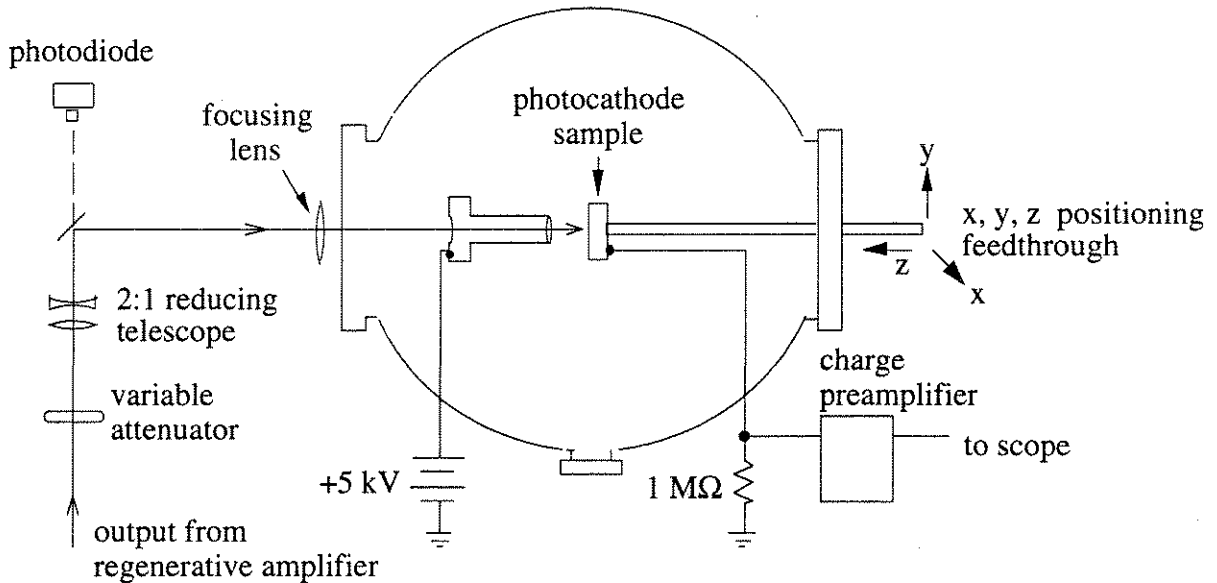


Figure 4.1: Setup for the DC test gun experiment.

As before, the anode was biased at +5 kV resulting in an applied field on the

order of 1 MV/m. In an actual RF gun the fields are approximately 100 MV/m, and therefore the Schottky effect will significantly alter the electron emission. At such high fields the effective work function of copper will become (from Eq. 3.18)

$$e\Phi_{eff} = 4.22 \text{ eV}$$

The Fowler function will therefore be changed from its zero field value for 266 nm incident radiation

$$F\left(\frac{h\nu_{266} - e\Phi_{Cu}}{kT_{room}}\right) = F(2.3) = 4.4$$

to a field enhanced value of

$$F\left(\frac{h\nu_{266} - e\Phi_{eff}}{kT_{room}}\right) = F(17) = 150$$

Thus the fields in the RF gun should increase the effective quantum efficiency of copper by about a factor of 30.

For the 1 MV/m field in the DC test gun, the energy barrier of copper is lowered to a value of

$$e\Phi_{eff} = 4.56 \text{ eV}$$

which corresponds to a Fowler function value of

$$F\left(\frac{h\nu_{266} - e\Phi_{eff}}{kT_{room}}\right) = F(3.8) = 8.8$$

At 266 nm incident radiation, even the modest field of the DC test gun will increase the emission from copper by about a factor of two.

4.1.1 Copper Measurements

We first looked at the emission characteristics of copper at 266 nm wavelength (Fig. 4.2). The cathode was a 1" diameter oxygen-free high-conductivity (OFHC) copper sample with a surface hand polished to 1 μm smoothness. The charge measurements were taken without the focusing lens in place and thus the spot size on the cathode was the full 3.0 mm diameter. The electron yield b_1 and corresponding quantum efficiency η_{266} (Eq. 3.17) were measured to be

$$\begin{aligned} b_1 &= 2.2 \text{ pC}/\mu\text{J} \\ \eta_{266} &= 1.0 \times 10^{-5} \end{aligned}$$

This value of b_1 measured at 266 nm incident wavelength can be used as a second method for determining the a_1 coefficient of copper—previously determined to be $2.0 \times 10^{-13} \text{ cm}^2\text{s}/\text{C}$ from the 217 nm measurement in Sec. 3.3.2. Using Eq. 3.16 with the Fowler function adjusted for the Schottky effect and the reflection coefficient for copper at 266 nm [35]

$$R_{266} = 0.337$$

we obtain

$$a_1 = 1.6 \times 10^{-13} \text{ cm}^2\text{s}/\text{C}$$

which is in good agreement (within 20%) with the previously obtained value.

For our next step we placed the focusing lens before the chamber to reduce the laser spot size to $\sim 100 \mu\text{m}$ and sent 266 nm pulses of 1 mJ energy onto the sample to create a small damaged spot on the surface. After damaging the sample the focusing lens was removed and a second charge measurement was taken. The new electron yield and quantum efficiency (measured below the space

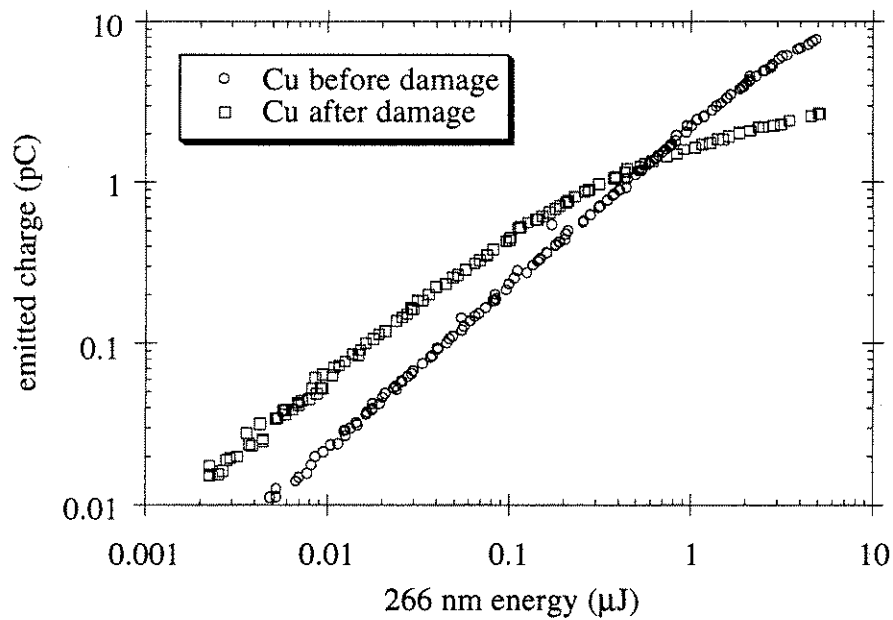


Figure 4.2: Electron yield of copper before and after laser damage. Before damage the yield is $b_1 = 2.2 \text{ pC}/\mu\text{J}$, corresponding to a quantum efficiency of $\eta_{266} = 1.0 \times 10^{-5}$. After damage the yield increases to $b_1 = 5.8 \text{ pC}/\mu\text{J}$, which is a quantum efficiency of $\eta_{266} = 2.7 \times 10^{-5}$. Note that space charge effects are much stronger after damage; this indicates that the emission is coming from a smaller area than before.

charge bending) were

$$\begin{aligned}b_1 &= 5.8 \text{ pC}/\mu\text{J} \\ \eta_{266} &= 2.7 \times 10^{-5}\end{aligned}$$

Thus after damaging, the yield has increased by nearly a factor of three. However, from Fig. 4.2 it is clear that space charge effects have become more prominent. This indicates that most of the emission is now coming from a smaller area on the surface even though the laser spot size has not changed. Apparently the emission from the damaged area has increased dramatically and now represents the majority of the charge emitted over the entire 3 mm diameter illumination area. There are two factors which may contribute to this enhanced emission from the damaged area: (1) in damaging the surface the laser may have ablated the layers of copper oxide and other contaminants exposing a cleaner copper surface, and (2) the damaged area may have sharp protrusions which would locally enhance the electric field from the anode bias and therefore increase emission due to the Schottky effect. Although damaging the cathode surface results in a higher electron yield, the uniformity of emission seems to be degraded and thus laser damage should be avoided for an RF gun photocathode where high emittance is an important factor in the overall gun performance.

4.1.2 Magnesium Measurements

The same experiment was then performed on magnesium. This sample was a 1" diameter 95% Mg-Zn-Al alloy also polished to 1 μm smoothness. The results are shown in Fig. 4.3. Initially, the electron yield of magnesium was

$$\begin{aligned}b_1 &= 0.15 \text{ pC}/\mu\text{J} \\ \eta_{266} &= 7.0 \times 10^{-7}\end{aligned}$$

This is less than 7% of the yield from copper. However, after damaging the sample as before the magnesium yield increased dramatically to

$$\begin{aligned} b_1 &= 33 \text{ pC}/\mu\text{J} \\ \eta_{266} &= 1.5 \times 10^{-4} \end{aligned}$$

This is an increase by a factor of 220. Once again the damaged sample yield shows a stronger space charge effect indicating large emission from the smaller damaged area. Over time, however, the electron yield began to decrease until after 15 minutes it stabilized at a value of

$$\begin{aligned} b_1 &= 10 \text{ pC}/\mu\text{J} \\ \eta_{266} &= 4.7 \times 10^{-5} \end{aligned}$$

Thus we see the effects of the high reactivity of magnesium. Even in a vacuum of 10^{-6} torr the surface quickly contaminated immediately following the laser ablation. Although magnesium can be cleaned to give a higher quantum efficiency than copper, it is subject to greater surface contamination and its yield is therefore less stable than copper, which showed no signs of electron yield degradation over time in the DC gun.

4.2 Effects of the RF Gun Environment

In an RF photoinjector gun, the cathode is exposed to many adverse physical conditions: extreme RF fields, high voltage arcing during conditioning, impurities in the vacuum, and repetitive incident ultraviolet laser shots. These factors may induce physical changes on the surface of the photocathode which modify its photoemission characteristics. Such changes were in fact observed for copper cathodes in the UCLA RF gun [42].

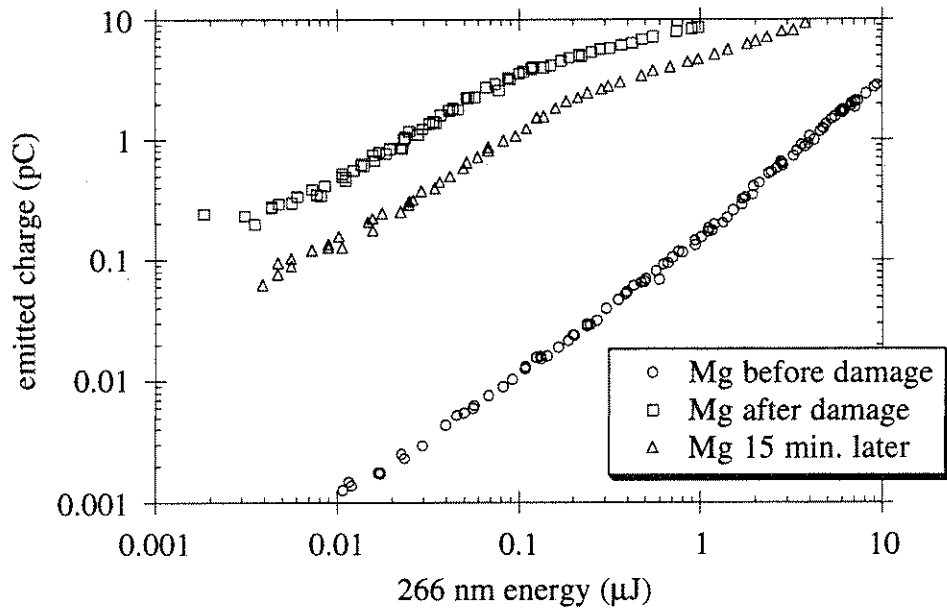


Figure 4.3: Electron yield of magnesium before and after laser damage. Before damage the yield is $b_1 = 0.15 \text{ pC}/\mu\text{J}$, corresponding to a quantum efficiency of $\eta_{266} = 7.0 \times 10^{-7}$. After damage the yield increases by a factor of 220 to $b_1 = 33 \text{ pC}/\mu\text{J}$ ($\eta_{266} = 1.5 \times 10^{-4}$). After 15 minutes, however, the yield decays to $b_1 = 10 \text{ pC}/\mu\text{J}$ ($\eta_{266} = 4.7 \times 10^{-5}$).

In an attempt to understand the nature of these emission changes, the DC gun was used to create quantum efficiency maps of the cathode surfaces. This was done by placing the focusing lens before the chamber to again reduce the spot size to about $100\ \mu\text{m}$ on the cathode. After recording the charge emitted for a laser shot, we would use the positioning feedthrough to move the cathode by $100\ \mu\text{m}$ to illuminate the next spot. By plotting the electron yield vs. position, a quantum efficiency map of the surface could be constructed.

The first sample tested was a 1" diameter copper photocathode originally polished by Spawr Industries to $\lambda/20$ for $10\ \mu\text{m}$ light. It had been used in the UCLA RF gun for 4 months of operation, then removed after its quantum efficiency and emittance characteristics degraded. Upon visual inspection the cathode surface showed discoloration in the form of millimeter-sized splotches, apparently from chemical contamination. There were also small pits on the surface due to laser damage.

The quantum efficiency map of this sample is shown in Fig. 4.4. The contamination and damage has produced variations in the electron yield by as much as a factor of five over millimeter length scales—roughly the size of the discolored splotches on the surface. The map for an identically polished new 1" diameter Spawr copper mirror is shown for comparison. Clearly there is no such variations over the surface of this sample. The average electron yield for the new Spawr mirror is actually lower than for the used photocathode, most likely because the smooth surface of the new mirror has no emission enhancing protrusions that exist on the damaged surface of the old cathode.

A replacement cathode was then prepared for use in the RF gun. This 1" diameter copper cathode was hand polished using $1\ \mu\text{m}$ abrasive polishing liquid,

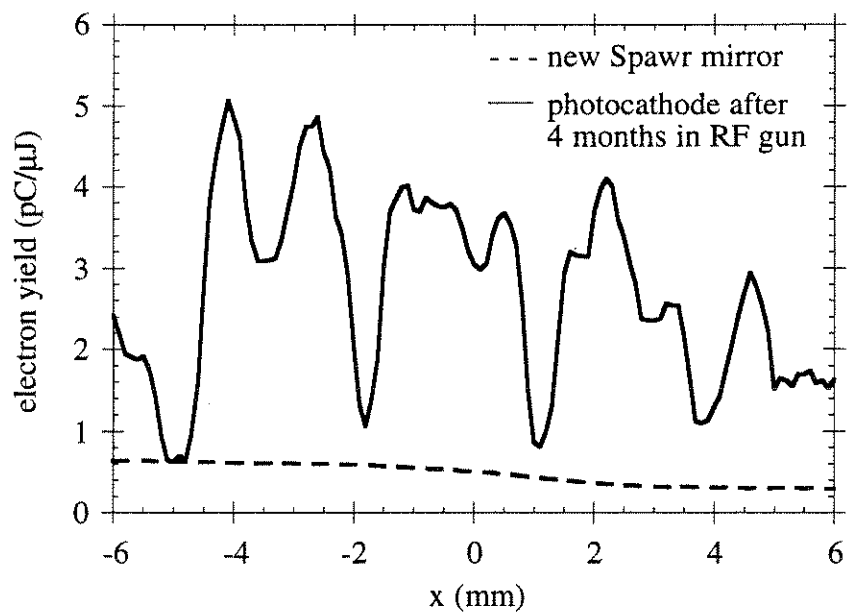


Figure 4.4: Quantum efficiency map of the Spawr polished copper photocathode after 4 months in the UCLA RF gun. A newly polished Spawr copper mirror is shown for comparison.

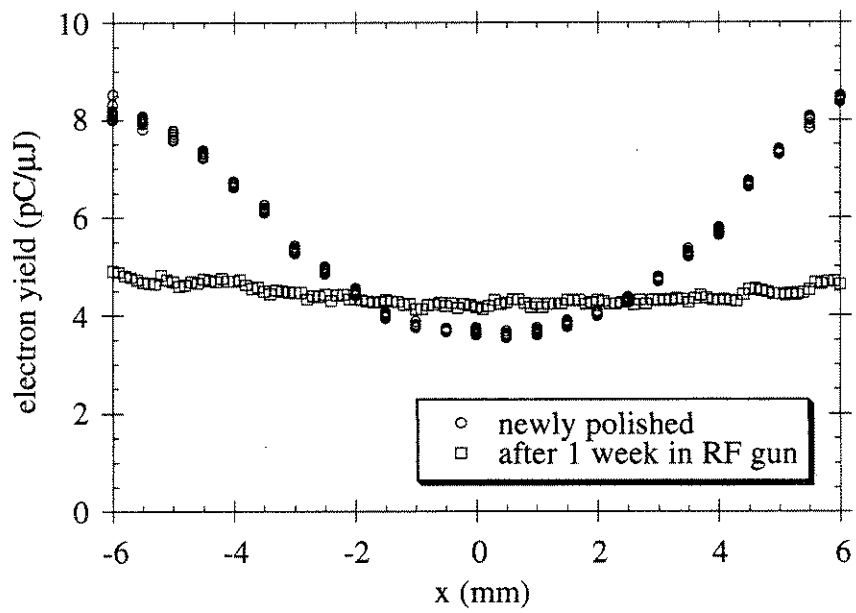


Figure 4.5: Quantum efficiency map of a hand polished copper photocathode before and after one week of use in the UCLA RF gun.

and then placed in the DC test gun for a surface characterization, which is shown in Fig. 4.5. There is a factor of two increase in electron yield toward the edges of the sample, apparently due to nonuniformities in the polishing technique. The cathode was then placed in the RF gun for one week of operation, then removed and placed back in the DC test gun for another surface mapping, also shown in Fig. 4.5. The previously enhanced emission toward the edges has been reduced to a uniform electron yield across the surface. This may be due to a smoothing of the surface near the edges caused by the stress induced by the 100 MV/m electric fields. This sample showed none of the discoloration or damage sites present on the surface of the 4 month operating cathode.

We can draw several conclusions from these photocathode studies. First, although an ablated magnesium surface exhibited a higher quantum efficiency than an ablated copper surface, the magnesium yield quickly deteriorated in a vacuum of 10^{-6} torr. Higher vacuums will then be necessary in devices which employ magnesium photocathodes. We also found that although copper demonstrated a much lower reactivity than magnesium, long term operation in the RF gun produced surface contamination and damage which degraded the quantum efficiency and emission uniformity of the copper cathode. Finally, we saw that short term exposure to the RF gun environment led to an *increase* in emission uniformity, most likely due to a smoothing of the surface by the high RF fields.

Chapter 5

Photoemission from Semiconductors

The susceptibility of metals such as copper and magnesium to contamination and damage leads us to investigate other materials for use as photocathode emitters. The ideal photocathode material should have a low reactivity, but a high quantum efficiency and high laser damage threshold. Small and large bandgap semiconductors such as silicon, diamond, and fullerene are quite nonreactive and therefore we investigated the photoemission properties of these materials to determine which may be a suitable candidate for producing laser photocathodes.

One measure of a material's suitability as a linear photoemission cathode is the product of its quantum efficiency and damage fluence $\eta\mathcal{E}_{dam}$. For example, if a laser pulse with a given spotsize produces charge Q from a copper photocathode, this same charge Q can be obtained using a material of quantum efficiency 3 times less than copper if the incident laser energy is increased by a factor of 3. Of course, this material must have a high enough damage threshold to withstand such an energy increase. Therefore, a material having $\eta\mathcal{E}_{dam}$ equal to that of copper will be able to produce the same charge as copper at the same spotsize with an appropriate increase in incident laser energy—without the risk of damage.

5.1 Band Structure of Semiconductors

The electronic structure of a semiconductor [43] is quite different from that of a metal (Fig. 5.1). In a metal, the outermost electron shell of each atom is only partially filled. When metal atoms form a lattice crystal, the electrons in this shell are not bound to individual atoms but rather are free to move throughout the metal. These are the conduction electrons which are responsible for many of the physical properties of the metal: electrical conductivity, heat capacity, reflectivity, etc. The electrons in this band approximate a free electron gas, and so the Sommerfeld model can successfully describe many of these metal properties including photoemission. The highest occupied state at $T = 0$ is located at the Fermi level, but there is a continuum of empty states that lie from the Fermi level up to above the vacuum level into which a conduction electron can be excited.

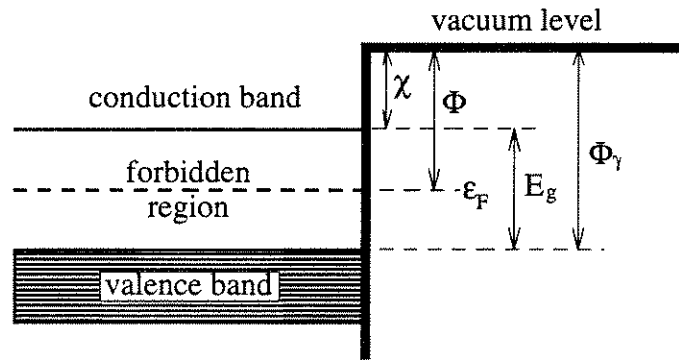


Figure 5.1: Band structure for an undoped (intrinsic) semiconductor. χ is the electron affinity, Φ is the work function, ϵ_F is the Fermi level, E_g is the band gap, and Φ_γ is the photoelectric threshold.

In a pure (intrinsic) semiconductor the electrons in the outermost shell of each atom are used to form the covalent bonds of the crystal lattice. There are no free electrons, and therefore the conduction band is empty. The outer shell

electrons form the valence band which has all of its states completely filled. There is a forbidden energy region between the valence band and the conduction band which has no available electron states (the electron wave function in the periodic potential of the lattice has no solution at these energies).

The Fermi level ϵ_F lies in the middle of the forbidden region, and the work function Φ is defined as in a metal to be the energy difference between the Fermi level and the vacuum level. In order for a semiconductor to exhibit conductivity, electrons must be excited from the valence band up to the conduction band where they are free to move. Typically, this excitation will come from the thermal energy of the electrons. The least amount of energy required to do this is the band gap energy E_g (the distance from the top of the valence band to the bottom of the conduction band). Materials with large bandgaps ($E_g > 1$ eV) are classified as insulators because very few electrons will have enough energy at normal temperatures to traverse the bandgap.

For every electron that is excited into the conduction band there is a corresponding lack of electron, or “hole” that is created in the valence band. This hole acts as a positive charge carrier and is free to move throughout the semiconductor in the valence band the same way that the electron is free to move throughout the semiconductor in the conduction band. Thus an intrinsic semiconductor will have an equal number of electrons and holes that carry charge.

The energy difference between the bottom of the conduction band and the vacuum level is the electron affinity χ . Once an electron is excited into the conduction band this is the amount of energy required to free it from the material. Semiconductors which are used as thermionic or field emitters generally have a low electron affinity.

In general, the electron population will be much higher in the valence band than in the conduction band or in any surface states which may exist. Therefore, when a semiconductor is used for photoemission the valence band will be the dominant source of electrons. The minimum photon energy required for photoemission will thus be the energy difference between the top of the valence band and the vacuum level. This is known as the photoelectric threshold Φ_γ and it is this quantity, not the work function, which characterizes the photoemission properties of a semiconductor.

5.2 N-type Doping

The addition of impurities to a semiconductor lattice can greatly change the electronic properties of the material [44]. If the impurity is an atom which gives up an electron in order to bind to the lattice and the energy levels of these electrons lie in the forbidden region close to the bottom of the conduction band, the donated electrons can enter the conduction band where they are free to move throughout the material. This is known as an n-type semiconductor, because the charge carriers are negative electrons.

If the doping level is high, there will be an additional effect called band bending (Fig. 5.2). Some impurity atoms on the surface will have their donor electrons fall into unoccupied surface states rather than into the conduction band. This will produce an excess of negative charge at the surface which will repel conduction electrons deeper into the material, exposing the fixed, positive donor sites. A depletion region is thus created near the semiconductor surface. This leads to a variation of electric potential which causes the bands to bend downward away from the surface. As a result, the electron affinity and the photoelectric threshold

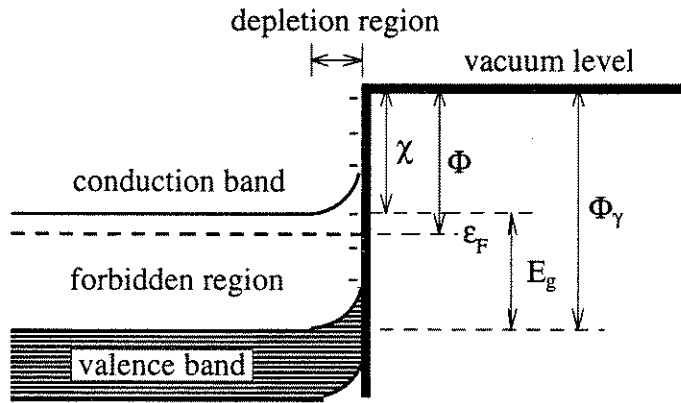


Figure 5.2: A heavily doped n-type semiconductor.

will increase for an n-type semiconductor.

5.3 P-type Doping

If the semiconductor is doped with an element that receives an electron when binding to the lattice, then these impurity atoms will become acceptor sites throughout the crystal if the acceptor energy levels lie in the forbidden region close to the top of the valence band. The acceptors will trap electrons from the valence band, thereby creating mobile holes. This is a p-type semiconductor, because the charge carriers are positive holes in the valence band.

Band bending will also occur for high p-type doping (Fig 5.3). The impurity acceptors on the surface will pull in electrons from occupied surface states, creating a net positive charge there. This will repel the positive valence band holes deeper into the material, exposing the fixed negative acceptor sites. Once again a depletion region is formed, and the variation of electric potential causes the bands to bend. Because the depletion region is now negative, the bands will

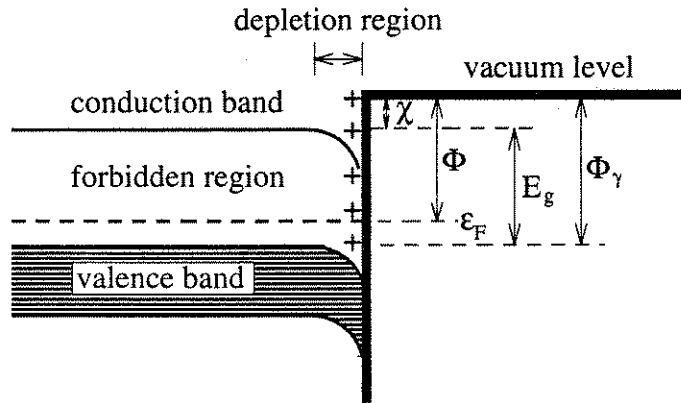


Figure 5.3: A heavily doped p-type semiconductor.

bend upward away from the surface. For a p-type semiconductor, this band bending will cause a decrease in both the electron affinity and photoelectric threshold. In fact, if the bending is strong enough it is possible for the conduction band in the bulk of the material to reach a higher energy level than the vacuum level at the surface. This is known as negative electron affinity (NEA). Electrons which are excited into the conduction band will simply fall out of the material if they are close enough to the surface. For this reason NEA materials generally make good thermionic and field emitters.

To study the emission properties of semiconductors [45], we used the short pulse laser setup described in Sec. 3.2. A special copper mount was designed having two cups, each 2 mm deep, with thin wire clamps to keep the semiconductor samples in place while maintaining electrical contact with the surface. The mount held two samples, each of which could be positioned at the usual 3 mm distance from the anode using the positioning feedthrough. Emitted charge vs. incident laser energy traces were taken at the three short pulse laser wavelengths for various semiconductor materials. The goal was to find a material having an

electron yield comparable to that found earlier for copper, while having a higher laser damage threshold.

5.4 Silicon

Pure silicon has a bandgap of 1.1 eV [43] and a photoelectric threshold of 5.2 eV [44]. Thus we expect to observe 1-photon emission with the 217 nm pulses, 2-photon emission with the 325 nm pulses, and 3-photon emission with the 650 nm pulses. The resistivity of pure silicon is extremely high, $\sim 10^{12} \Omega\cdot\text{cm}$ [35]. Doped silicon, however, can have resistivities many orders of magnitude lower than this, and for high doping may have different photoemission thresholds due to the band bending effects described earlier.

For this experiment we measured the photoemission from phosphorous-doped n-type silicon and boron-doped p-type silicon. The samples were single crystal (100) squares measuring $5 \text{ mm} \times 5 \text{ mm} \times 1 \text{ mm}$ thick. For the n-type sample, the phosphorous doping was 10^{16} cm^{-3} giving a resistivity of $\rho = 0.5 \Omega\cdot\text{cm}$. For the p-type sample, the boron doping was 10^{15} cm^{-3} which gave a resistivity of $\rho = 20 \Omega\cdot\text{cm}$.

The results are shown in Fig. 5.4. As expected, the 217 nm and 325 nm traces yield slopes 1 and 2 respectively. The slopes of the 650 nm traces are $\sim 20\%$ too high which indicates that at such low multiphoton yields, emission of electrons not in the valence band (conduction electrons, electrons in surface states, etc.) may be contributing to the measured charge. For the n-type silicon sample the b_n coefficients are

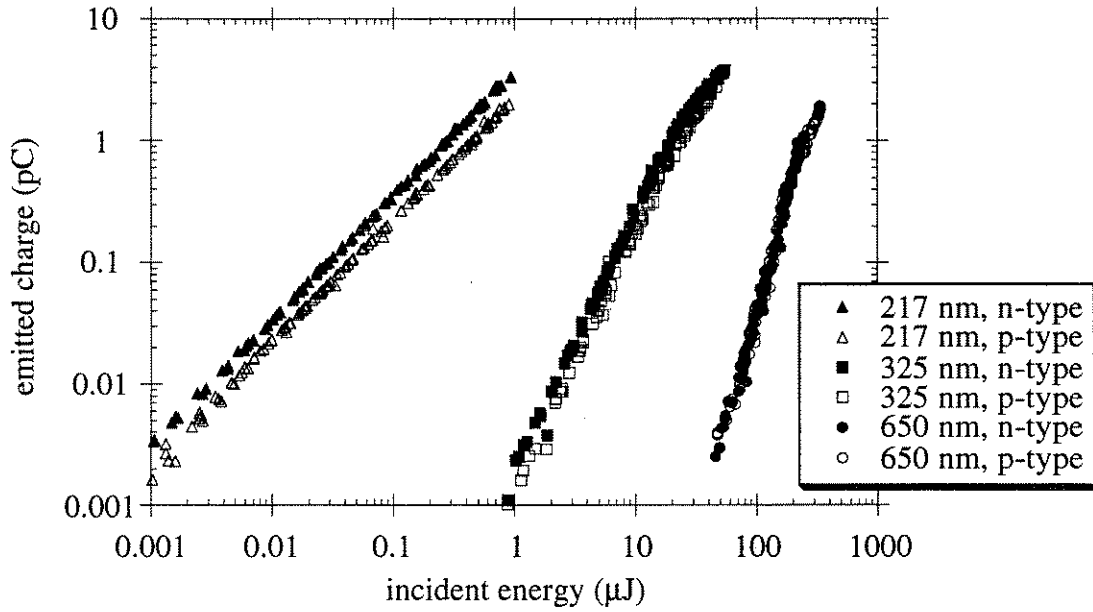


Figure 5.4: Emitted charge vs. incident energy for n- and p-type silicon.

$$217 \text{ nm: } b_1 = 3.7 \text{ pC}/\mu\text{J}$$

$$325 \text{ nm: } b_2 = 1.5 \times 10^{-3} \text{ pC}/\mu\text{J}^2$$

$$650 \text{ nm: } b_3 = 6.9 \times 10^{-8} \text{ pC}/\mu\text{J}^3$$

and for the p-type sample we have

$$217 \text{ nm: } b_1 = 2.3 \text{ pC}/\mu\text{J}$$

$$325 \text{ nm: } b_2 = 1.5 \times 10^{-3} \text{ pC}/\mu\text{J}^2$$

$$650 \text{ nm: } b_3 = 5.0 \times 10^{-8} \text{ pC}/\mu\text{J}^3$$

Note that the yields for both samples are comparable, which suggests that the band bending for these doping levels is not significant.

Comparing these values to the b_n coefficients of copper obtained in Sec. 3.3.2 we see that for silicon b_1 is less than 2% of the value for copper, b_2 is 0.8% that of

copper, and b_3 is 0.5% of the copper value. Therefore, even highly doped silicon emits significantly less electrons at each wavelength than does copper.

5.5 Diamond

Diamond has some extreme characteristics favorable for photocathode durability. It is the hardest of all materials and has a surface that is very nonreactive. Thus diamond should be resistant to laser damage and surface contamination. Diamond has a large bandgap ($E_g = 5.5$ eV) [46] and therefore is a high resistivity insulator ($\rho = 10^{16}$ $\Omega\cdot\text{cm}$ [35]). Its conduction band lies at the vacuum level and thus the photoelectric threshold is equal to the bandgap energy ($\Phi_\gamma = 5.5$ eV). The presence of hydrogen on the (111) surface of natural diamond can shift the energy bands such that the diamond exhibits NEA [47]. This type of diamond has been used as a thermionic emitter and as a cold field-emitting cathode.

Because of the large photoelectric threshold, pure crystalline diamond may demonstrate a low quantum yield. Thus we wished to investigate other forms and dopings of diamond which may show significant electron emission. In this experiment we measured the photoemission yields of three types of diamond: pure diamond film, doped diamond film, and pure single crystal diamond.

5.5.1 Pure Diamond Film

The photoemission results for two different types of pure diamond film are shown in Fig. 5.5. Both films were deposited by plasma enhanced chemical transport (PECT) on silicon substrates [48]. The cauliflower diamond film was 1 μm thick and had a surface roughness of 40 \AA , while the well-oriented diamond film had

a thickness of $5.5 \mu\text{m}$ and a surface roughness of 4 \AA . X-ray diffraction measurements showed that the crystal faces on the surfaces of both films were predominantly (111). Because the samples were small ($4 \text{ mm} \times 4 \text{ mm}$ squares), we placed a focusing lens in the laser line which reduced the spotsize by a factor of six. This assured that the entire laser spot was contained within the sample boundaries. The laser energy values were scaled at each wavelength to account for the increased intensity so that the b_n values could be properly compared to those of copper and silicon obtained earlier with the larger spotsizes. Space charge effects now occur at lower charge values due to the smaller spotsize of the laser.

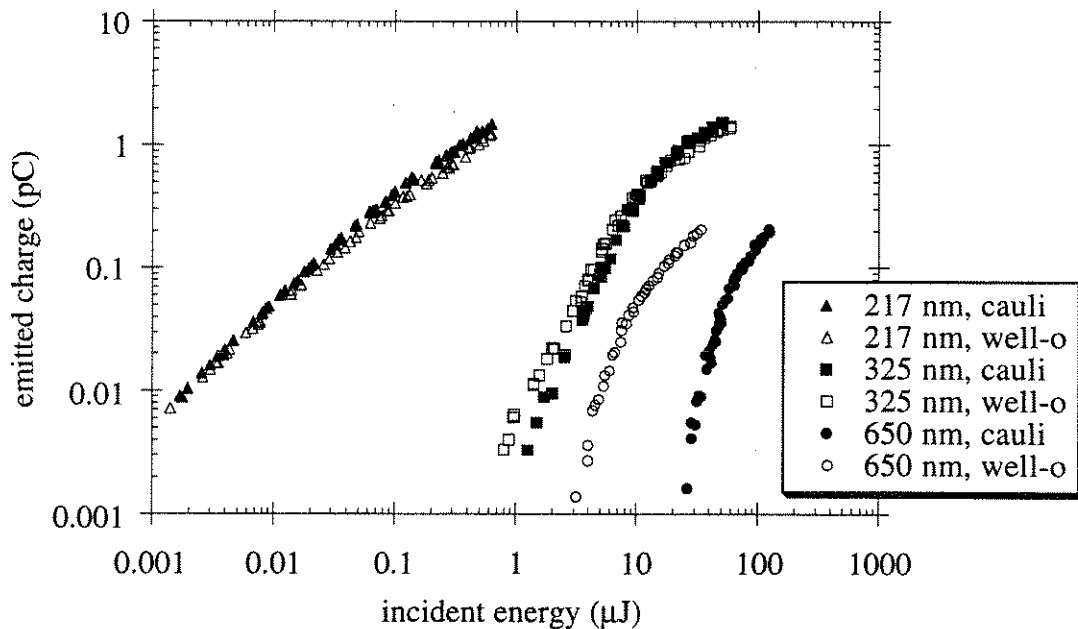


Figure 5.5: Emitted charge vs. incident energy for cauliflower and well-oriented pure diamond films.

With a 5.5 eV photoelectric threshold we once again expect emission curves of slopes 1, 2, and 3 for the 217, 325, and 650 nm wavelengths, respectively. Below

the space charge bending these slopes are correct except for the cauliflower film at 650 nm which has a slope $\sim 30\%$ too high. Again, this may be due to emission contributions from non-valence band electrons becoming apparent at the low 3-photon emission levels. The b_n coefficients of the cauliflower diamond film are

$$\begin{aligned} 217 \text{ nm: } & b_1 = 5.1 \text{ pC}/\mu\text{J} \\ 325 \text{ nm: } & b_2 = 3.6 \times 10^{-3} \text{ pC}/\mu\text{J}^2 \\ 650 \text{ nm: } & b_3 = 3.1 \times 10^{-7} \text{ pC}/\mu\text{J}^3 \end{aligned}$$

The coefficients for the well-oriented sample are

$$\begin{aligned} 217 \text{ nm: } & b_1 = 4.3 \text{ pC}/\mu\text{J} \\ 325 \text{ nm: } & b_2 = 5.1 \times 10^{-3} \text{ pC}/\mu\text{J}^2 \\ 650 \text{ nm: } & b_3 = 6.9 \times 10^{-5} \text{ pC}/\mu\text{J}^3 \end{aligned}$$

The b_n coefficients are small compared to those of copper except for the b_3 value of the well-oriented film at 650 nm. This value is nearly 5 times *greater* than the corresponding b_3 copper value.

5.5.2 Doped Diamond Film

Sodium-doped and boron-doped diamond films were also produced using the PECT deposition technique on silicon substrates. The films had a well-oriented crystal structure that was predominantly (111). Both films were determined to be p-type by observing polarity in hot probe and rectify junction measurements. The concentration of the boron-doped film was $8 \times 10^{19} \text{ cm}^{-3}$; the concentration of the sodium-doped film was not measured. The resistivity of the sodium-doped film was $\rho = 2.2 \times 10^3 \text{ }\Omega\cdot\text{cm}$, while the resistivity of the boron-doped film was 5 orders of magnitude lower, $\rho = 4.3 \times 10^{-2} \text{ }\Omega\cdot\text{cm}$.

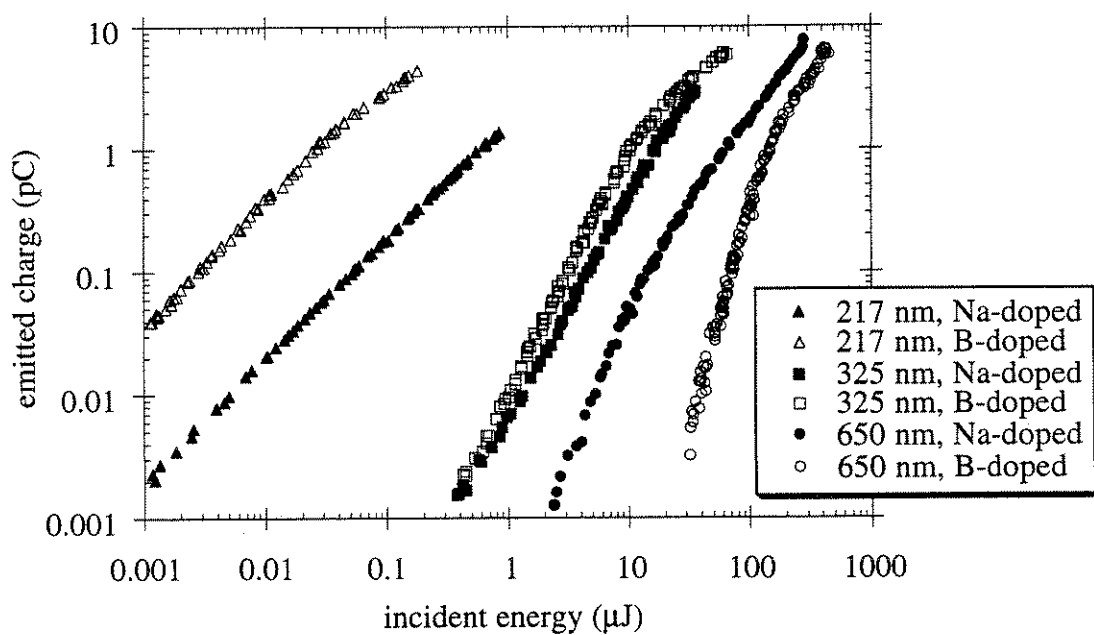


Figure 5.6: Emitted charge vs. incident energy for sodium-doped and boron-doped diamond films.

The photoemission curves for these two films are shown in Fig. 5.6. The curves at 217 nm and 325 nm have the expected slopes of 1 and 2 for both samples. The slopes at 650 nm are 20% too low for the sodium-doped film and 20% too high for the boron-doped film from the expected slope 3 (measured as always below space charge bending). Note that the emission at 650 nm is much higher for the sodium-doped sample, while the 217 nm emission is much higher for the boron-doped sample. For the sodium-doped diamond film, the b_n coefficients are

$$\begin{aligned} 217 \text{ nm: } & b_1 = 1.7 \text{ pC}/\mu\text{J} \\ 325 \text{ nm: } & b_2 = 3.7 \times 10^{-3} \text{ pC}/\mu\text{J}^2 \\ 650 \text{ nm: } & b_3 = 4.5 \times 10^{-5} \text{ pC}/\mu\text{J}^3 \end{aligned}$$

while the b_n coefficients for the boron-doped film are

$$\begin{aligned} 217 \text{ nm: } & b_1 = 38 \text{ pC}/\mu\text{J} \\ 325 \text{ nm: } & b_2 = 9.7 \times 10^{-3} \text{ pC}/\mu\text{J}^2 \\ 650 \text{ nm: } & b_3 = 2.4 \times 10^{-7} \text{ pC}/\mu\text{J}^3 \end{aligned}$$

The 217 nm emission from the boron-doped diamond film is quite significant, $\sim 20\%$ of the emission from copper. The 650 nm emission from the sodium-doped film is also significant, a factor of 3 greater than copper.

5.5.3 Single-Crystal Bulk Diamond

The last of the diamond samples tested in this experiment were (110) and (111) single-crystal natural bulk diamond. The (110) face sample measured 4 mm \times 4 mm \times 0.25 mm thick, and the (111) face sample was 3 mm \times 3 mm \times 0.25 mm thick. Because of the small sample sizes we had to reduce the laser spotsize (again by a factor of six) in order to assure that the laser spot was completely on the

sample surfaces. As before, the laser energy values were scaled to the larger spotsizes for proper b_n comparisons with previous results.

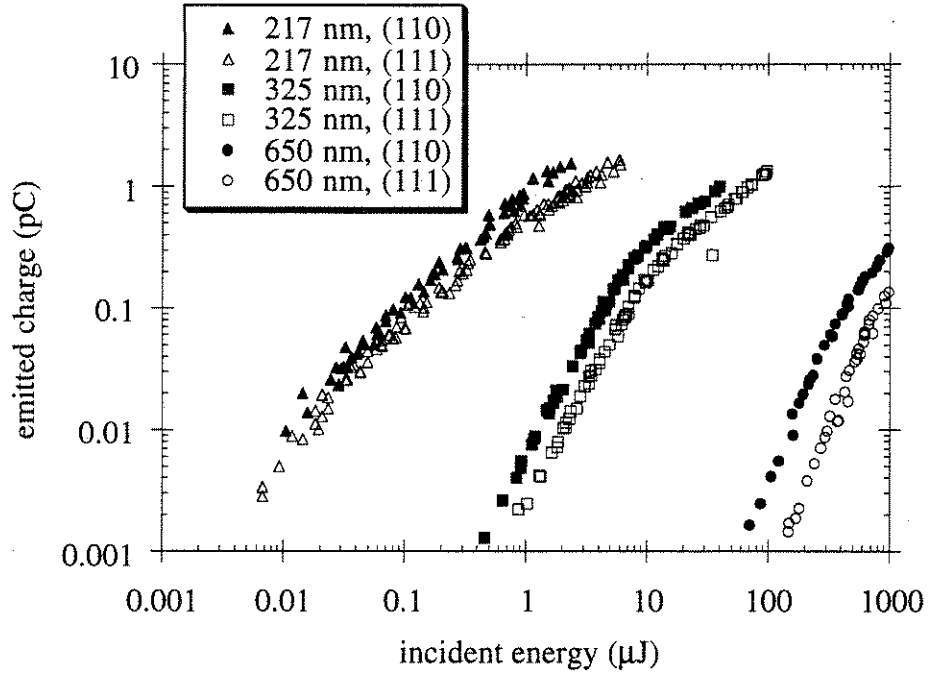


Figure 5.7: Emitted charge vs. incident energy for (110) and (111) single-crystal bulk diamond.

We first measured the reflection and transmission coefficients of the (110) sample for our three laser wavelengths. The results were

$$217 \text{ nm: } R = 0.23, T = 0.002$$

$$325 \text{ nm: } R = 0.23, T = 0.79$$

$$650 \text{ nm: } R = 0.27, T = 0.72$$

with an error of ± 0.05 for each quantity. Thus we see that natural diamond exhibits a low absorption for $\lambda = 650$ and 325 nm, but a strong absorption at 217 nm. This is expected because photon energies at 650 and 325 nm (1.9 and

3.8 eV respectively) are much less than the diamond bandgap and therefore single photons of these wavelengths cannot interact with the valence electrons. The 217 nm photons, however, have an energy of 5.7 eV which is slightly larger than the 5.5 eV diamond bandgap. These photons can then excite valence electrons into the conduction band and as a result are strongly absorbed by the material.

The photoemission curves for the bulk diamond samples are shown in Fig. 5.7. The 217 and 325 nm curves demonstrate slopes 1 and 2 for both samples, while the 650 nm curves are each $\sim 15\%$ less than a slope 3. The b_n coefficients for the (110) diamond sample are

$$\begin{aligned} 217 \text{ nm: } & b_1 = 0.90 \text{ pC}/\mu\text{J} \\ 325 \text{ nm: } & b_2 = 5.1 \times 10^{-3} \text{ pC}/\mu\text{J}^2 \\ 650 \text{ nm: } & b_3 = 2.4 \times 10^{-9} \text{ pC}/\mu\text{J}^3 \end{aligned}$$

while the (111) sample coefficients are

$$\begin{aligned} 217 \text{ nm: } & b_1 = 0.53 \text{ pC}/\mu\text{J} \\ 325 \text{ nm: } & b_2 = 2.1 \times 10^{-3} \text{ pC}/\mu\text{J}^2 \\ 650 \text{ nm: } & b_3 = 2.6 \times 10^{-10} \text{ pC}/\mu\text{J}^3 \end{aligned}$$

We see that the (110) sample shows higher emission than the (111) sample, but the overall emission of each bulk natural diamond sample is much less than copper at all wavelengths.

5.6 Fullerene Films

The final material tested in our photoemission experiment was fullerene. Fullerene exists primarily as the soccer ball shaped molecule C_{60} but also includes C_{70} , C_{84} ,

and higher numbered ellipsoidal carbon molecules. Pure C_{60} has a resistivity of $\rho = 10^5 \Omega \cdot \text{cm}$ [49] and a bandgap of $E_g = 1.9 \text{ eV}$ [50]. The photoelectric threshold of fullerene has been measured to be $\Phi_\gamma = 7.6 \text{ eV}$ [32]. For this value of Φ_γ we expect the charge vs. energy curves to yield a slope 2 for the 217 nm laser pulses, slope 2 for the 325 nm pulses, and slope 4 for the 650 nm pulses.

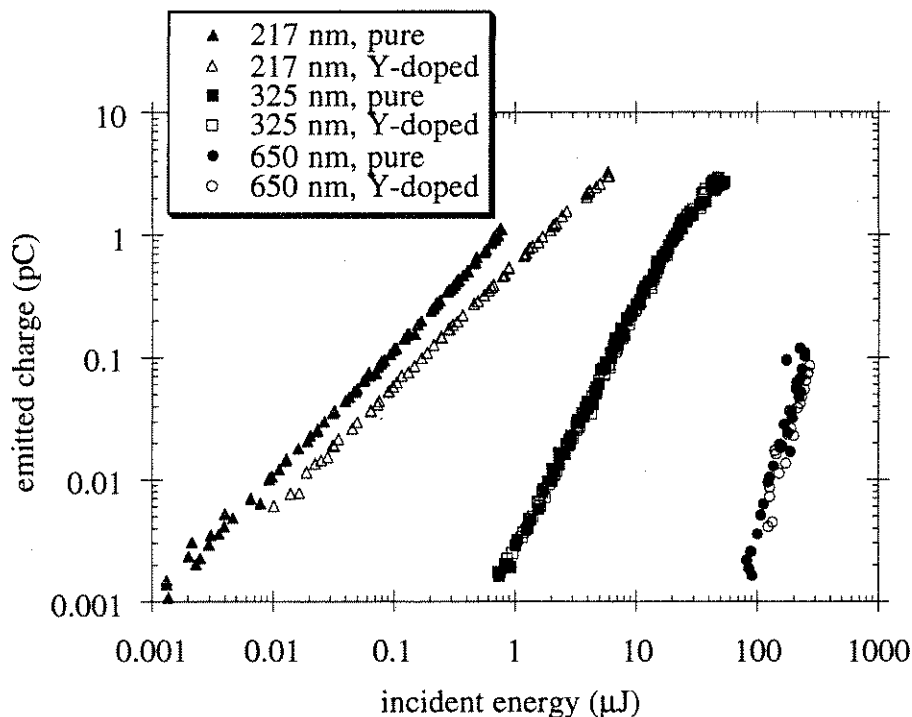


Figure 5.8: Emitted charge vs. incident energy for pure and yttrium-doped fullerene films.

The thin fullerene films used in this experiment were produced by evaporating a powder containing 95% C_{60} and 5% C_{70} and higher. The films were deposited on silicon substrates and were $\sim 5000 \text{ \AA}$ in thickness. Two types of fullerene film were tested—pure fullerene and yttrium-doped fullerene.

The results are shown in Fig. 5.8. The 217 nm and 325 nm curves give slopes 1

and 2, respectively. The 650 nm curves were 10–20% higher than a slope 3. Thus the 217 nm and 650 nm slopes are inconsistent with the values of Φ_γ measured in the above references. The b_n coefficients for pure fullerene are

$$\begin{aligned} 217 \text{ nm: } b_1 &= 1.2 \text{ pC}/\mu\text{J} \\ 325 \text{ nm: } b_2 &= 2.8 \times 10^{-3} \text{ pC}/\mu\text{J}^2 \\ 650 \text{ nm: } b_3 &= 5.4 \times 10^{-9} \text{ pC}/\mu\text{J}^3 \end{aligned}$$

and the yttrium-doped fullerene coefficients are

$$\begin{aligned} 217 \text{ nm: } b_1 &= 0.54 \text{ pC}/\mu\text{J} \\ 325 \text{ nm: } b_2 &= 2.3 \times 10^{-3} \text{ pC}/\mu\text{J}^2 \\ 650 \text{ nm: } b_3 &= 4.2 \times 10^{-9} \text{ pC}/\mu\text{J}^3 \end{aligned}$$

The b_n coefficients for the two samples at all wavelengths are much lower than the corresponding b_n coefficients for copper.

5.7 Summary of Electron Yields

Fig. 5.9 is a comparison of the b_1 coefficients for all the materials at 217 nm wavelength. Most photoemission applications use modest incident laser intensities and therefore require single-photon emission to achieve the desired electron yield. Thus the b_1 coefficients are the most relevant in evaluating the feasibility of a material for use as a photoemitter.

All of the materials had b_n coefficients significantly lower than copper with the exception of the boron-doped diamond film. The yield from boron-doped diamond was nearly 20% of the electron yield from copper. Using Eq. 3.17 we can calculate the quantum efficiency of boron-doped diamond at 217 nm from its b_1 coefficient:

$$\eta_{217} = 2.2 \times 10^{-4} \text{ electrons/photon}$$

The relatively high single-photon electron yield of boron-doped diamond makes it the best photocathode candidate of the materials tested in this experiment.

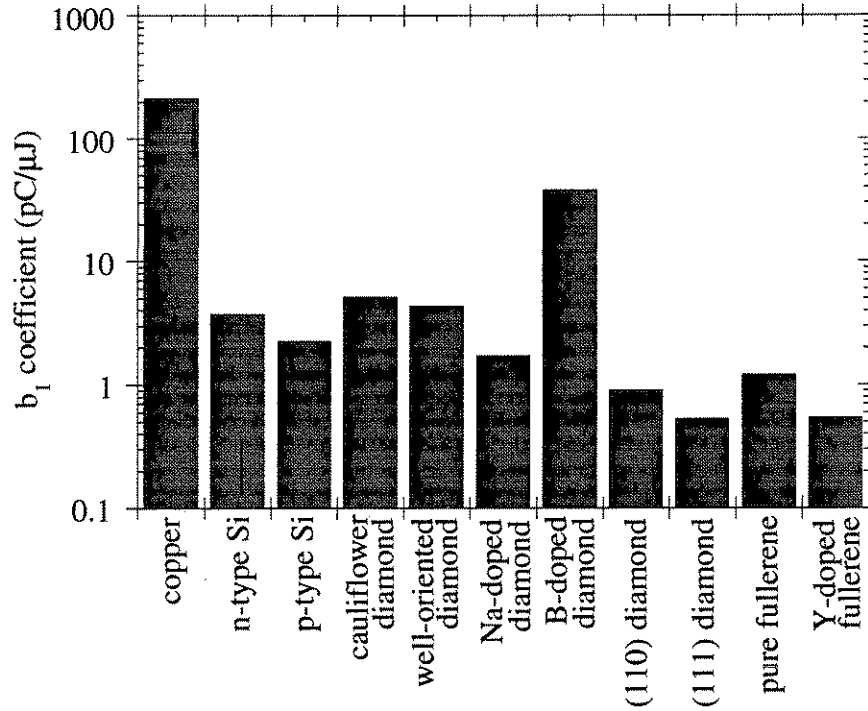


Figure 5.9: The b_1 coefficients for various materials at 217 nm incident wavelength.

The b_2 coefficients for 2-photon emission at 325 nm are shown in Fig. 5.10. All of the semiconductor materials had coefficients of the same order of magnitude. Once again, the boron-doped diamond film exhibited the highest yield; however, its b_2 coefficient was only 5% of the value for copper.

Fig. 5.11 shows the b_3 coefficients for 3-photon emission at 650 nm. These coefficients varied by over 5 orders of magnitude for the different semiconductor materials. As mentioned earlier, both the well-oriented diamond film and the

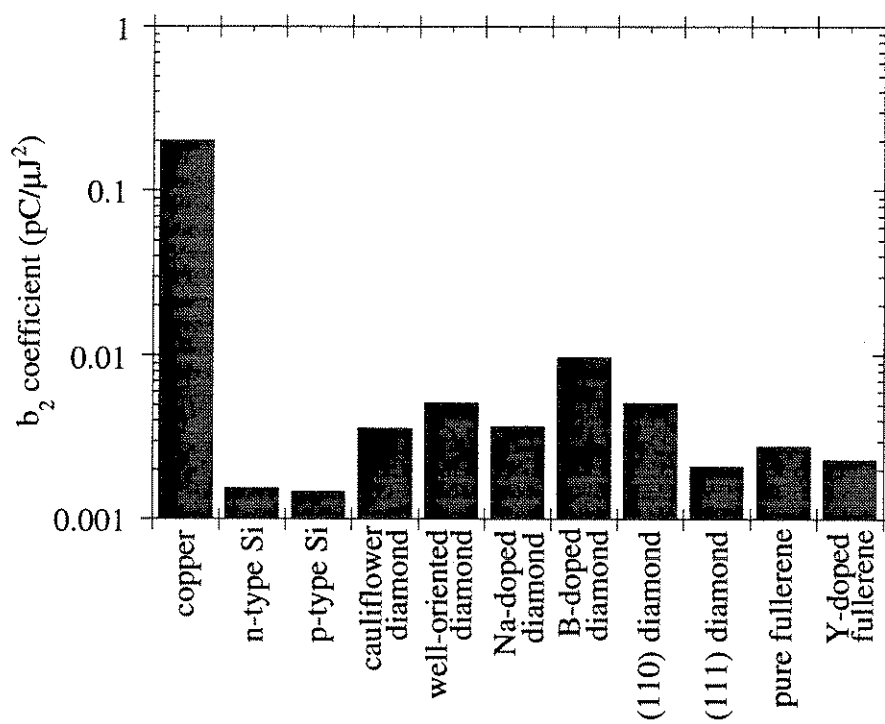


Figure 5.10: The b_2 coefficients for various materials at 325 nm incident wavelength.

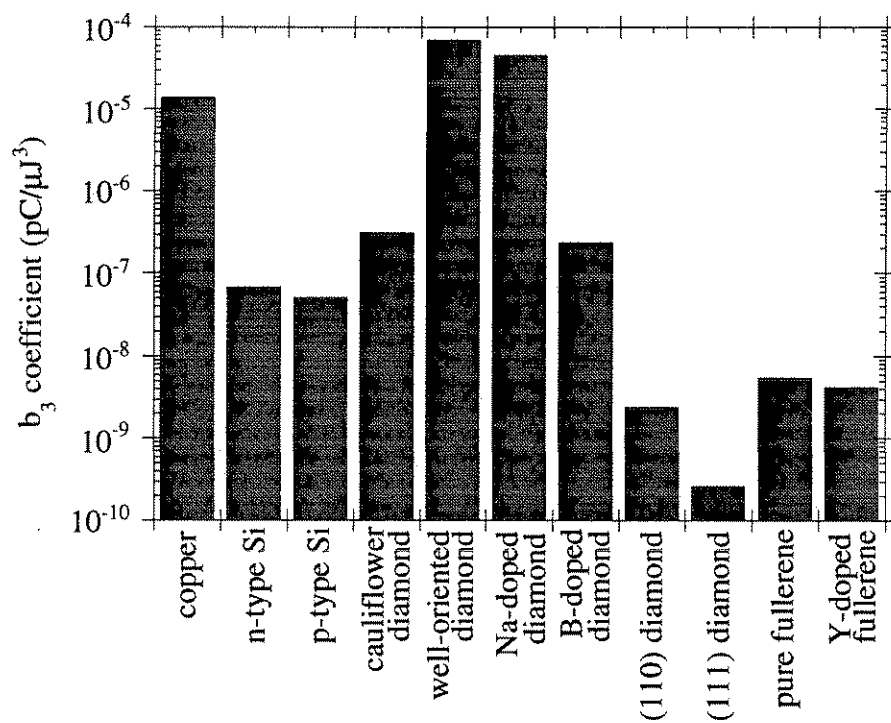


Figure 5.11: The b_3 coefficients for various materials at 650 nm incident wavelength.

sodium-doped diamond film had b_3 coefficients greater than copper. However, the 10–20% variation from a slope 3 for these samples suggests that there may be charge contributions from processes other than the 3-photon emission from valence band electrons (e.g., lower order photoemission from surface state electrons or contaminants). In any case the electron yields at 650 nm for all the materials are small for laser energies below 50 μJ (peak intensities below 1 GW/cm^2). The requirement of such high incident intensities to attain significant yields makes 3-photon emission impractical for photocathode applications unless an extremely short-pulse laser system can be utilized to achieve very high intensities without damaging the photoemitter.

5.8 Damage Threshold Measurements

As mentioned earlier, the boron-doped diamond sample showed the most promise as a photocathode emitter because of its high single-photon electron yield. From the discussion at the beginning of this chapter, however, a photocathode must also have a high damage threshold to withstand the repeated barrage of incident laser pulses during its use. Thus we performed laser damage measurements on the boron-doped diamond film and compared them to damage measurements made on copper. Of course, the damage threshold for a thin film is not only dependent on its material, but is also strongly dependent on the film quality and the adhesion properties of the film on the substrate. The damage thresholds of high quality polished chemical vapor deposited (CVD) diamond films have been measured to be only 15–20% lower than those of single crystal bulk diamond [51]. A boron-doped bulk diamond crystal would avoid all of these film-related weaknesses and therefore may constitute a better photocathode material if the

doping level can be made high enough to produce a significant electron yield. To predict the damage threshold of such a sample (or that of a high quality diamond film) we used our (110) bulk diamond under the assumption that boron doping does not significantly alter the damage resistance of a diamond crystal.

For short laser pulses, damage occurs when the laser fluence \mathcal{E} (energy per area) is great enough to create a plasma from the lattice ions on the surface. This is known as surface ablation [52]. A focusing lens was placed in the laser line to reduce the spotsize and therefore increase the laser fluence at the surface. The damage threshold measurements were performed at 650 nm with a spotsize of $w_0 = 400 \mu\text{m}$.

To measure the damage characteristics of copper, boron-doped diamond film, and (110) bulk diamond the bias of the hollow anode collector was changed to -2 kV. With this polarity the electron emission should be suppressed and thus no charge collected when the incident laser fluence is below the damage threshold of the cathode material. As the laser energy is increased there should be a sudden onset of a positive signal from the preamplifier when the laser begins to ablate the surface. This signal is produced as the ions from the laser ablation plasma are collected by the negatively biased anode leaving an excess of electrons on the photocathode which then travel through the $1 \text{ M}\Omega$ load resistor to ground. We define the material damage threshold as the laser fluence corresponding to the onset of this positive signal.

The damage threshold measurements for these three materials at 650 nm are shown in Fig. 5.12. The minimum charge measurable by the preamplifier is 0.001 pC —thus any charge below this value is taken to be zero. For all three materials there is no ion charge at low laser energies. As the incident energy is

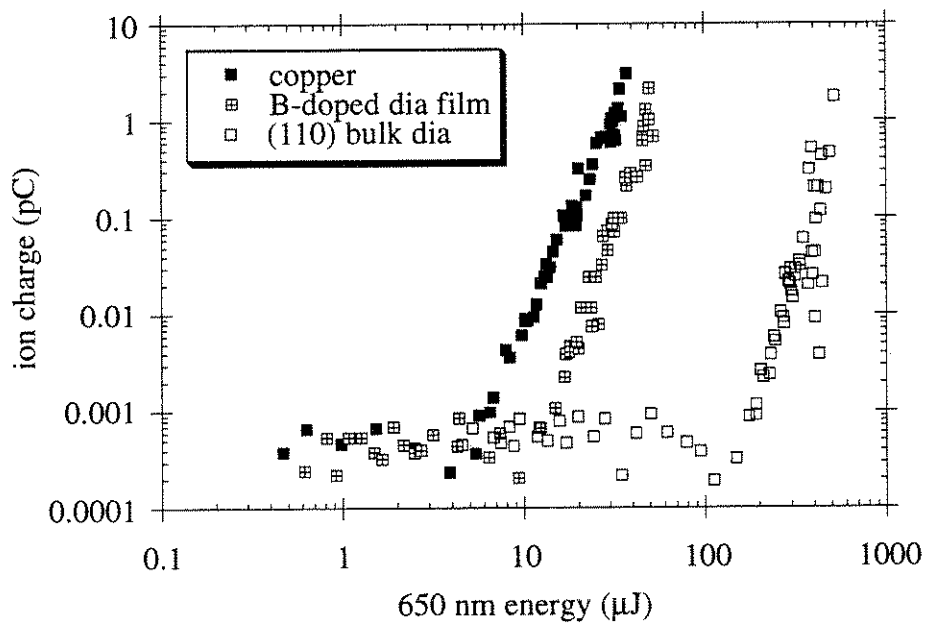


Figure 5.12: Emitted ion charge vs. incident 650 nm laser energy for copper, boron-doped diamond film, and (110) bulk diamond. The onset of laser damage occurs at energies of $8 \mu\text{J}$, $17 \mu\text{J}$, and $200 \mu\text{J}$, respectively. The corresponding damage fluences are $6 \text{ mJ}/\text{cm}^2$ for copper, $14 \text{ mJ}/\text{cm}^2$ for boron-doped diamond film, and $160 \text{ mJ}/\text{cm}^2$ for (110) bulk diamond.

increased we see an onset of ion emission at $8 \mu\text{J}$, $17 \mu\text{J}$, and $200 \mu\text{J}$ for copper, boron-doped diamond film, and (110) bulk diamond, respectively. The slope of each ion emission curve after the onset is very large (> 5) and therefore we assume that the onset of ion emission indicates the beginning of laser damage. The damage fluences corresponding to these energies are

$$\begin{aligned} \text{copper: } \mathcal{E}_{dam} &= 6 \text{ mJ/cm}^2 \\ \text{boron-doped diamond film: } \mathcal{E}_{dam} &= 14 \text{ mJ/cm}^2 \\ \text{(110) bulk diamond: } \mathcal{E}_{dam} &= 160 \text{ mJ/cm}^2 \end{aligned}$$

Thus the damage threshold of the boron-doped diamond film at 650 nm is over twice the threshold of copper, and the threshold of (110) bulk diamond is over 25 times that of copper. All samples showed visible damage spots upon inspection after the experiment.

Damage threshold measurements were also performed at 325 nm and 217 nm, but these results were inconclusive. The 325 nm results are shown in Fig. 5.13. At this wavelength, the onset of ion emission was nearly the same for all three samples. This suggests that the higher energy 325 nm photons may be dislodging contaminants on the sample surfaces and therefore the ion emission is independent of the cathode material. In addition, the ion emission curve for the (110) bulk diamond sample after the onset was a slope 2 which indicates a 2-photon effect. This is inconsistent with laser ablation which is not a simple 2-photon process, and may indicate that contaminant ions on this sample are being ejected by 2-photon absorption of the 325 nm laser pulses.

The ion emission curves at 217 nm are shown in Fig. 5.14. For copper and boron-doped diamond film, ion emission is present at all laser energies. The curves for these two samples are slope 1 before bending due to space charge

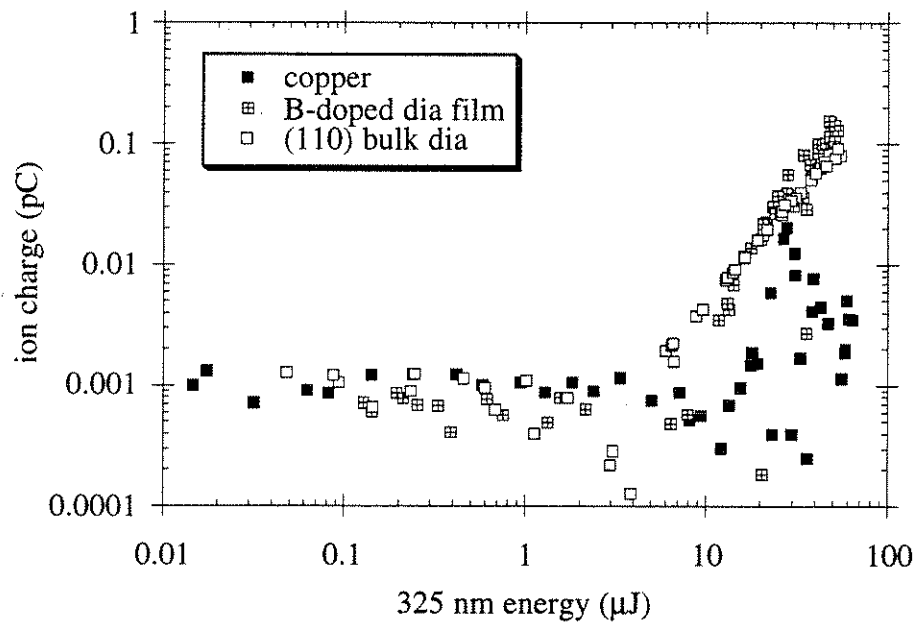


Figure 5.13: Emitted ion charge vs. incident 325 nm laser energy for copper, boron-doped diamond film, and (110) bulk diamond. The onset of ion emission is nearly the same for all three samples, suggesting that the source of the ions may be surface contaminants.

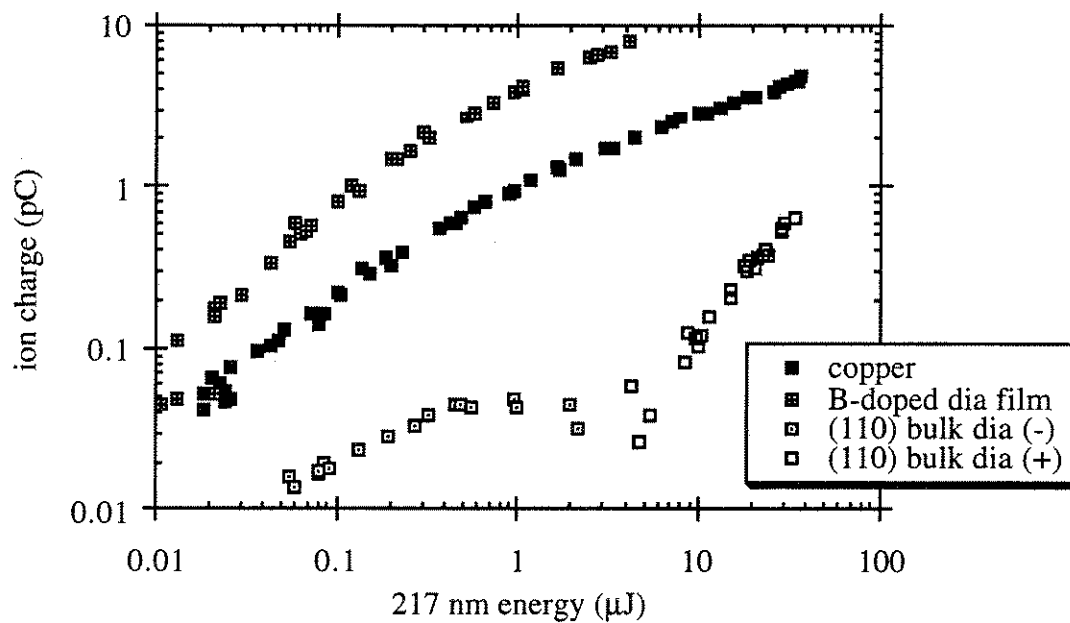


Figure 5.14: Emitted ion charge vs. incident 217 nm laser energy for copper, boron-doped diamond film, and (110) bulk diamond. For copper and boron-doped diamond there is no threshold but rather a continuous emission of ions at all laser energies. For (110) bulk diamond, the emitted charge is initially *negative* (as indicated by the dotted squares), then drops to zero and changes polarity at $E_{217} = 3 \mu\text{J}$. Above this energy the emitted charge is positive.

saturation. Again the source of ions is most likely contaminants being knocked off the surfaces by single 217 nm photons, because at low energies the laser pulse is not capable of ablating the material surface—yet ion emission is observed.

The (110) bulk diamond exhibits very strange behavior at 217 nm. For laser energies below 3 μJ the emitted charge was *negative*. This indicates that electrons are being emitted from the sample despite the anode bias of -2 kV. Because the photoelectrons escape the diamond surface barrier with an excess energy of less than 1 eV, they could not possibly overcome the 2 kV potential and be collected by the anode. The only other possibility is that some electrons are escaping from the sample to the vacuum chamber walls. As the incident laser energy is increased to 3 μJ the magnitude of the negative emitted charge decreases to zero and then changes polarity, demonstrating an increasing *positive* emitted charge for higher laser energies. Apparently at these energies the ion emission predominates over the electron emission, resulting in a net positive emitted charge.

From the results of this chapter we can calculate the product of the quantum efficiency and damage fluence for copper and boron-doped diamond film:

$$\text{copper: } \eta\mathcal{E}_{dam} = 7.2 \times 10^{-3} \text{ mJ/cm}^2$$

$$\text{boron-doped diamond film: } \eta\mathcal{E}_{dam} = 3.1 \times 10^{-3} \text{ mJ/cm}^2$$

We can obtain an estimate of $\eta\mathcal{E}_{dam}$ for a boron-doped bulk diamond sample (or a high quality boron-doped diamond film) by taking the product of the boron-doped diamond film quantum efficiency and the (110) bulk diamond damage fluence:

$$\text{boron-doped bulk diamond: } \eta\mathcal{E}_{dam} = 3.5 \times 10^{-2} \text{ mJ/cm}^2$$

Because the $\eta\mathcal{E}_{dam}$ of our boron-doped diamond film is comparable to that of copper and the estimated $\eta\mathcal{E}_{dam}$ of boron-doped bulk diamond is greater than

copper, we conclude that boron-doped diamond may be a suitable non-reactive replacement for a copper photocathode. However, the photoelectric threshold of diamond ($e\Phi_\gamma = 5.5$ eV) is higher than the work function of copper ($e\Phi = 4.6$ eV) and therefore a shorter wavelength laser ($\lambda < 226$ nm) will be required to obtain linear photoemission. Other issues such as surface quality, graphite inclusions, and film/substrate interface defects also need to be addressed.

Chapter 6

Thin Film Photoemission Experiment

Until now we have investigated photoemission simply in terms of amount of emitted charge vs. amount of incident laser energy. There has been no discussion of the dynamics of the photoemission process. One issue concerning the electron dynamics is the initial location of the photoelectrons within the material. Do the photoelectrons originate at the surface, or is the emission dominated by electrons inside the bulk of the material? In this chapter we will attempt to resolve this issue and make quantitative measurements on the maximum escape depth of photoelectrons by observing photoemission from thin copper films. We can then use these measurements to estimate the promptness of the photoemission process—an issue which may be important in the production of subpicosecond electron bunches using ultrashort laser pulses.

6.1 Photoelectron Dynamics

As described in Sec. 2.5 the standard model of volume photoemission consists of a three step process: the electron absorbs a photons which elevates it to an excited energy state, travels to the surface, and then crosses the surface barrier to

escape the material. The total emitted charge will thus depend on the depth into which the incident light can penetrate and the depth from which a photoexcited electron can reach the surface before losing its escape energy.

For optically excited electrons in metals, the primary mechanism for energy loss will be inelastic collisions with the conduction band electrons [53]. A single such collision will on average result in a significant loss of energy for the excited electron because the conduction electrons have much lower energy. After the collision the electron most likely will no longer have sufficient energy to overcome the surface barrier and will not be emitted ($nh\nu - e\Phi < e\Phi$ for all wavelengths in this experiment). Thus the maximum electron escape depth is dependent on the range l that the photoexcited electrons can travel before suffering a collision.

In general, electrons may also suffer elastic collisions with lattice phonons and may lose energy through plasmon excitation. However, for visible photon excitation energies the electron-phonon mean free path is much larger than the electron-electron mean free path. Therefore, electron-phonon collisions can be ignored. Also, the photon energies are too small to create photoelectrons capable of exciting plasma waves ($\hbar\omega_p \approx 11$ eV for copper)—this effect can be ignored as well. The electron range l will then be equal to the electron-electron mean free path, and any electrons which are emitted will have traveled ballistically to the surface.

At visible wavelengths, l is a decreasing function of the excitation energy [38]. This can be explained in terms of the Pauli exclusion principle for the conduction electrons. A photoelectron that has been excited to an energy ε above the Fermi energy ϵ_F can only interact with those conduction electrons having energy between ϵ_F and $\epsilon_F - \varepsilon$. Conduction electrons below this energy

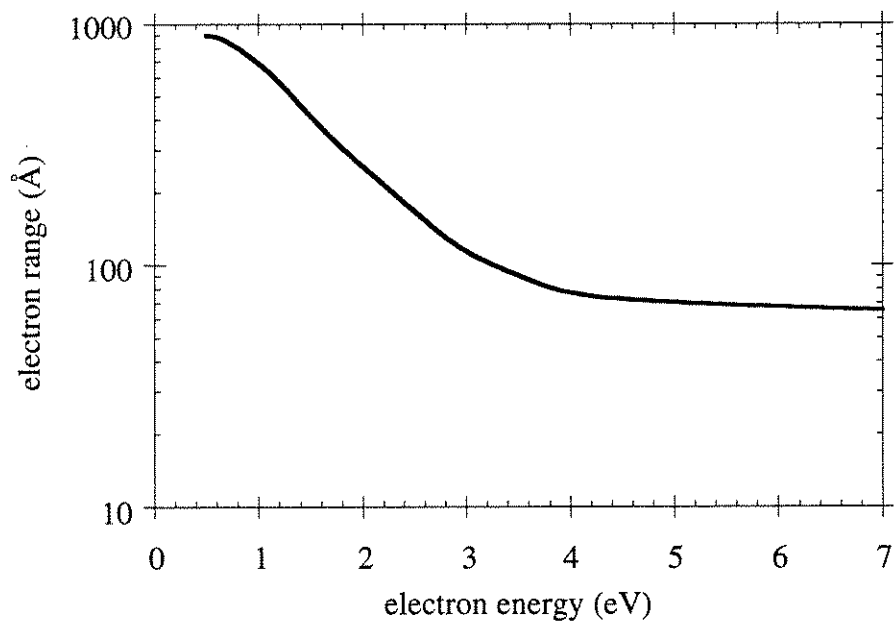


Figure 6.1: Empirical curve for electron range vs. excitation energy (with respect to the Fermi level) as measured in gold films.

cannot be excited above the Fermi level because the photoelectron energy is less than this energy difference, and there are no unoccupied energy states below the Fermi level. Thus no energy exchange between the conduction electrons below $\epsilon_F - \epsilon$ and the excited electron can take place. The greater the excitation energy ϵ , the larger the number of conduction electrons that the photoelectron can interact with, and therefore the shorter the electron range. Fig. 6.1 shows an empirical curve taken from [53] showing this behavior of the electron range l in gold films.

6.1.1 One-photon Emission

Linear photoemission from thin metal films can be investigated using a simple one-dimensional analysis [54]. This approach is sufficient because the isotropy of the electron velocities allows us to study motion in the \hat{z} direction (the direction normal to the surface) independent of the electron motion in the \hat{x} or \hat{y} directions. In addition, for optically excited electrons most of the kinetic energy must be in the \hat{z} direction in order to overcome the metal surface barrier, thus the emitted electrons will have had primarily z motion in the metal.

Fig. 6.2 depicts a laser pulse incident on a thin metal film of thickness d . Let us look at electrons at a depth z from the front surface (the surface onto which the laser pulse is incident). As the pulse propagates through the metal, its intensity decreases exponentially:

$$I(z) = I_0 e^{-z/\delta} \quad (6.1)$$

where δ is the optical absorption depth at the laser wavelength. The probability of an electron at depth z absorbing one photon is proportional to this intensity:

$$P_\gamma(z) \propto I_0 e^{-z/\delta} \quad (6.2)$$

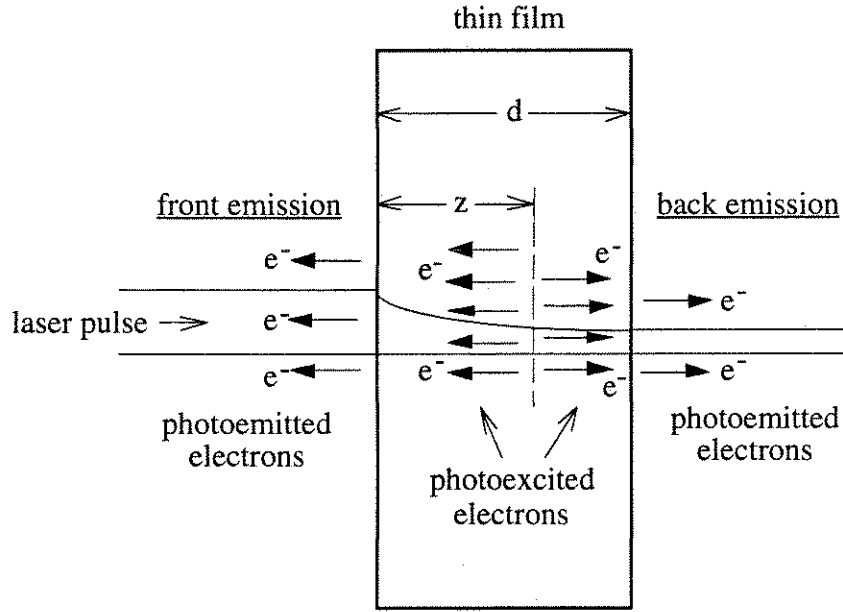


Figure 6.2: Front and back side photoemission from a film of thickness d .

An electron which absorbs a photon must then travel to the front surface without suffering a collision in order to have a chance to escape. The probability P_{nc} of no collision occurring over this distance z is

$$P_{nc}(z) \propto e^{-z/l} \quad (6.3)$$

Thus the total probability for the front surface emission of an electron from a depth z is

$$P_{front}(z) = P_{\gamma}(z) \cdot P_{nc}(z) \propto I_0 e^{-z/\delta} e^{-z/l} \quad (6.4)$$

For a film of thickness d , the electrons which lie a distance z from the front surface will be at a distance $d - z$ from the back surface. The probability for emission from the back surface is then

$$P_{back}(z) = P_{\gamma}(z) \cdot P_{nc}(d - z) \propto I_0 e^{-z/\delta} e^{-(d-z)/l} \quad (6.5)$$

To find the total electron yield from each surface, we must integrate the emission probabilities over the thickness of the film. For a given incident light intensity the emitted charge from the front is

$$Q_{front} \propto \int_0^d I_0 e^{-z/\delta} e^{-z/l} dz = \frac{I_0}{\frac{1}{\delta} + \frac{1}{l}} \left[1 - e^{-(\frac{1}{\delta} + \frac{1}{l})d} \right] \quad (6.6)$$

and the charge emitted from the back is

$$Q_{back} \propto \int_0^d I_0 e^{-z/\delta} e^{-(d-z)/l} dz = \frac{I_0}{\frac{1}{\delta} - \frac{1}{l}} \left[e^{-d/l} - e^{-d/\delta} \right] \quad (6.7)$$

We have ignored any internal surface reflections of the light or the photoelectrons. From Eqs. 3.4 and 3.10 we can write these expressions in terms of the measured b_1 coefficients:

$$b_{1\ front} = \frac{K_1}{\frac{1}{\delta} + \frac{1}{l}} \left[1 - e^{-(\frac{1}{\delta} + \frac{1}{l})d} \right] \quad (6.8)$$

$$b_{1\ back} = \frac{K_1}{\frac{1}{\delta} - \frac{1}{l}} \left[e^{-d/l} - e^{-d/\delta} \right] \quad (6.9)$$

where K_1 is the constant of proportionality having units of pC/($\mu\text{J}\cdot\text{\AA}$). For large thicknesses we should recover the bulk b_1 value measured in Sec. 3.3.2 from $b_{1\ front}$

$$\lim_{d \rightarrow \infty} b_{1\ front} = b_{1\ bulk} \quad (6.10)$$

and therefore we can determine the value of K_1 :

$$K_1 = \left(\frac{1}{\delta} + \frac{1}{l} \right) b_{1\ bulk} \quad (6.11)$$

Fig. 6.3 shows the behavior of Eqs. 6.8 and 6.9 as a function of film thickness d for 217 nm incident light on copper. We used the published optical absorption depth value for copper of $\delta_{217} = 105 \text{ \AA}$ [35] and the electron range value suggested by Fig. 6.1 of $l = 70 \text{ \AA}$ for a 5.7 eV excitation energy. For small film thicknesses ($d < l$) the front and back electron yields are equal and increase as the thickness

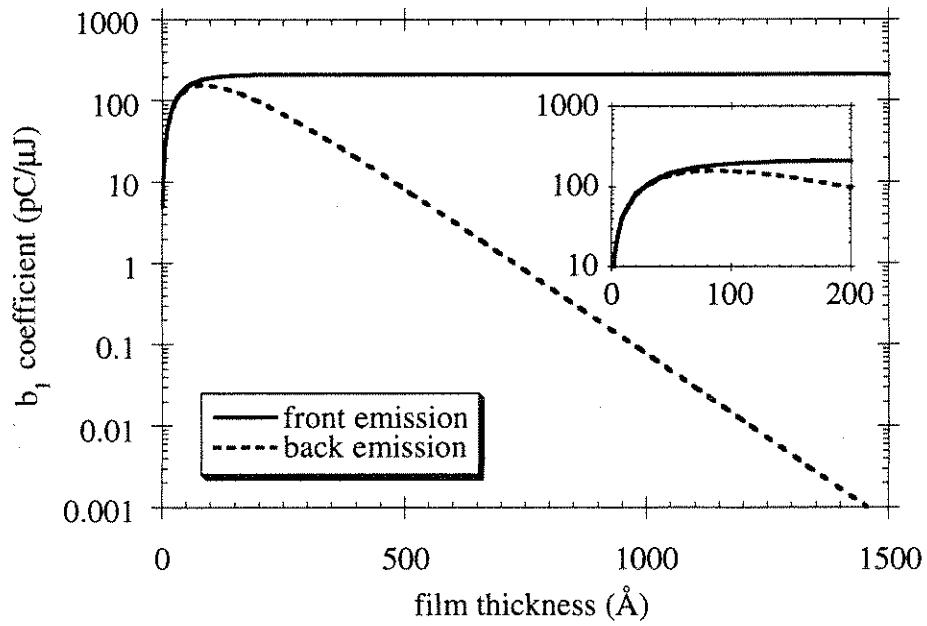


Figure 6.3: The theoretical behavior of the electron yield (as measured by the b_1 coefficient) vs. film thickness for front and back illumination of copper by 217 nm light. The optical absorption depth is taken to be $\delta_{217} = 105 \text{ \AA}$ and the electron range is $l = 70 \text{ \AA}$.

becomes larger. For greater thicknesses ($d > l$) the front yield reaches the bulk b_1 value after about 200 Å and remains constant, while the back yield turns around and decays exponentially, dropping by 5 orders of magnitude over 1500 Å.

6.1.2 Two-photon Emission

For 2-photon emission, the electron dynamics are a bit more complicated. Fig. 6.4 is a picture of a 2-photon emission process from the front surface of the metal film. This electron absorbs the first photon at z_1 , then travels toward the surface where it absorbs a second photon at z_2 . The doubly excited electron continues in this direction and eventually crosses the potential barrier at the front surface where it escapes the metal. The probability of these events occurring to produce front emission is

$$P_{front}(z_1, z_2) = P_\gamma(z_1)P_{nc1}(z_1 - z_2)P_\gamma(z_2)P_{nc2}(z_2) \quad (6.12)$$

The quantity $P_{nc1}(z)$ is the probability that the electron will travel a distance z without suffering a collision after it has absorbed one photon:

$$P_{nc1}(z) \propto e^{-z/l_1} \quad (6.13)$$

and $P_{nc2}(z)$ is the probability of the electron traveling a distance z without a collision after absorbing two photons:

$$P_{nc2}(z) \propto e^{-z/l_2} \quad (6.14)$$

Because the absorption of each photon increases the energy of the photoelectron, the electron range l_1 after absorbing one photon will be different than the electron range l_2 after absorbing two photons (as demonstrated in Fig. 6.1). A similar

analysis of an electron traveling toward the back surface yields

$$P_{back}(z_1, z_2) = P_\gamma(z_1)P_{nc1}(z_2 - z_1)P_\gamma(z_2)P_{nc2}(d - z_2) \quad (6.15)$$

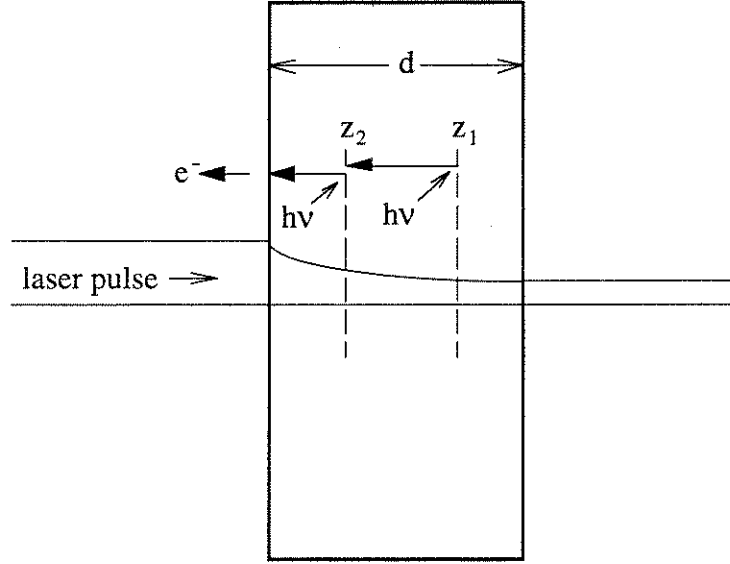


Figure 6.4: Two-photon front emission from a metal film of thickness d . The electron absorbs the first photon at z_1 (as measured from the front surface), absorbs a second photon at z_2 , and then travels to the surface where it is emitted.

To find the emitted charge from both surfaces we must integrate z_1 and z_2 over the thickness of the film:

$$Q_{front} \propto I_0^2 \int_0^d \int_0^{z_1} e^{-z_1/\delta} e^{-z_2/\delta} e^{-(z_1-z_2)/l_1} e^{-z_2/l_2} dz_2 dz_1 \quad (6.16)$$

$$Q_{back} \propto I_0^2 \int_0^d \int_{z_1}^d e^{-z_1/\delta} e^{-z_2/\delta} e^{-(z_2-z_1)/l_1} e^{-(d-z_2)/l_2} dz_2 dz_1 \quad (6.17)$$

$$(6.18)$$

Performing this integration and expressing the result in terms of the b_2 coefficient

gives

$$b_{2 \text{ front}} = K_2 \left[\frac{1}{\left(\frac{1}{\delta} + \frac{1}{l_1}\right) \left(\frac{2}{\delta} + \frac{1}{l_2}\right)} - \frac{e^{-\left(\frac{1}{\delta} + \frac{1}{l_1}\right)d}}{\left(\frac{1}{\delta} + \frac{1}{l_1}\right) \left(\frac{1}{\delta} - \frac{1}{l_1} + \frac{1}{l_2}\right)} + \frac{e^{-\left(\frac{2}{\delta} + \frac{1}{l_2}\right)d}}{\left(\frac{2}{\delta} + \frac{1}{l_2}\right) \left(\frac{1}{\delta} - \frac{1}{l_1} + \frac{1}{l_2}\right)} \right] \quad (6.19)$$

$$b_{2 \text{ back}} = K_2 \left[\frac{e^{-\frac{2d}{\delta}}}{\left(\frac{1}{\delta} - \frac{1}{l_1}\right) \left(\frac{2}{\delta} - \frac{1}{l_2}\right)} - \frac{e^{-\left(\frac{1}{\delta} + \frac{1}{l_1}\right)d}}{\left(\frac{1}{\delta} - \frac{1}{l_1}\right) \left(\frac{1}{\delta} + \frac{1}{l_1} - \frac{1}{l_2}\right)} + \frac{e^{-\frac{d}{l_2}}}{\left(\frac{2}{\delta} - \frac{1}{l_2}\right) \left(\frac{1}{\delta} + \frac{1}{l_1} - \frac{1}{l_2}\right)} \right] \quad (6.20)$$

Fig. 6.5 shows the behavior of Eqs. 6.19 and 6.20. As before, K_2 is determined by the bulk b_2 value:

$$K_2 = \left(\frac{1}{\delta} + \frac{1}{l_1}\right) \left(\frac{2}{\delta} + \frac{1}{l_2}\right) b_{2 \text{ bulk}} \quad (6.21)$$

The absorption depth for copper at this wavelength is listed as $\delta_{217} = 105 \text{ \AA}$ [35] and the electron range values from Fig. 6.1 are $l_1 = 75 \text{ \AA}$ for a 1-photon 3.8 eV excitation energy and $l_2 = 65 \text{ \AA}$ for a 2-photon 7.6 eV energy. Note that the 2-photon front emission rises more slowly than the 1-photon emission, reaching the bulk b_2 value after about 250 \AA . The back emission, however, falls off more quickly—dropping by 7 orders of magnitude over 1500 \AA .

6.1.3 Three-photon Emission

Finally, we will look at the electron dynamics of 3-photon emission. Fig. 6.6 shows a picture of a 3-photon front emission process from a metal film. The

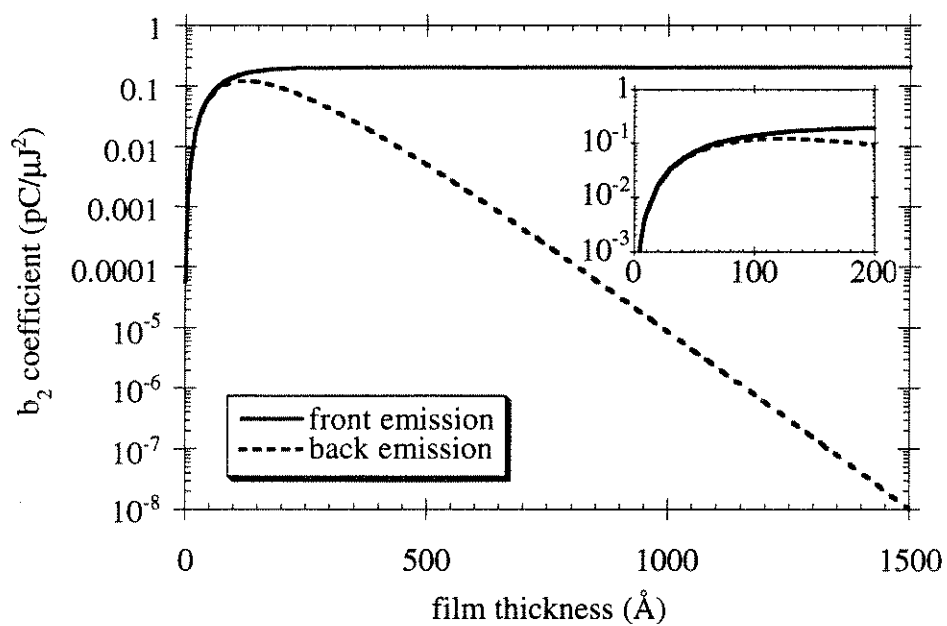


Figure 6.5: Theoretical behavior of the 2-photon electron yield (as measured by the b_2 coefficient) vs. film thickness for front and back illumination of copper by 325 nm light. The optical absorption depth is $\delta_{325} = 145 \text{ \AA}$ and the electron ranges are $l_1 = 75 \text{ \AA}$ and $l_2 = 65 \text{ \AA}$.

electron absorbs the first photon at z_1 , travels to z_2 where it absorbs a second photon, travels to z_3 and absorbs a third photon, then propagates to the front surface and escapes the metal. The probability of this sequence of events is

$$P_{front}(z_1, z_2, z_3) = P_\gamma(z_1)P_{nc1}(z_1 - z_2)P_\gamma(z_2)P_{nc2}(z_2 - z_3)P_\gamma(z_3)P_{nc3}(z_3) \quad (6.22)$$

The corresponding analysis for an electron traveling to the back surface gives

$$P_{back}(z_1, z_2, z_3) = P_\gamma(z_1)P_{nc1}(z_2 - z_1)P_\gamma(z_2)P_{nc2}(z_3 - z_2)P_\gamma(z_3)P_{nc3}(d - z_3) \quad (6.23)$$

Again we must integrate z_1 , z_2 , and z_3 over the sample thickness to find the emitted charge:

$$Q_{front} \propto I_0^3 \int_0^d \int_0^{z_1} \int_0^{z_2} e^{-z_1/\delta} e^{-z_2/\delta} e^{-z_3/\delta} e^{-(z_1-z_2)/l_1} \times e^{-(z_2-z_3)/l_2} e^{-z_3/l_3} dz_3 dz_2 dz_1 \quad (6.24)$$

$$Q_{back} \propto I_0^3 \int_0^d \int_{z_1}^d \int_{z_2}^d e^{-z_1/\delta} e^{-z_2/\delta} e^{-z_3/\delta} e^{-(z_2-z_1)/l_1} \times e^{-(z_3-z_2)/l_2} e^{(d-z_3)/l_3} dz_3 dz_2 dz_1 \quad (6.25)$$

Expressing the yield in terms of the b_3 coefficients after a painful integration gives

$$b_{3\ front} = K_3 \left[\frac{1}{\left(\frac{1}{\delta} + \frac{1}{l_1}\right) \left(\frac{2}{\delta} + \frac{1}{l_2}\right) \left(\frac{3}{\delta} + \frac{1}{l_3}\right)} - \frac{e^{-\left(\frac{1}{\delta} + \frac{1}{l_1}\right)d}}{\left(\frac{1}{\delta} + \frac{1}{l_1}\right) \left(\frac{1}{\delta} - \frac{1}{l_1} + \frac{1}{l_2}\right) \left(\frac{2}{\delta} - \frac{1}{l_1} + \frac{1}{l_3}\right)} + \frac{e^{-\left(\frac{2}{\delta} + \frac{1}{l_2}\right)d}}{\left(\frac{2}{\delta} + \frac{1}{l_2}\right) \left(\frac{1}{\delta} - \frac{1}{l_1} + \frac{1}{l_2}\right) \left(\frac{1}{\delta} - \frac{1}{l_2} + \frac{1}{l_3}\right)} - \frac{e^{-\left(\frac{3}{\delta} + \frac{1}{l_3}\right)d}}{\left(\frac{3}{\delta} + \frac{1}{l_3}\right) \left(\frac{2}{\delta} - \frac{1}{l_1} + \frac{1}{l_3}\right) \left(\frac{1}{\delta} - \frac{1}{l_2} + \frac{1}{l_3}\right)} \right] \quad (6.26)$$

$$b_{3 \text{ back}} = K_3 \left[\frac{-e^{-\frac{3d}{\delta}}}{\left(\frac{1}{\delta} - \frac{1}{l_1}\right) \left(\frac{2}{\delta} - \frac{1}{l_2}\right) \left(\frac{3}{\delta} - \frac{1}{l_3}\right)} + \frac{e^{-\left(\frac{2}{\delta} + \frac{1}{l_1}\right)d}}{\left(\frac{1}{\delta} - \frac{1}{l_1}\right) \left(\frac{1}{\delta} + \frac{1}{l_1} - \frac{1}{l_2}\right) \left(\frac{2}{\delta} + \frac{1}{l_1} - \frac{1}{l_3}\right)} \right. \\ \left. - \frac{e^{-\left(\frac{1}{\delta} + \frac{1}{l_2}\right)d}}{\left(\frac{2}{\delta} - \frac{1}{l_2}\right) \left(\frac{1}{\delta} + \frac{1}{l_1} - \frac{1}{l_2}\right) \left(\frac{1}{\delta} + \frac{1}{l_2} - \frac{1}{l_3}\right)} + \frac{e^{-\frac{d}{l_3}}}{\left(\frac{3}{\delta} - \frac{1}{l_3}\right) \left(\frac{2}{\delta} + \frac{1}{l_1} - \frac{1}{l_3}\right) \left(\frac{1}{\delta} + \frac{1}{l_2} - \frac{1}{l_3}\right)} \right] \quad (6.27)$$

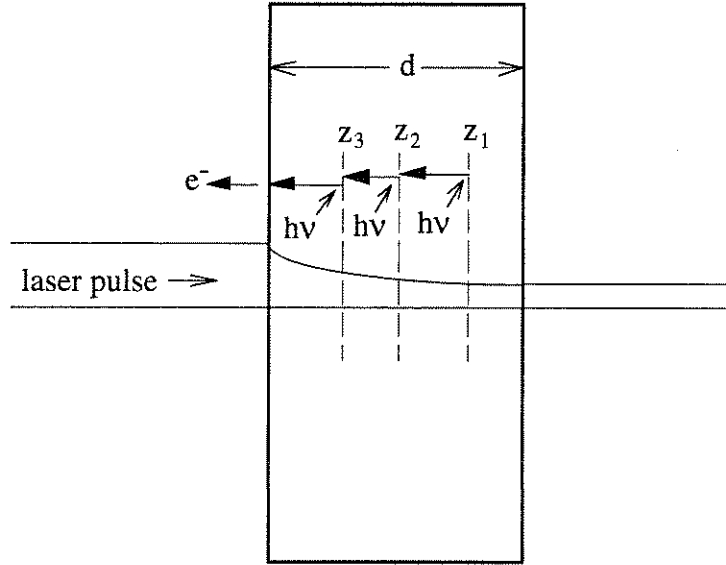


Figure 6.6: Three-photon front emission from a metal film of thickness d . The electron absorbs the first photon at z_1 , a second photon at z_2 , a third at z_3 , and then is emitted from the front surface.

The plots of Eqs. 6.26 and 6.27 are shown in Fig. 6.7. The K_3 coefficient is given by

$$K_3 = \left(\frac{1}{\delta} + \frac{1}{l_1}\right) \left(\frac{2}{\delta} + \frac{1}{l_2}\right) \left(\frac{3}{\delta} + \frac{1}{l_3}\right) b_{3 \text{ bulk}} \quad (6.28)$$

The absorption depth from [35] is $\delta_{650} = 154 \text{ \AA}$ and the electron ranges after excitation by one, two, and three 650 nm (1.9 eV) photons are taken from Fig. 6.1

to be $l_1 = 200 \text{ \AA}$, $l_2 = 75 \text{ \AA}$, and $l_3 = 70 \text{ \AA}$. The front emission curve rises more slowly than the previous two wavelengths, reaching the bulk b_3 value after 350 \AA . The back emission curve also rises slowly and then, like the 325 nm curve, decays by 7 orders of magnitude over the 1500 \AA thickness.

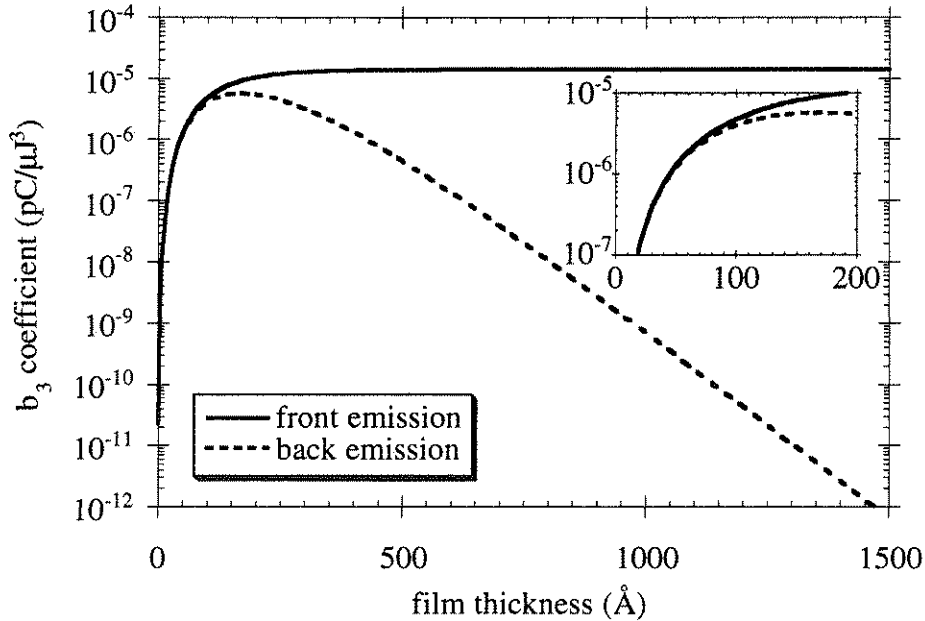


Figure 6.7: Theoretical behavior of the 3-photon electron yield (in terms of the b_3 coefficient) vs. film thickness for front and back illumination of copper by 650 nm light. The optical absorption depth is $\delta_{650} = 154 \text{ \AA}$ and the electron ranges are $l_1 = 200 \text{ \AA}$, $l_2 = 75 \text{ \AA}$, and $l_3 = 70 \text{ \AA}$.

6.2 Front and Back Illumination Experiment

The setup for the multiphoton thin film illumination experiment is shown in Fig. 6.8. The samples were $1'' \times 2''$ fused silica slides with steps of various thicknesses of copper film evaporated onto one side. Two samples were used, one with film thicknesses ranging from $50\text{--}500 \text{ \AA}$ and the other with thicknesses $500\text{--}1400$

Å. The hollow anode was mounted on a rotation stage with an external control so that it could be positioned on either side of the sample for the front illumination (Fig. 6.8a) and back illumination (Fig. 6.8b) configurations. A mechanical feedthrough was used to move the sample to illuminate each thickness and also to flip the slide so that the copper side would face the anode for each configuration. The transmission of the laser pulse through each thickness of copper film was measured using a photodiode placed behind the sample outside of the vacuum chamber.

These transmission measurements for each laser wavelength are shown in Fig. 6.9. By fitting an exponential to each curve we can determine the optical absorption depths from Eq. 6.1:

$$\delta_{217} = 107 \text{ \AA}$$

$$\delta_{325} = 138 \text{ \AA}$$

$$\delta_{650} = 154 \text{ \AA}$$

The published values [35] of the absorption depths for copper at these wavelengths are 105 Å, 145 Å, and 154 Å, respectively—thus we are in excellent agreement with these values.

We performed the usual emitted charge vs. laser energy traces with the 217, 325, and 650 nm pulses for both front and back side illumination for each thickness of copper film. All of the traces demonstrated the expected slopes 1, 2, and 3 for the respective wavelengths. From these traces we determined the b_n coefficients for each copper thickness in each configuration. By plotting the front and back b_n coefficients vs. film thickness, we hope to get an idea of the relative contribution of the surface vs. bulk electrons and also a measurement of the maximum electron

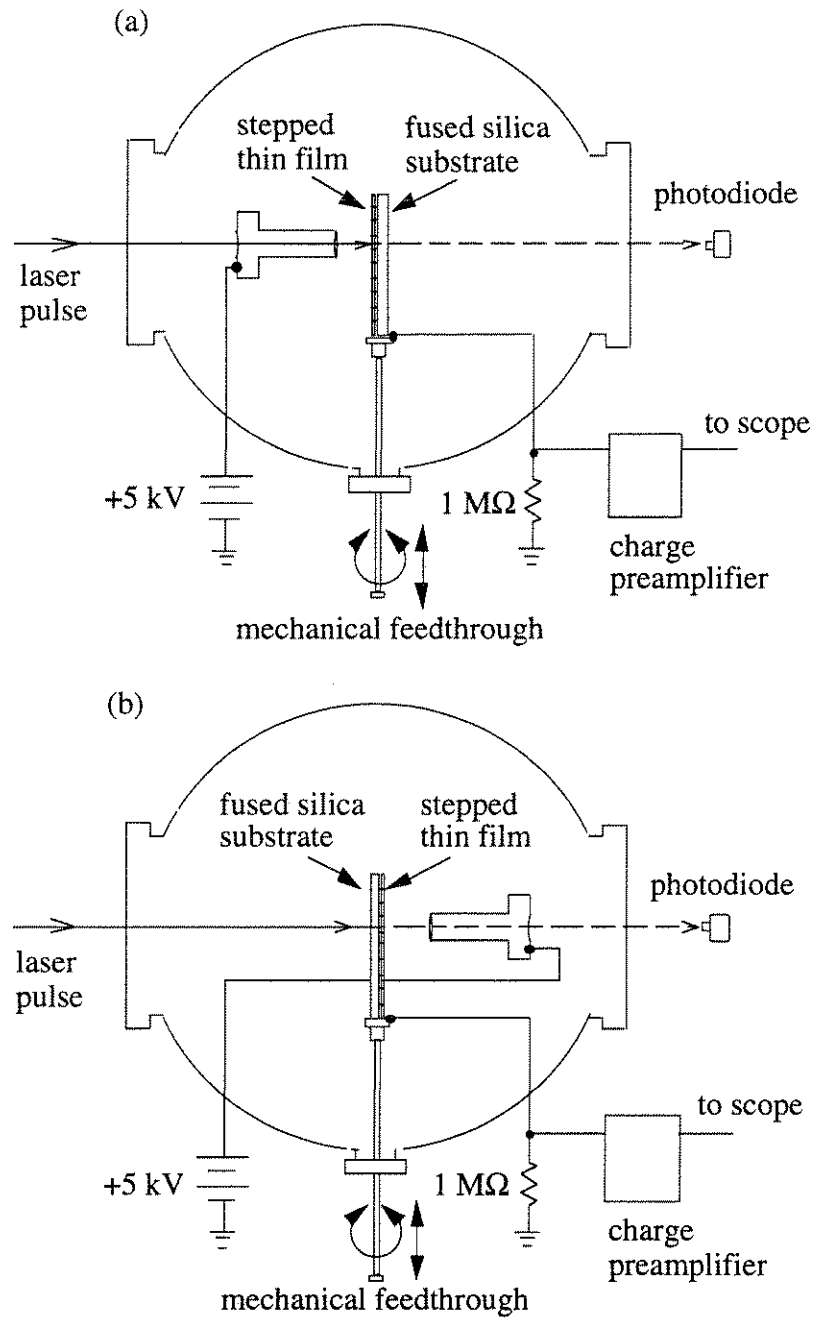


Figure 6.8: Setup for the multiphoton thin film illumination experiment: (a) front illumination configuration (b) back illumination configuration.

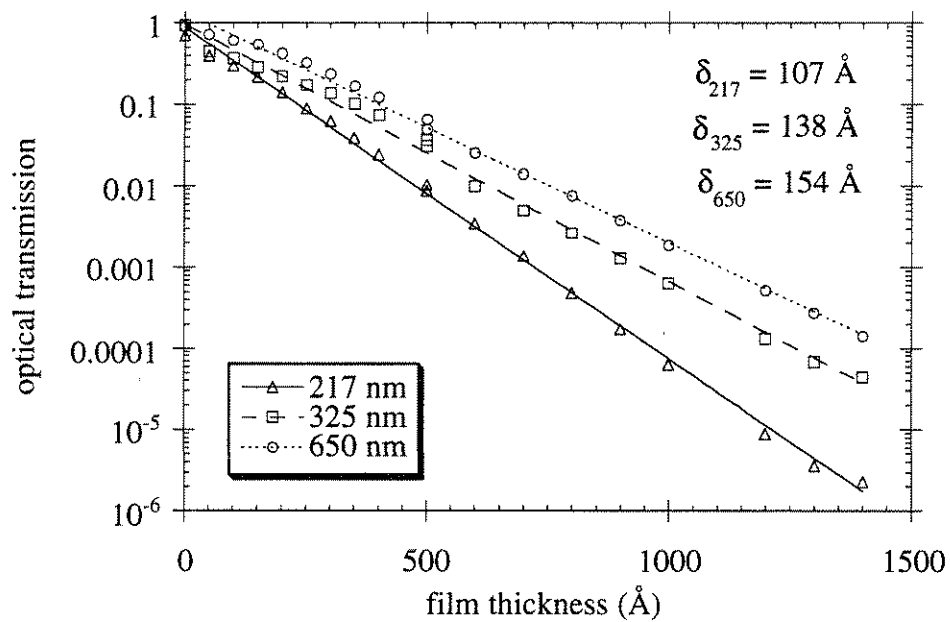


Figure 6.9: Optical transmission vs. copper film thickness for 217, 325, and 650 nm laser wavelengths. The solid and dashed curves are exponential fits from which the absorption depths are calculated to be $\delta_{217} = 107 \text{ \AA}$, $\delta_{325} = 138 \text{ \AA}$, and $\delta_{650} = 154 \text{ \AA}$.

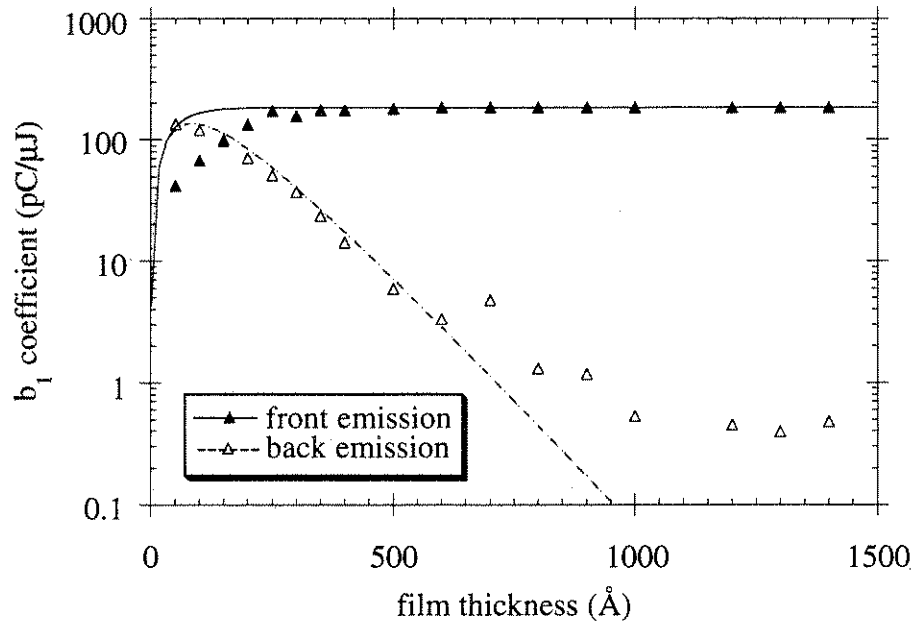


Figure 6.10: The measured 1-photon yield (b_1 coefficients) vs. copper film thickness for front and back illumination by 217 nm laser pulses, plotted with the theoretical curves. The maximum emission depth is 250 Å.

escape depth.

Fig. 6.10 is a plot of the b_1 coefficients vs. film thickness for 217 nm incident laser pulses. The front b_1 coefficients increase as the films become thicker until they reach a bulk value of $b_n = 190 \text{ pC}/\mu\text{J}$ at 250 Å. This increase is more gradual than predicted by the theory. As the films become thicker than this value we observe no additional emitted charge, thus we take 250 Å to be the maximum depth from which electrons can escape the metal for this incident wavelength. Note that the front emission from thicknesses $d > 250 \text{ Å}$ is a factor of five greater than the emission from the thinnest 50 Å sample. This indicates that the majority of the emitted electrons originated in the bulk of the metal and not on the surface. The back b_1 coefficients initially decay exponentially, but

then reach a constant value of ~ 0.2 pC/ μ J at 1000 Å. However, this charge was found to be present with no sample in place—therefore it is background charge caused by scattered 217 nm light.

An unexpected result shown in this plot is that for small thicknesses (50 and 100 Å) the back electron yield is greater than the front yield. However, this may be due to the presence of copper oxide or other contaminants on the metal surface. In the front illumination configuration the laser pulses are incident on the bare copper side; any surface contaminants may absorb some of the light and thereby reduce the energy available to the conduction electrons. In the back illumination configuration, on the other hand, the laser pulses are incident on the surface which has been deposited on the fused silica substrate. This surface is protected by the substrate and thus has no contaminants which may absorb the light. Therefore, for small thicknesses the back emission can be greater because the laser energy incident on the conduction electrons is higher.

Fig. 6.11 shows the b_2 coefficients vs. film thickness for the front and back illumination by 325 nm incident light. The constant of proportionality K_2 was reduced for the front theoretical curve independently of the back curve to account for contaminants decreasing the front emission. The yield from the front reaches a bulk value of $b_2 = 0.14$ pC/ μ J² at the maximum electron escape depth of 350 Å. The measured front emission increase is much more gradual than the theory predicts. For this wavelength the bulk emission is about a factor of two greater than the 50 Å emission—again the majority of electrons originate in the bulk and not on the metal surface.

The back emission data points follow the theoretical curve quite well up to 500 Å, at which point the data begins to oscillate about 0.25 pC/ μ J² while the

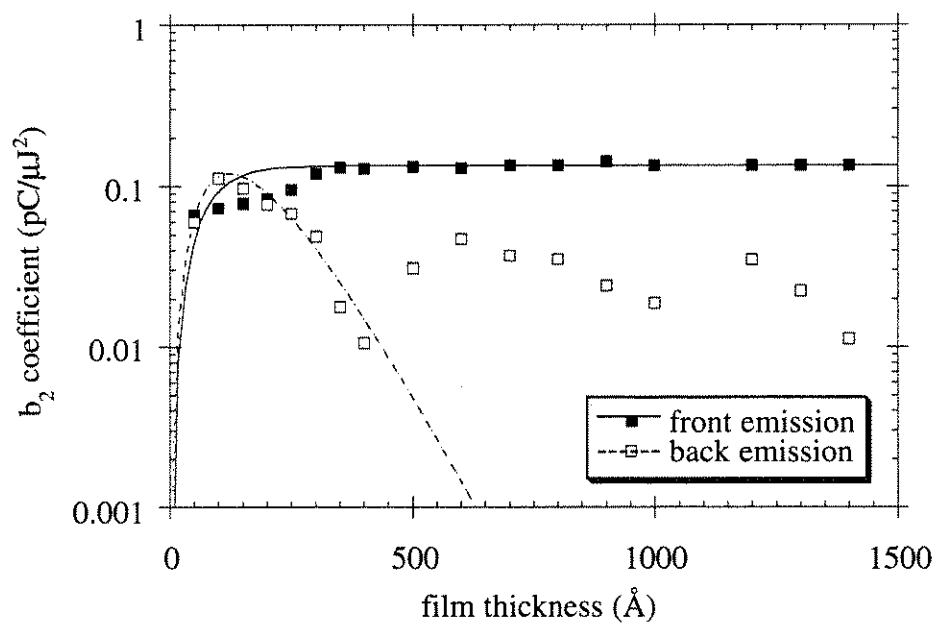


Figure 6.11: The 2-photon yield (b_2 coefficients) vs. copper film thickness for front and back illumination by 325 nm laser pulses, plotted with the theoretical curves. The maximum emission depth is 350 Å.

theoretical curve continues to decrease exponentially. There was no background charge observed without the sample in place as was the case with the 217 nm measurements.

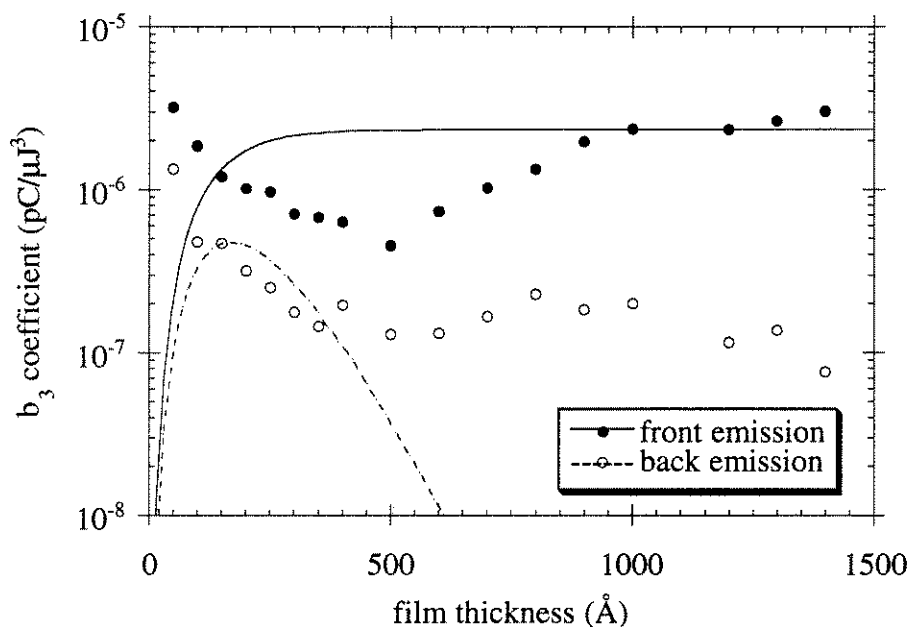


Figure 6.12: The 3-photon yield (b_3 coefficients) vs. copper film thickness for front and back illumination by 650 nm laser pulses, plotted with the theoretical curves.

The front and back electron yields for incident 650 nm laser pulses are shown in Fig. 6.12. The K_3 constant for the theoretical curves was adjusted independently for the front and back emission in an attempt to best fit the data in the presence of possible surface contamination. Clearly, there is poor agreement between the experimental data and the theoretical curves. Both the front and back emission data points initially decrease until about 500 Å, after which the front emission increases to a value of 2.3×10^{-6} pC/ μJ^3 while the back emission remains roughly constant. No maximum electron escape depth can be discerned from this data.

6.3 Emission Promptness

The measurements of the maximum emission depth d_{max} can be used to obtain an upper limit on the time delay between an incident laser pulse and the resulting emitted electron bunch. Because the photoemitted electrons traveled ballistically to the metal surface, the maximum time delay will be the transit time for electrons from the maximum emission depth to reach the surface:

$$\Delta t_{max} = \frac{d_{max}}{v_e} \quad (6.29)$$

For 1-photon emission, the minimum electron velocity v_e for escape will be the Fermi velocity v_F plus the velocity required to overcome the work function $v_{e\Phi}$:

$$v_e = v_F + v_{e\Phi} = \sqrt{\frac{2\epsilon_F}{m_e}} + \sqrt{\frac{2e\Phi}{m_e}} \quad (6.30)$$

where m_e is the electron mass. For copper $\epsilon_F = 7.0$ eV and $e\Phi = 4.6$ eV, thus the minimum escape velocity is

$$v_e = 2.0 \times 10^6 \text{ m/s}$$

For the maximum escape depth $d_{max} = 250$ Å measured for the 217 nm emission, the delay time is

$$\Delta t_{max} = 12 \text{ fs}$$

A similar analysis for the 2-photon 325 nm emission (assuming the longest delay scenario where the electron absorbs the first photon at the measured $d_{max} = 350$ Å and the second photon right at the surface) gives a delay time of

$$\Delta t_{max} = 21 \text{ fs}$$

We can perform a theoretical analysis for the maximum delay time for 3-photon emission at 650 nm. From Fig. 6.7 the maximum escape depth is approximately 350 Å. We will assume the longest delay scenario in which an electron at the maximum depth absorbs one 650 nm photon, then travels to the surface where it absorbs the remaining two photons in order to escape. This also gives a delay time of

$$\Delta t_{max} = 21 \text{ fs}$$

For laser systems producing pulses > 100 fs, these emission delays will be negligible in comparison with the laser pulsewidth. Therefore, an RF gun or other accelerator operating below the space charge regime will produce an initial electron bunch having nearly the same temporal profile as the incident laser pulse (space charge effects and beam line optics may broaden the electron bunch in time). Further electron pulse compression may not be necessary by the beam line optics.

Another result from this chapter is that the electron yield from the back side of a thin copper film can be comparable to the yield from the front side of bulk copper. For example, the 1-photon yield from the back emission of a 150 Å film is only a factor of two less than the front bulk yield (Fig. 6.10). Thus a back illuminated photocathode could be used in devices such as high frequency RF linacs and synchotrons where laser beam access from the front side is difficult or impossible. Such a photocathode would allow for synchronization to RF cycles or other fast events down the beam line (such as a beat-wave accelerator) which is not possible with conventional thermionic cathodes.

Chapter 7

Conclusions

Using an amplified ultrafast dye laser system, we were able to investigate many issues concerning linear and nonlinear photoemission processes and materials from which photoelectrons are produced. We identified 1-, 2-, and 3-photon emission from copper, silicon, diamond, and fullerene. The emission was induced by illuminating these materials with 217, 325, and 650 nm laser pulses. The amount of charge produced is proportional to the laser intensity I for 1-photon emission, I^2 for 2-photon emission, and I^3 for 3-photon emission. At the laser intensities used (up to ~ 10 GW/cm²), pure multiphoton emission was the dominant process—no evidence of thermally-enhanced or thermionic emission was observed. In addition, for these laser intensities 1-photon emission consistently produced several orders of magnitude more charge than 2-photon emission, which in turn produced several orders of magnitude more charge than 3-photon photoemission. Thus for typical subpicosecond laser systems a 1-photon process is necessary for applications which require a high emitted charge. However, because of its I^n dependence a multiphoton emitter would produce an electron bunch having a factor of \sqrt{n} shorter in duration than the incident laser pulse. For copper the quantum efficiency of 1-photon emission at 217 nm was measured to be $\eta_{217} = 1.2 \times 10^{-3}$.

We also observed the first multicolor emission process. This was done by sending both 650 and 325 nm pulses colinearly to the copper photocathode and varying the time delay between them. There was an enhancement of charge when the pulses overlapped in time, indicating a process whereby electrons absorb one 650 nm and one 325 nm photon to gain the required energy for photoemission. This effect could be useful for synchronizing two or more non-harmonic subpicosecond laser pulses in space and time.

Emission properties of copper and magnesium cathodes were studied using frequency quadrupled Nd:YAG pulses ($\lambda = 266$ nm) to produce 1-photon emission. The quantum efficiency of copper at this wavelength is significantly less than at 217 nm ($\eta_{266} = 1.0 \times 10^{-5}$) which is expected from the frequency dependence of the Fowler-DuBridge theory. The quantum efficiency of magnesium was initially less than copper but after performing laser cleaning (which included ablating the surface) the magnesium quantum efficiency increased by a factor of 220 to 1.5×10^{-4} . However, this high quantum efficiency immediately began to decay as contaminants in the vacuum chamber were redeposited on the surface. Copper showed much less change after laser cleaning and thus is a more stable photocathode material.

The copper cathodes in the UCLA RF photoinjector gun, however, did show deterioration in quantum efficiency over time. Fortunately, this may not be an unavoidable deleterious effect. Although the vacuum environment in the RF gun ($P < 10^{-8}$ torr) was at least two orders of magnitude better than the DC test gun setup, the RF gun was found later to be contaminated by viton and other contaminants which probably led to the decrease of the cathode quantum efficiency and uniformity of emission over time. To study the effects of this contamination

we used the DC test gun with a moveable cathode mount to produce quantum efficiency maps of the photocathode surface. A cathode which had been used in the RF gun for over four months showed variations up to a factor of eight in quantum efficiency across the surface. A cathode which was used in the gun for one week showed an increase in emission uniformity but a decrease in overall quantum efficiency, most likely due to a smoothing of its surface by the high RF fields.

These results led us to investigate other materials which may be more stable in an RF gun environment. We examined emission properties of various dopings of silicon, diamond, and fullerene at 217, 325, and 650 nm wavelengths. Of these, boron-doped diamond showed the most promise as a photocathode material. Its single-photon quantum efficiency was about 20% of that of copper, but showed a higher damage threshold and is much less susceptible to contamination because of its extremely low reactivity. The product of the quantum efficiency and damage threshold $\eta\mathcal{E}_{dam}$ (which we take to be a measure of photocathode suitability) of the boron-doped diamond film was comparable to that of copper, while the estimated $\eta\mathcal{E}_{dam}$ for boron-doped bulk diamond (or high quality boron-doped diamond film) is much higher than copper.

Finally, we studied some of the electron dynamics of photoemission by performing front and back illumination experiments on thin copper films. We found that for thicknesses of 150 Å or less the back emission is a significant fraction of the front emission, and can even be greater due to the front side contamination of the copper. This may be useful for devices such as high frequency RF linacs and synchrotrons where laser beam access from the front side is difficult or impossible. In such cases a thin film photocathode illuminated from the back side

could replace the conventional thermionic cathode and therefore produce shorter pulses, higher peak currents, and allow for laser synchronization of the electron pulses to other events in the device or the experiment.

The maximum electron escape depth from copper at 217 nm was measured to be 250 Å, and the escape depth for 2-photon emission at 325 nm was 350 Å. The results for the 3-photon emission at 650 nm were inconsistent with the other wavelengths and with the simple electron transport theory that was used. The theory predicts an escape depth at 650 nm of 350 Å. The escape depths can be used to estimate the promptness of the electron emission. The delay time between the incident laser pulse and the electrons emitted from the maximum escape depth was calculated to be 12 fs and 21 fs for the 217 and 325 nm light, respectively. The calculation for the 650 nm light using the theoretical escape depth also gave a delay time of 21 fs. These delays will limit the minimum electron pulsewidth attainable with an ultrashort laser pulse. For typical picosecond and subpicosecond laser pulses used in RF photoinjectors, however, the electron bunch broadening due to these emission delays will be insignificant.

Bibliography

- [1] H. Hertz. *Ann. d. Phys.*, 31:983, 1887.
- [2] J. J. Thomson. *Phil. Mag.*, 48:547, 1899.
- [3] P. Lenard. *Wien. Ber.*, 108:649, 1899.
- [4] A. Einstein. *Ann. d. Phys.*, 17:132, 1905.
- [5] M. Planck. *Verh. D. Phys. Ges.*, 2, 1900.
- [6] R. H. Fowler. The analysis of photoelectric sensitivity curves for clean metals at various temperatures. *Phys. Rev.*, 38:45–56, Jul 1931.
- [7] L. A. DuBridge. A further experimental test of Fowler's theory of photoelectric emission. *Phys. Rev.*, 39:108–18, Jan 1932.
- [8] F. Reif. *Fundamentals of Statistical and Thermal Physics*. McGraw-Hill, 1965.
- [9] J. H. Bechtel, W. L. Smith, and N. Bloembergen. Two-photon photoemission from metals induced by picosecond laser pulses. *Phys. Rev. B*, 15(10):4557–63, May 1977.
- [10] O. W. Richardson. *Proc. Camb. Phil. Soc. Math. Phys. Sci.*, 11:286, 1902.

- [11] O. W. Richardson. *Phil. Mag.*, 28:633, 1914.
- [12] S. Dushman. *Phys. Rev.*, 21:623, 1923.
- [13] B. Feuerbacher, B. Fitton, and R. F. Willis, editors. *Photoemission and the electronic properties of surfaces*, chapter 1. John Wiley and Sons, 1978.
- [14] I. Tamm and S. Schubin. *Z. Physik*, 68:97, 1931.
- [15] K. Mitchell. The theory of the surface photoelectric effect in metals. *Proc. Roy. Soc.*, A146:442, 1934.
- [16] L. I. Schiff and L. H. Thomas. Quantum theory of metallic reflection. *Phys. Rev.*, 47:860–69, 1935.
- [17] R. E. B. Makinson. Metallic reflexion and the surface photoelectric effect. *Proc. Roy. Soc.*, A162:367–90, 1937.
- [18] R. Suhrmann and H. Theissing. *Z. Physik*, 55:701, 1929.
- [19] G. W. Gobeli, F. G. Allen, and E. O. Kane. *Phys. Rev. Lett.*, 12:94, 1964.
- [20] C. N. Berglund and W. E. Spicer. *Phys. Rev.*, 136:A1030, 1964.
- [21] B. J. Waclawski and E. W. Plummer. *Phys. Rev. Lett.*, 29:783, 1972.
- [22] B. Feuerbacher and B. Fitton. *Phys. Rev. Lett.*, 29:786, 1972.
- [23] G. D. Mahan. *Phys. Rev. Lett.*, 24:1068, 1970.
- [24] T. H. Maiman. *Nature*, 187:493, 1960.
- [25] H. Sonnenberg, H. Heffner, and W. Spicer. *Appl. Phys. Lett.*, 5:95, 1964.

- [26] E. M. Logothetis and P. L. Hartman. Laser induced emission from solids: Many photon photoelectric effects and thermionic emission. *Phys. Rev.*, 187(2):460–74, 1969.
- [27] G. L. Eesley. Observation of nonequilibrium electron heating in copper. *Phys. Rev. Lett.*, 51(23):2140–43, 1983.
- [28] R. W. Schoenlein, W. Z. Lin, J. G. Fujimoto, and G. L. Eesley. Femtosecond studies of nonequilibrium electronic processes in metals. *Phys. Rev. Lett.*, 58(16):1680–83, 1987.
- [29] R. W. Schoenlein, J. G. Fujimoto, G. L. Eesley, and T. W. Capehart. Femtosecond studies of image-potential dynamics in metals. *Phys. Rev. Lett.*, 61(22):2596–99, Nov 1988.
- [30] T. Tsang, T. Srinivasan-Rao, and J. Fisher. Surface-plasmon field-enhanced multiphoton photoelectric emission from metal films. *Phys. Rev. B*, 43(11):8870–78, 1991.
- [31] J. Fisher, T. Srinivasan-Rao, T. Tsang, and G. Brandes. Photoemission from magnesium and from diamond film using high intensity laser beams. *Nucl. Inst. Meth. A*, 340:190–94, 1994.
- [32] D. L. Lichtenberger, K. W. Nebesny, C. D. Ray, D. R. Huffman, and Lowell D. Lamb. Valence and core photoelectron spectroscopy of C₆₀, buckminsterfullerene. *Chem. Phys. Lett.*, 176(2):203–08, Jan 1991.
- [33] T. Maruyama, E. L. Garwin, R. A. Mair, R. Prepost, J. S. Smith, and J. D. Walker. Electron-spin polarization in photoemission from thin Al_xGA_{1-x}As. *J. Appl. Phys.*, 73:5189–92, 1993.

- [34] P. Muggli, R. Brogle, and C. Joshi. Two-color photoemission using femtosecond laser pulses on copper. *J. Opt. Soc. Am. B*, 12(4):553–58, Apr 1995.
- [35] R. C. Weast, editor. *Handbook of Chemistry and Physics*. CRC Press, Boca Raton, Florida, 1984.
- [36] W. Schottky. *Z. Phys.*, 14:63, 1923.
- [37] H. E. Elsayed-Ali, T. B. Norris, M. A. Pessot, and G. A. Mourou. Time-resolved observation of electron-phonon relaxation in copper. *Phys. Rev. Lett.*, 58(12):1212–15, Mar 1986.
- [38] J. J. Quinn and R. A. Ferrell. Electron self-energy approach to correlation in a degenerate electron gas. *Phys. Rev.*, 112(3):812–27, Nov 1958.
- [39] S. C. Hartman, N. Barov, C. Pellegrini, S. Park, J. Rosenzweig, G. Travish, R. Zhang, C. Clayton, P. Davis, M. Everett, C. Joshi, and G. Hairapetian. Initial measurements of the UCLA RF photoinjector. *Nucl. Inst. Meth. A*, 340(1):219–30, Feb 1994.
- [40] E. Chevallay, J. Durand, S. Hutchins, G. Suberlucq, and M. Wurgel. Photocathodes tested in the dc gun of the CERN photoemission laboratory. *Nucl. Inst. Meth. A*, 340:146–56, 1994.
- [41] R. Brogle, P. Muggli, and C. Joshi. Studies of linear and nonlinear photoelectric emission for advanced accelerator applications. In *Proceedings of the 1995 Particle Accelerator Conference, Dallas, Texas*, May 1995.

- [42] P. Davis, G. Hairapetian, M. Hogan, C. Joshi, M. Lampel, S. Park, C. Pellegrini, J. Rosenzweig, G. Travish, and R. Zhang. The UCLA compact high brightness electron accelerator. In *Proceedings of the 1995 Particle Accelerator Conference, Dallas, Texas, May 1995*.
- [43] N. W. Ashcroft and N. D. Mermin. *Solid State Physics*. Saunders College Publishing, 1976.
- [44] F. G. Allen and G. W. Gobeli. Work function, photoelectric threshold, and surface states of atomically clean silicon. *Phys. Rev.*, 127(1):150–58, 1962.
- [45] P. Muggli, R. Brogle, S. Jou, H. J. Doerr, R. F. Bunshah, and C. Joshi. Photoemission from diamond and fullerene films for advanced accelerator applications. *IEEE Trans. Plas. Sci.*, 24(2), Apr 1996.
- [46] F. J. Himpsel, J. A. Knapp, J. A. VanVechten, and D. E. Eastman. Quantum photoyield of diamond (111)—a stable negative affinity emitter. *Phys. Rev. B.*, 20(2):624–27, 1979.
- [47] J. van der Weide and F. J. Nemanich. Argon and hydrogen plasma interaction on diamond (111) surfaces: Electronic states and structure. *Appl. Rev. Lett.*, 62(16):1878–80, 1993.
- [48] S. Jou, H. J. Doerr, and R. F. Bunshah. Diamond coatings from a solid carbon source. *Thin Solid Films*, 253:95–102, 1994.
- [49] R. C. Hadon, A. F. Hebard, M. J. Rosseinsky, D. W. Murphy, S. J. Duclos, K. B. Lyons, B. Miller, J. M. Rosamilia, R. M. Fleming, A. R. Kortan, S. H. Glarum, A. V. Makhija, A. J. Muller, R. H. Eick, S. M. Zahurak, R. Tycko,

- G. Dabbagh, and F. A. Thiel. Conducting films of C_{60} and C_{70} by alkali metal doping. *Nature*, 350:320–22, 1990.
- [50] S. Hino, K. Matsumoto, S. Hasegawa, K. Kamiya, Hiroo Inokuchi, T. Morikawa, R. Takahashi, K. Seki, K. Kikuchi, S. Suzuki, I. Ikemoto, and Y. Achiba. Ultraviolet photoelectron spectra of C_{84} and K_xC_{84} . *Chem. Phys. Lett.*, 190(3,4):54–61, Mar 1992.
- [51] C. A. Klein. Pulsed laser-induced damage to diamond. *Diamond Films Technol.*, 5(3):141–58, 1995.
- [52] P. B. Corkum, F. Brunel, N. K. Sherman, and T. Srinivasan-Rao. Thermal response of metals to ultra-short pulse laser excitation. *Phys. Rev. Lett.*, 61(25):2886–89, 1988.
- [53] S. M. Sze, J. L. Moll, and T. Sugano. *Solid-State Electronics*, volume 7, pages 509–23. Permagon Press, 1964.
- [54] C. R. Cromwell, W. G. Spitzer, L. E. Howarth, and E. E. LaBate. Attenuation length measurements of hot electrons in metal films. *Phys. Rev.*, 127(6):2006–15, Sep 1962.